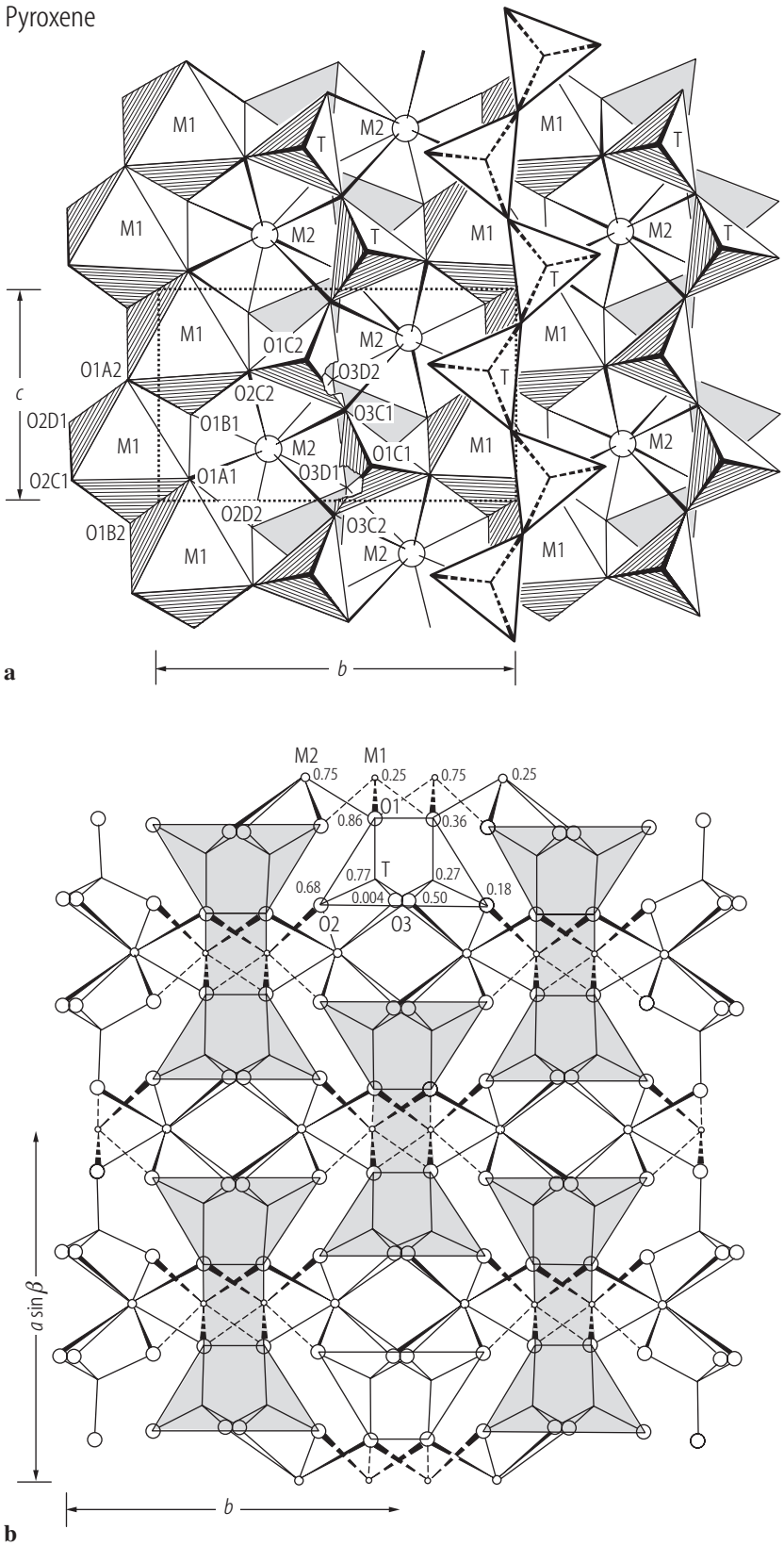

Fig. 1. Pyroxene having crystal structure of C2/c-type. (**a**) Projected onto the (100) plane [67B5, 81C1]; (**b**) projected down [001]. Shaded areas outline I-beam units [81C1].

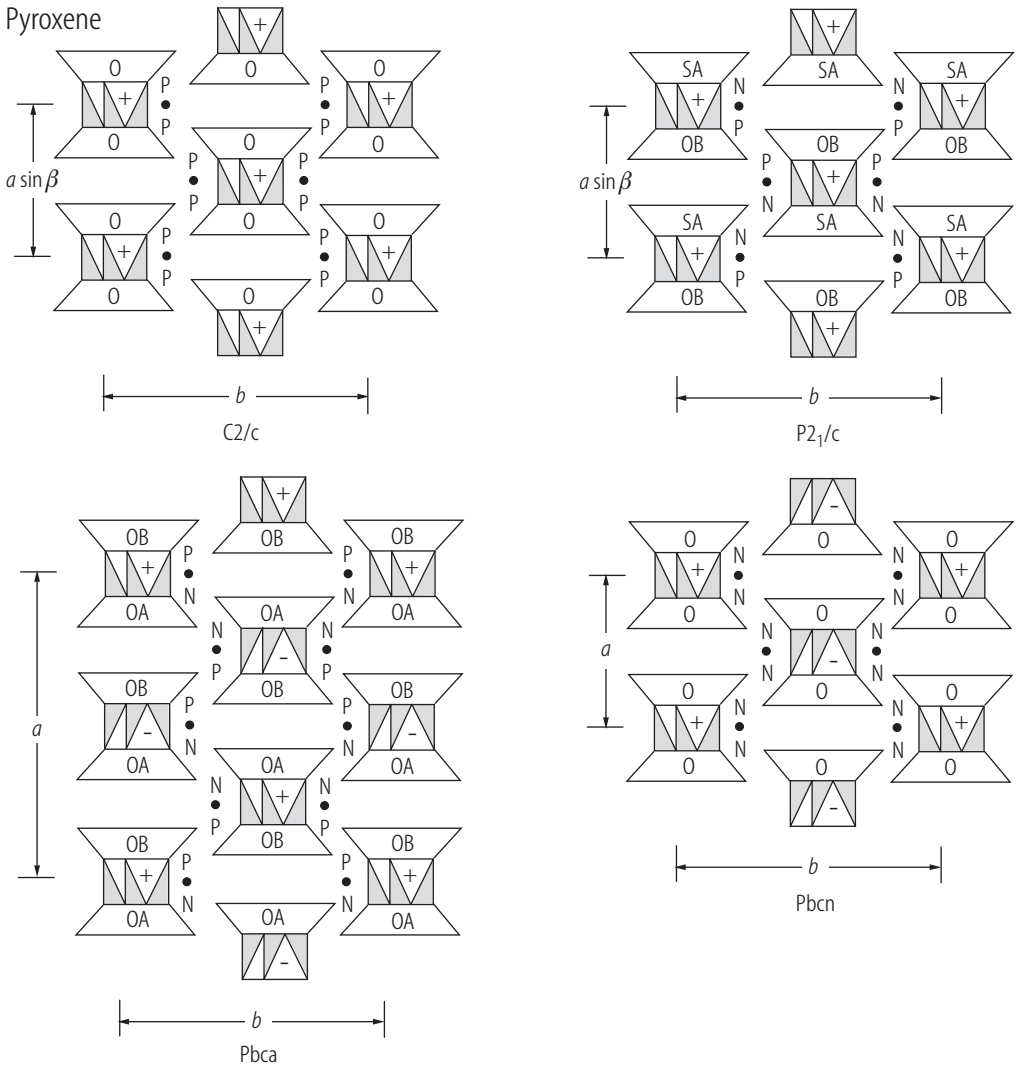

Fig. 2. Pyroxenes. I-beam diagrams [73P1].

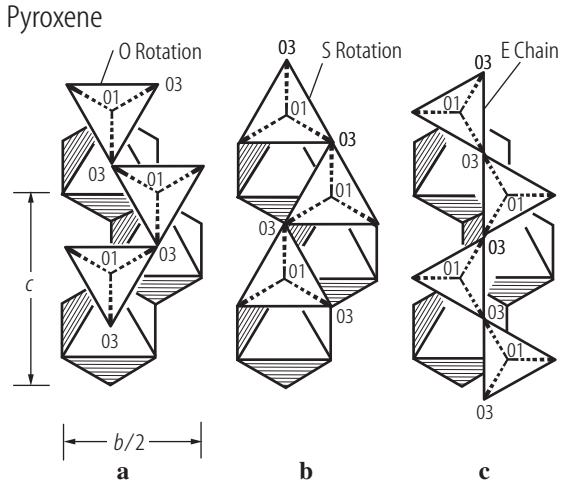

Fig. 3. Pyroxene. Complete O and S rotation and extended (E) chain configuration for an ideal pyroxene structure [81C1]. There is a difference in the size of tetrahedra in (**a**) and (**b**) as compared to (**c**).

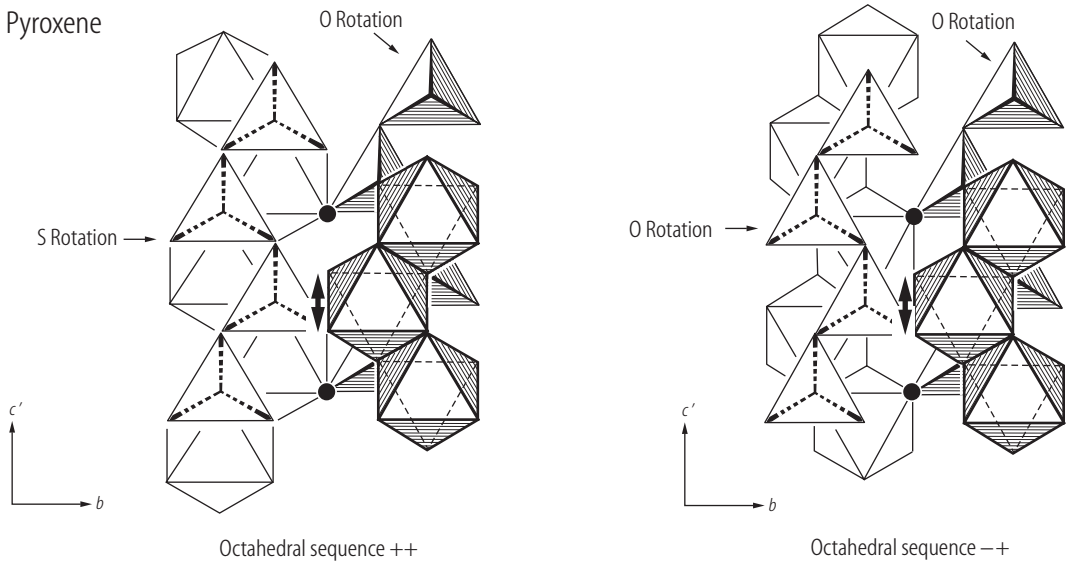

Fig. 4. Pyroxenes. Stacking sequences for ideal, completely rotated structures. Arrow in both figures show the degree of mismatch between tetrahedra and octahedra in hypothetical structures with parity violations [73P1, 81C1].

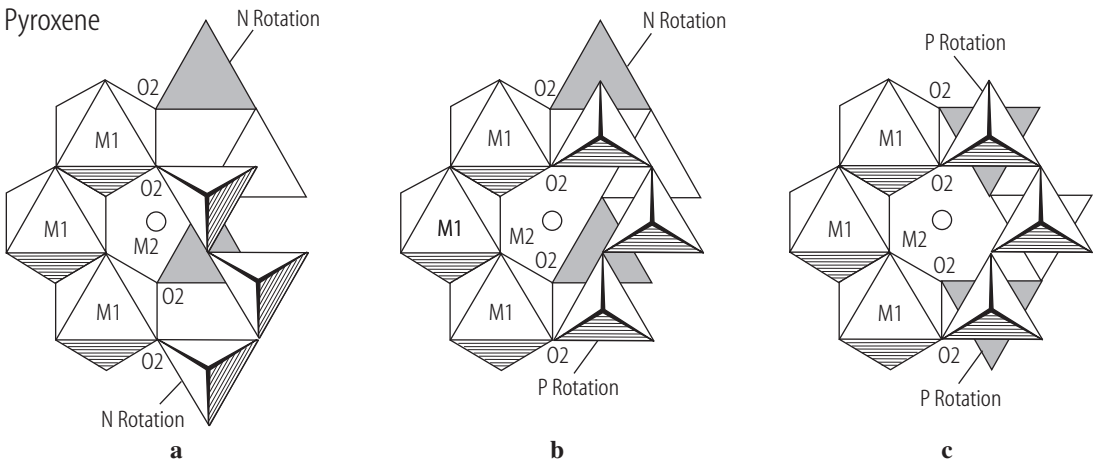

Fig. 5. Pyroxenes.Configuration of tetrahedral chains around the M2 site in an ideal structure [76S1, 81C1].

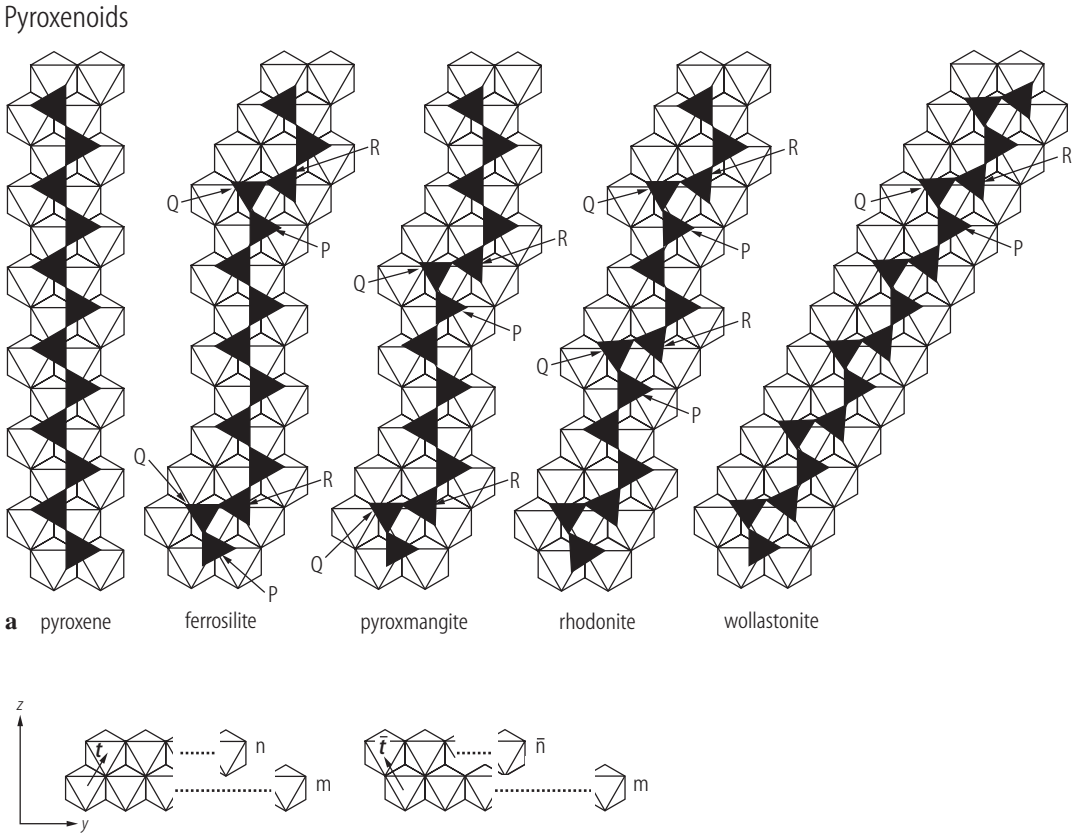

Fig. 6. Pyroxenoid ideal structural configurations. (**a**) Basic silicate chain and octahedral ribbon [80A1]: pyroxene, ferrosilite III, pyroxmangite, rhodonite, wollastonite; (**b**) finite linear arrays consisting of m and n regular octahedra showing stacking vectors $\boldsymbol{t}$ and $\bar{\boldsymbol{t}}$ [77T2].

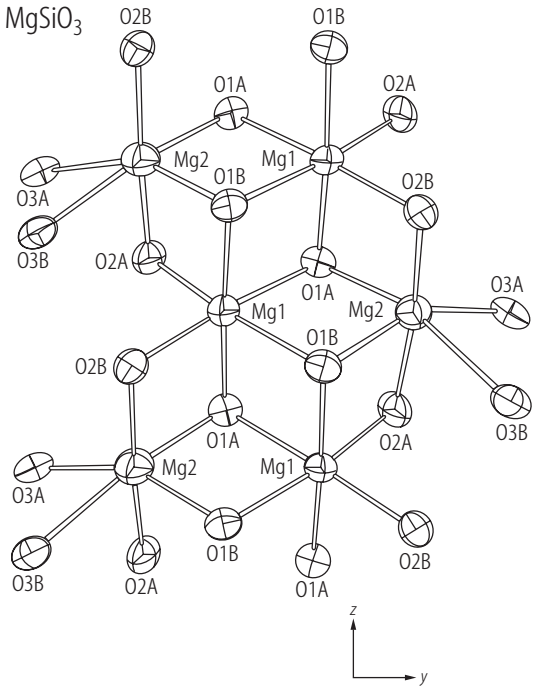

Fig. 7. $MgSiO_3$. Double chains of edge-sharing octahedra $Mg1O_6$ and $Mg2O_6$ parallel to [001] in OEn (space group Pbca) [86G3].

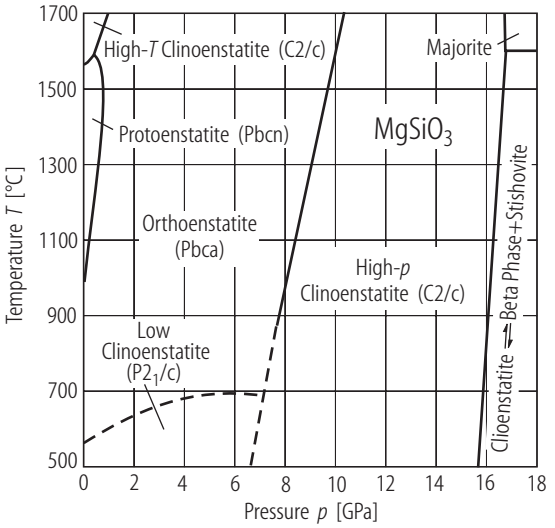

Fig. 8. $MgSiO_3$. Temperature-pressure phase diagram [90P1]. Extrapolations of experimentally determined boundaries are dashed. The high-*T* clinoenstatite and protoenstatite stability fields were calculated from the thermodynamic model of [90G2].

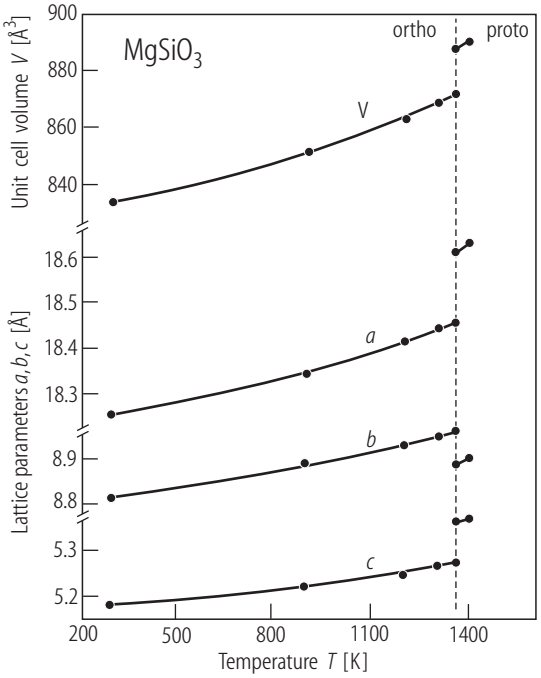

Fig. 9. $MgSiO_3$. Unit-cell dimensions and volume at OEn – PEn as a function of temperature. For comparison the *a* dimension and unit cell volume of PEn were doubled [95Y2].

For Fig. 10 see next page

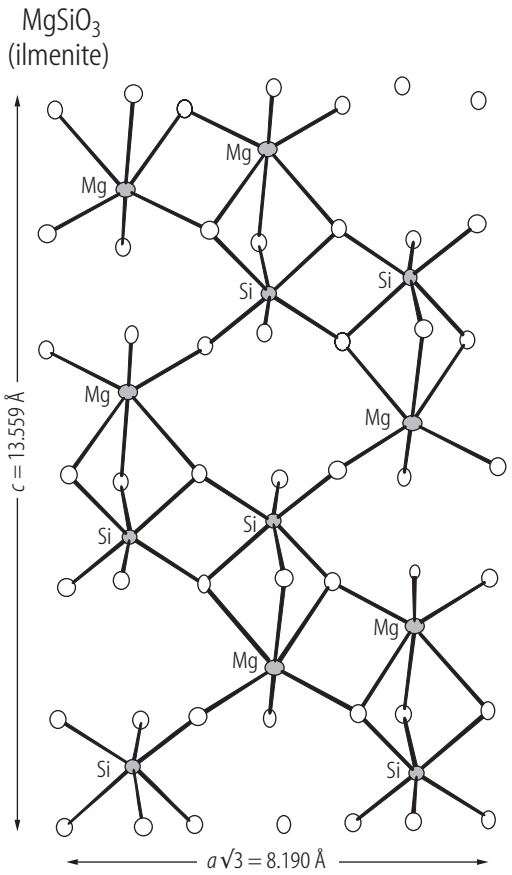

Fig. 11. $MgSiO_3$ ilmenite. A perspective view of the structure [82H1].

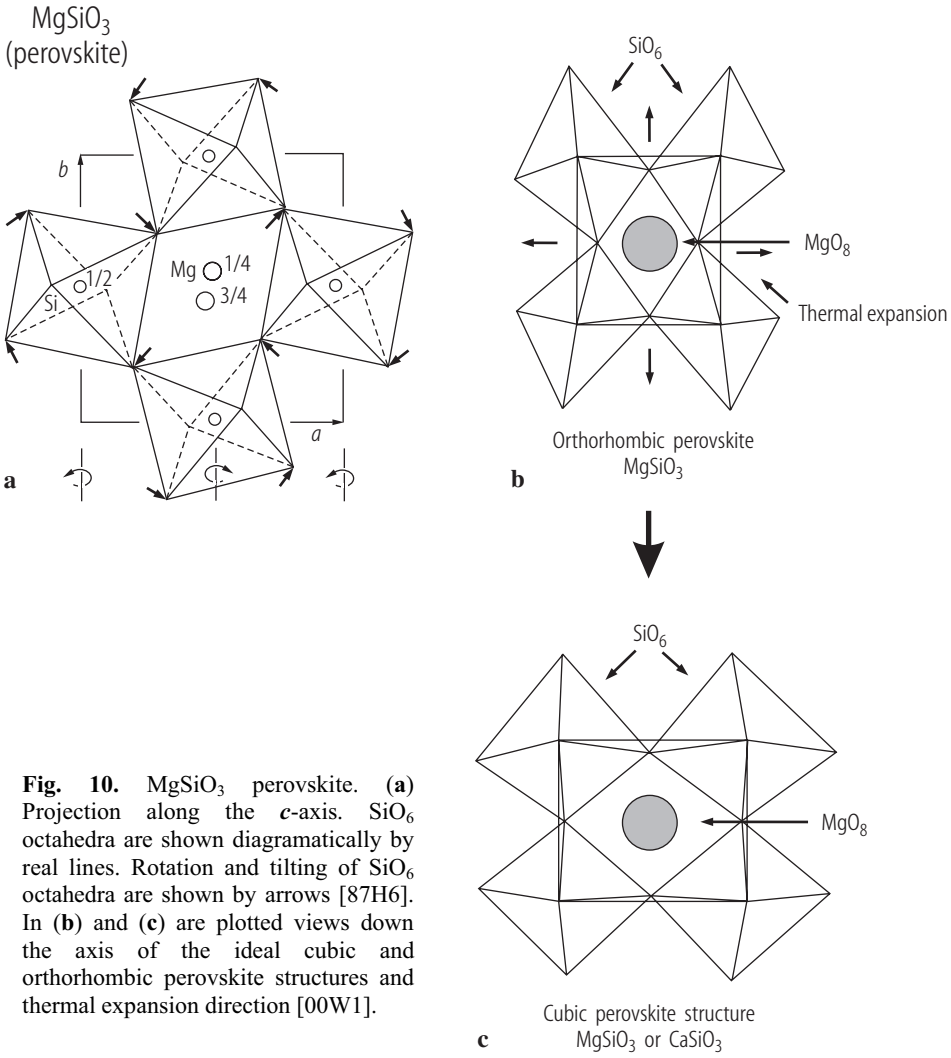

Fig. 10. $MgSiO_3$ perovskite. (**a**) Projection along the ***c***-axis. SiO_6 octahedra are shown diagramatically by real lines. Rotation and tilting of SiO_6 octahedra are shown by arrows [87H6]. In (**b**) and (**c**) are plotted views down the axis of the ideal cubic and orthorhombic perovskite structures and thermal expansion direction [00W1].

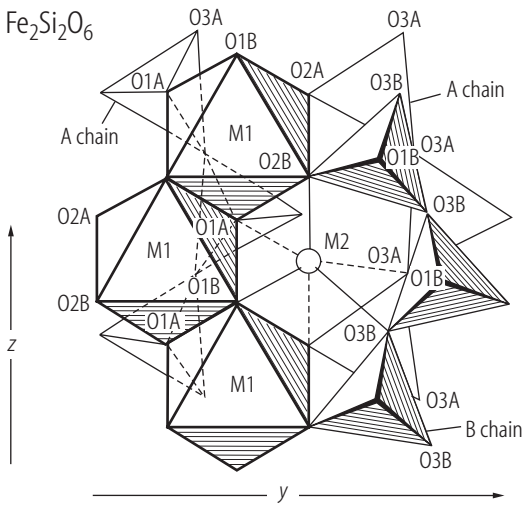

Fig. 12. $Fe_2Si_2O_6$. Partial view of the crystal structure. The double octahedral chain is shown. We note the regular octahedral site M1 and the distorted octahedral site M2, both occupied by Fe^{2+} [76S1].

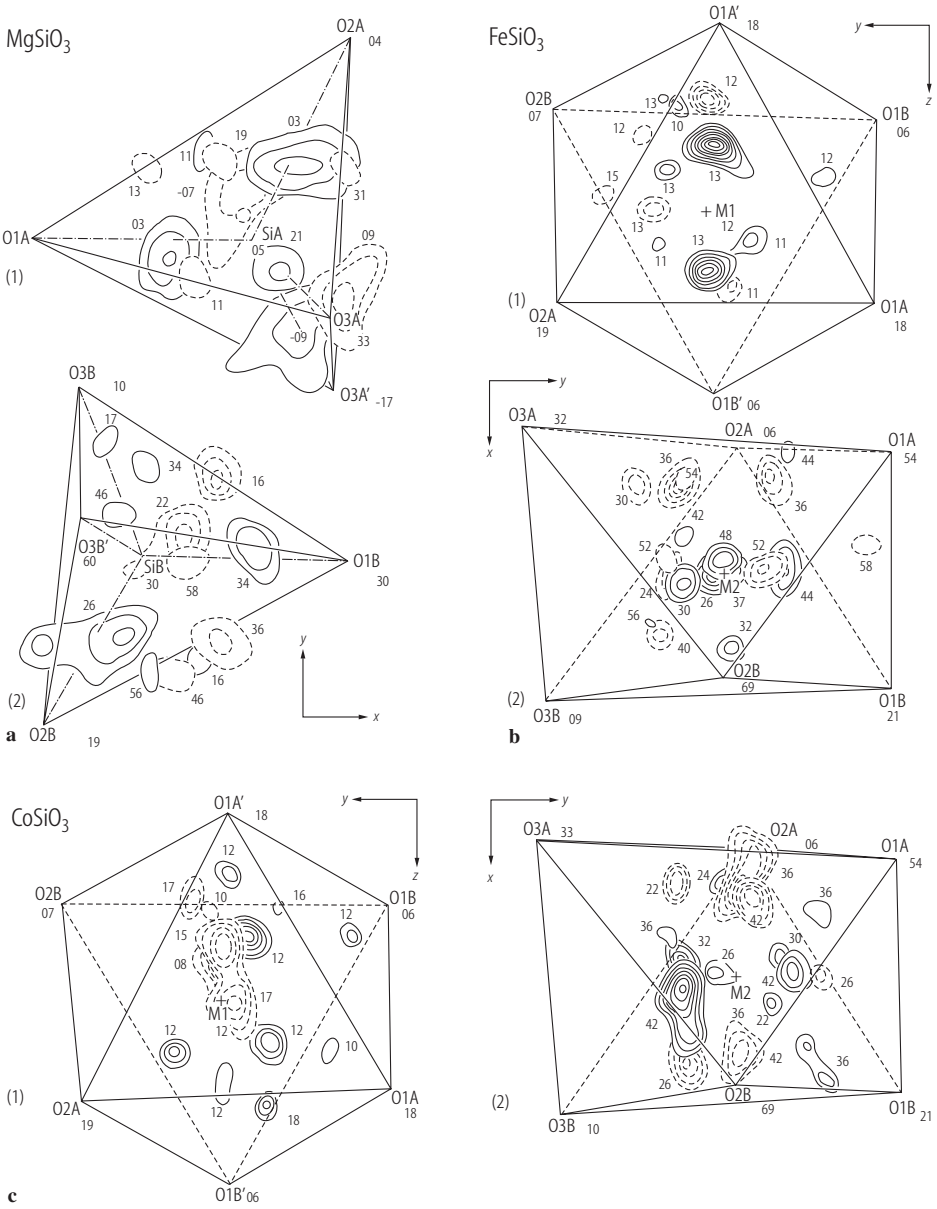

Fig. 13. $MSiO_3$ (M = Mg, Fe, Co). Composite differential Fourier maps. (**a**) $MgSiO_3$ OEn showing residual peaks around SiA (1) and SiB (2). Numbers give, in decimal fraction of *c*, the heights of atoms or the levels of sections approximately passing through the center of peaks. (**b**) $FeSiO_3$ OFs showing residual peaks around Fe at the M1(1) and M2(2) sites. (**c**) $CoSiO_3$ showing the residual peaks around Co at M1(1) and M2(2). In (**a-c**) the contours are at intervals of 0.1 $e/Å^3$, negative contours being broken and zero contours (**a**) and lower ones than 0.3 $e/Å^3$ in (**b**) and 0.4 $e/Å^3$ in (**c**) being omitted. Numbers indicate, in decimal fraction of *a* (in case (1)) or *c* (in case (2)), the heights of atoms or the levels of sections passing through the centers of peaks [82S1].

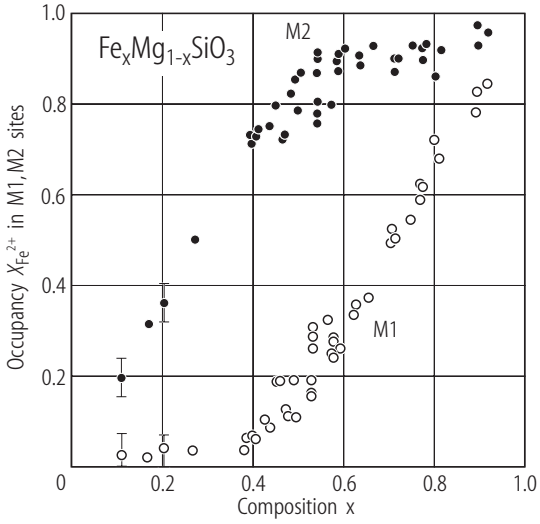

Fig. 14. $Fe_xMg_{1-x}SiO_3$ OPx. Occupancy of Fe^{2+} at M1 and M2 sites [01V1]. Data are from [67B2, 67E2, 69S2, 70V1, 86S1, 86W1].

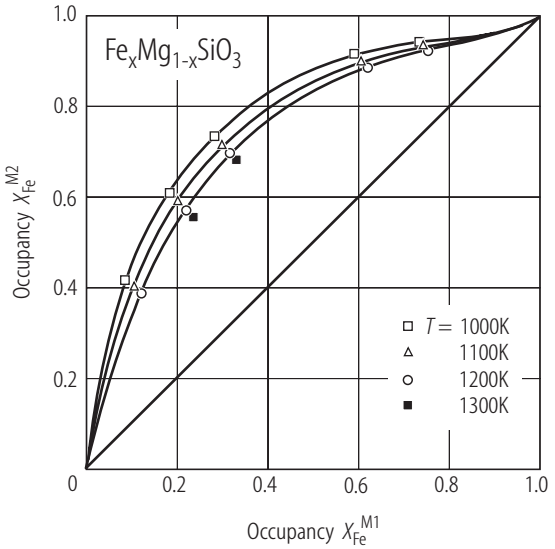

Fig. 15. $Fe_xMg_{1-x}SiO_3$ OPx. Site occupancies of Fe between M1 and M2 as function of composition [94Y2].

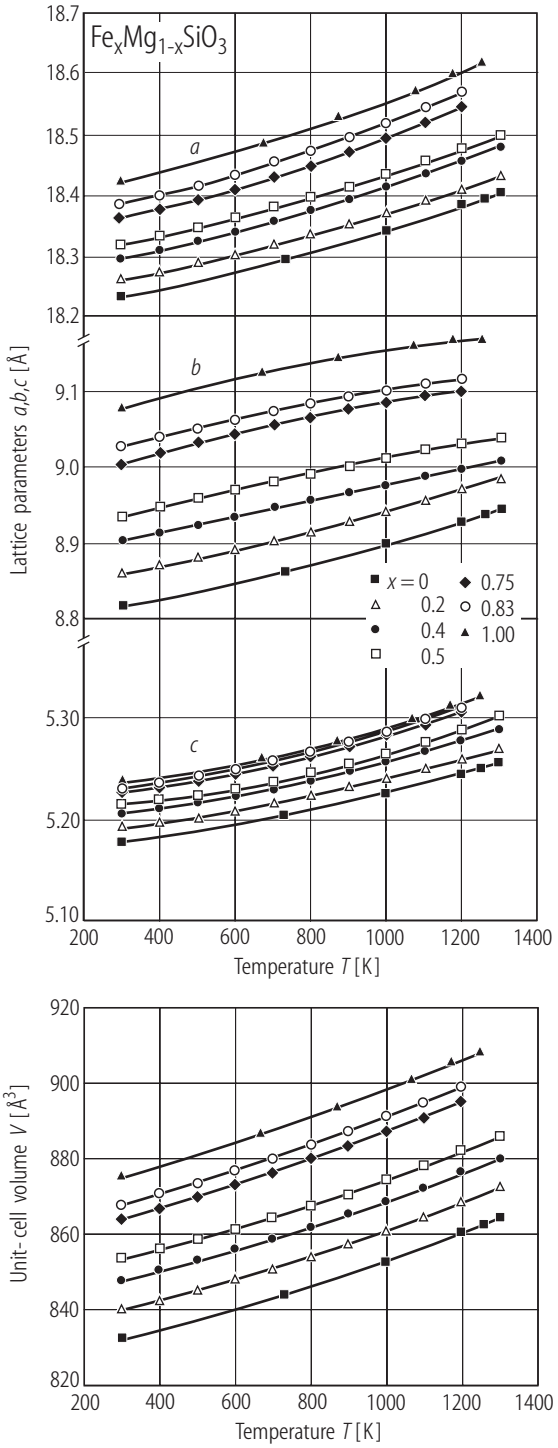

Fig. 16. $Fe_xMg_{1-x}SiO_3$ orthopyroxenes. Lattice parameters and volumes as function of temperature [94Y1].

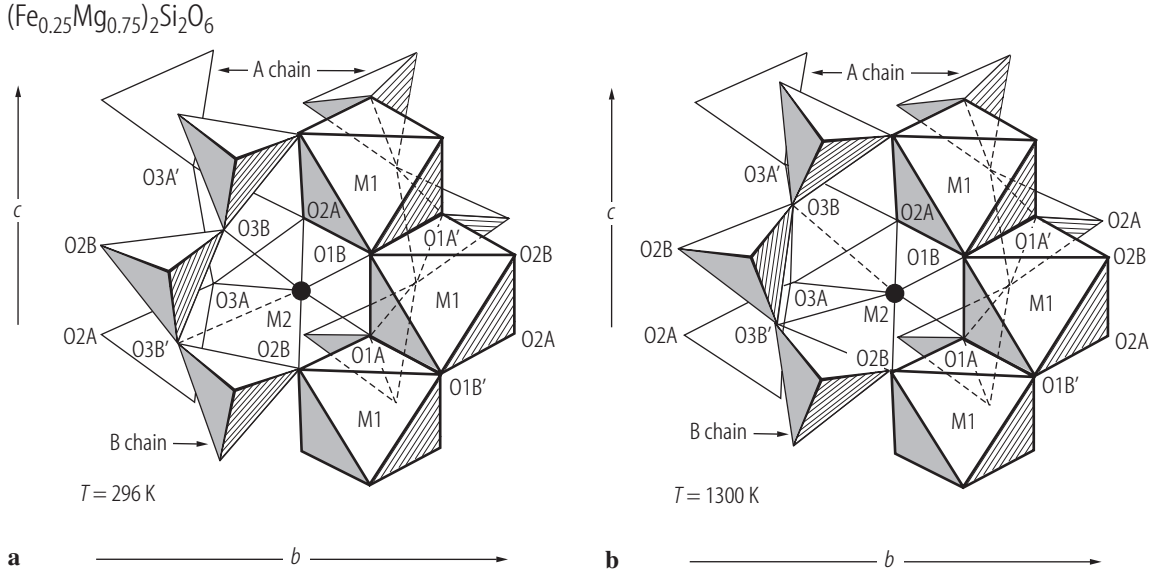

Fig. 17. $(Fe_{0.25}Mg_{0.75})_2Si_2O_6$ OPx. Projection of a part of structure along [100]; (**a**) T = 296K; (**b**) T = 1300K [95Y1].

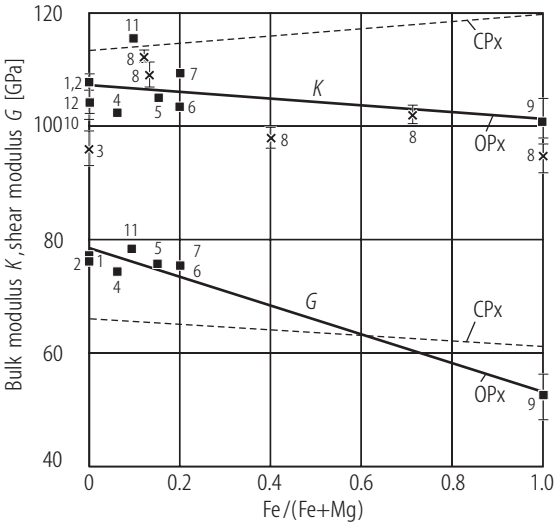

Fig. 18. $Fe_xMg_{1-x}SiO_3$ OPx. Elastic moduli: *1* – [99J1]; *2* – [78W1]; *3* – [94H1]; *4* – [88D2]; *5* – [69K1]; *6* – [72F1]; *7* – [93W2]; *8* – [97H2]; *9* – [84B2]; *10* – [95Z1]; *11* – [97C1]; *12* – [98F1]. Dashed lines indicate clinopyroxene (CPx) trends defined by the diopside-hedenbergite solid solution series [64A1, 79L1, 88K1].

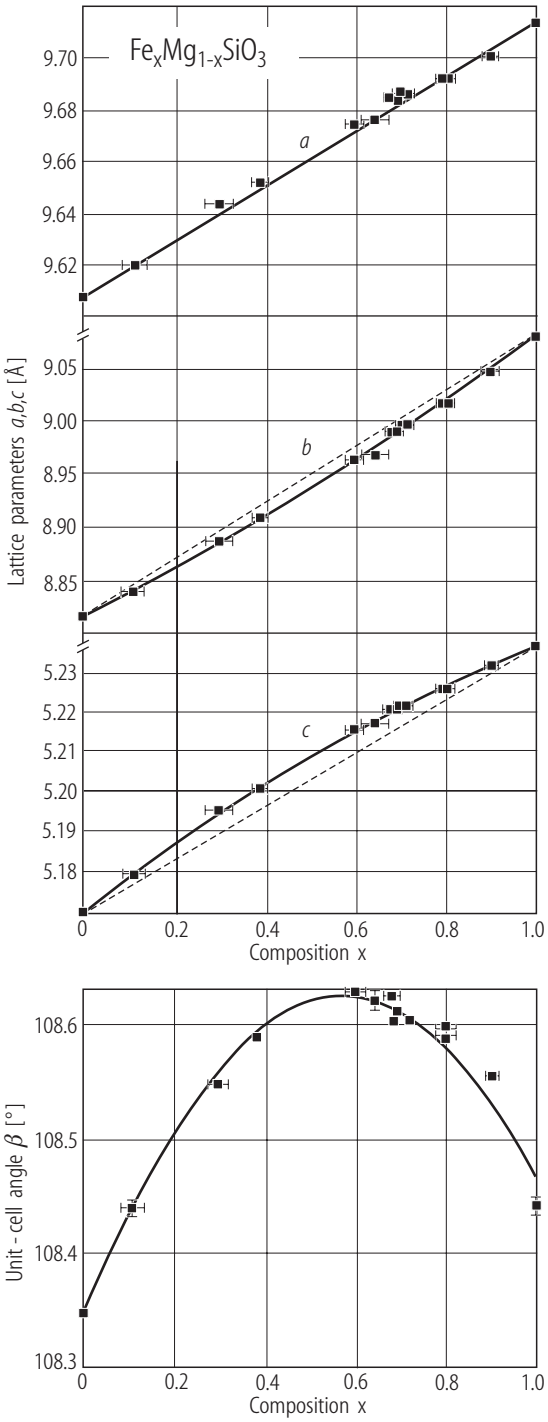

Fig. 19. $MgSiO_3$-$FeSiO_3$ clinopyroxenes ($P2_1/c$ type). Composition dependences of the lattice parameters [98A3]. The solid lines are the regression relations reported in text and dashed lines are interpolations between the two end members.

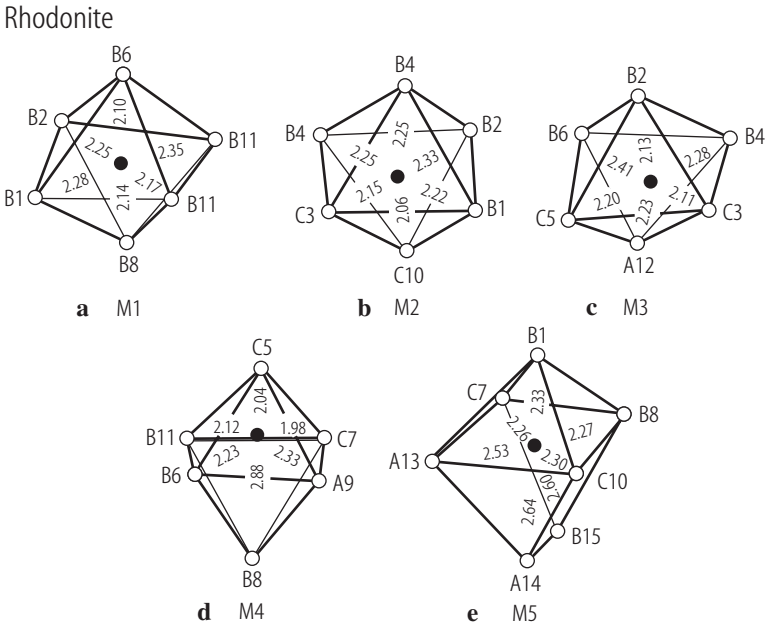

Fig. 20. Rhodonite. Projections of the oxygen coordination polyhedra about the five cation positions [75D1]. Metal-oxygen distances are indicated (in Å). The letters A, B and C indicate the oxygen ion type.

For Figs. 21, 22 see next pages

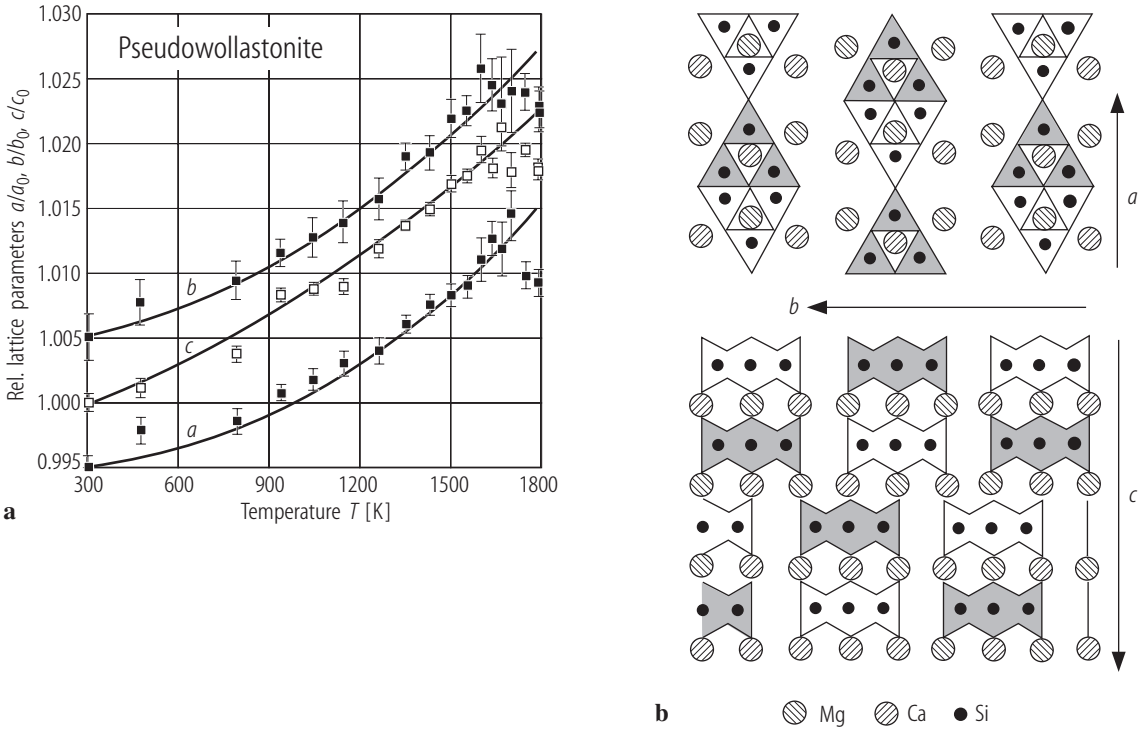

Fig. 23. Pseudowollastonite. Relative changes of the *a*, *b* and *c* lattice parameters as function of temperature. The data for *a* and *c* have been displaced upward and downward, respectively by 0.005 units [98R3]. In (**b**) is plotted a schematic sketch of the structure showing tetrahedral and octahedral layers. Si atoms form Si_3O_9 rings.

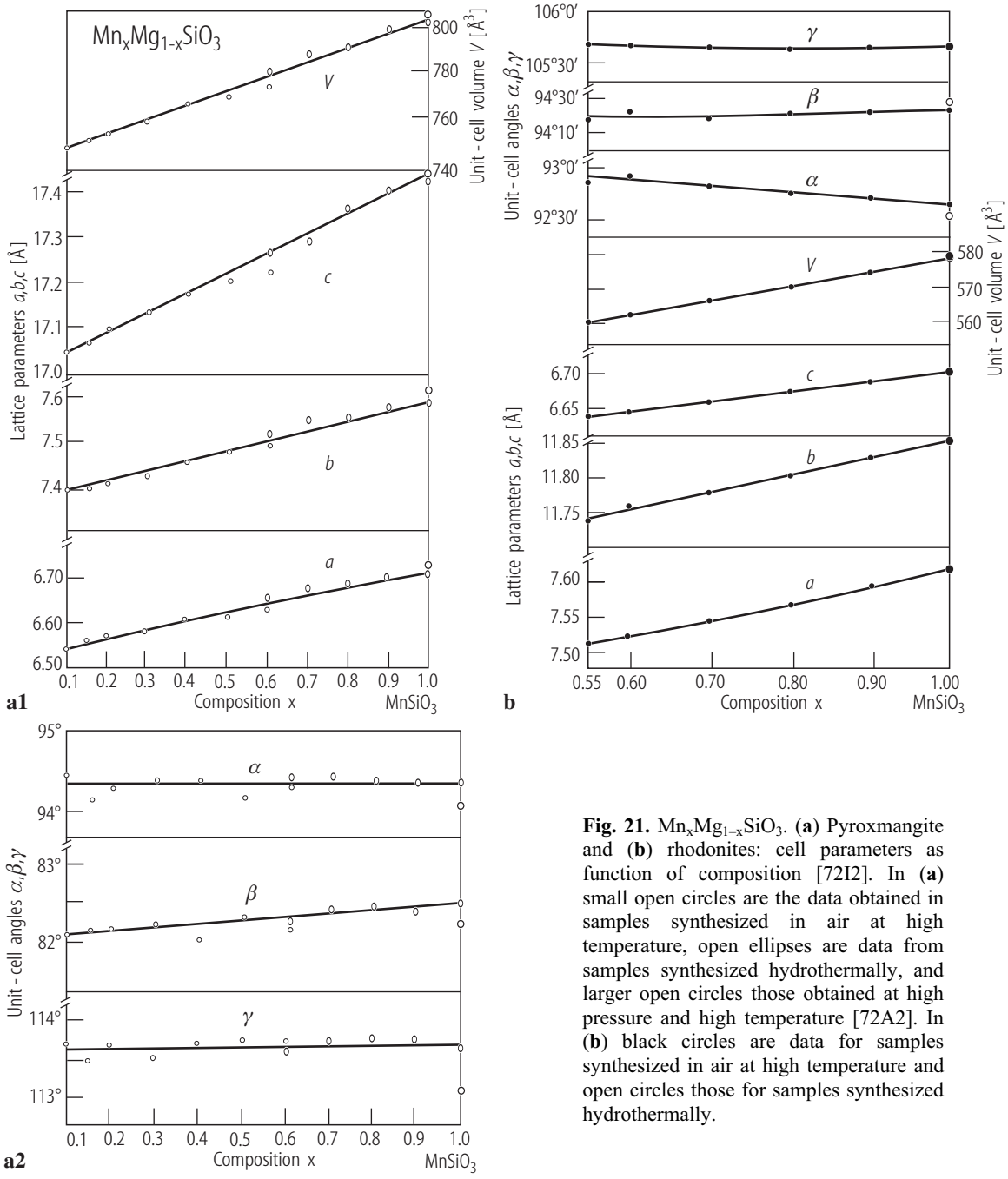

Fig. 21. $Mn_xMg_{1-x}SiO_3$. (**a**) Pyroxmangite and (**b**) rhodonites: cell parameters as function of composition [72I2]. In (**a**) small open circles are the data obtained in samples synthesized in air at high temperature, open ellipses are data from samples synthesized hydrothermally, and larger open circles those obtained at high pressure and high temperature [72A2]. In (**b**) black circles are data for samples synthesized in air at high temperature and open circles those for samples synthesized hydrothermally.

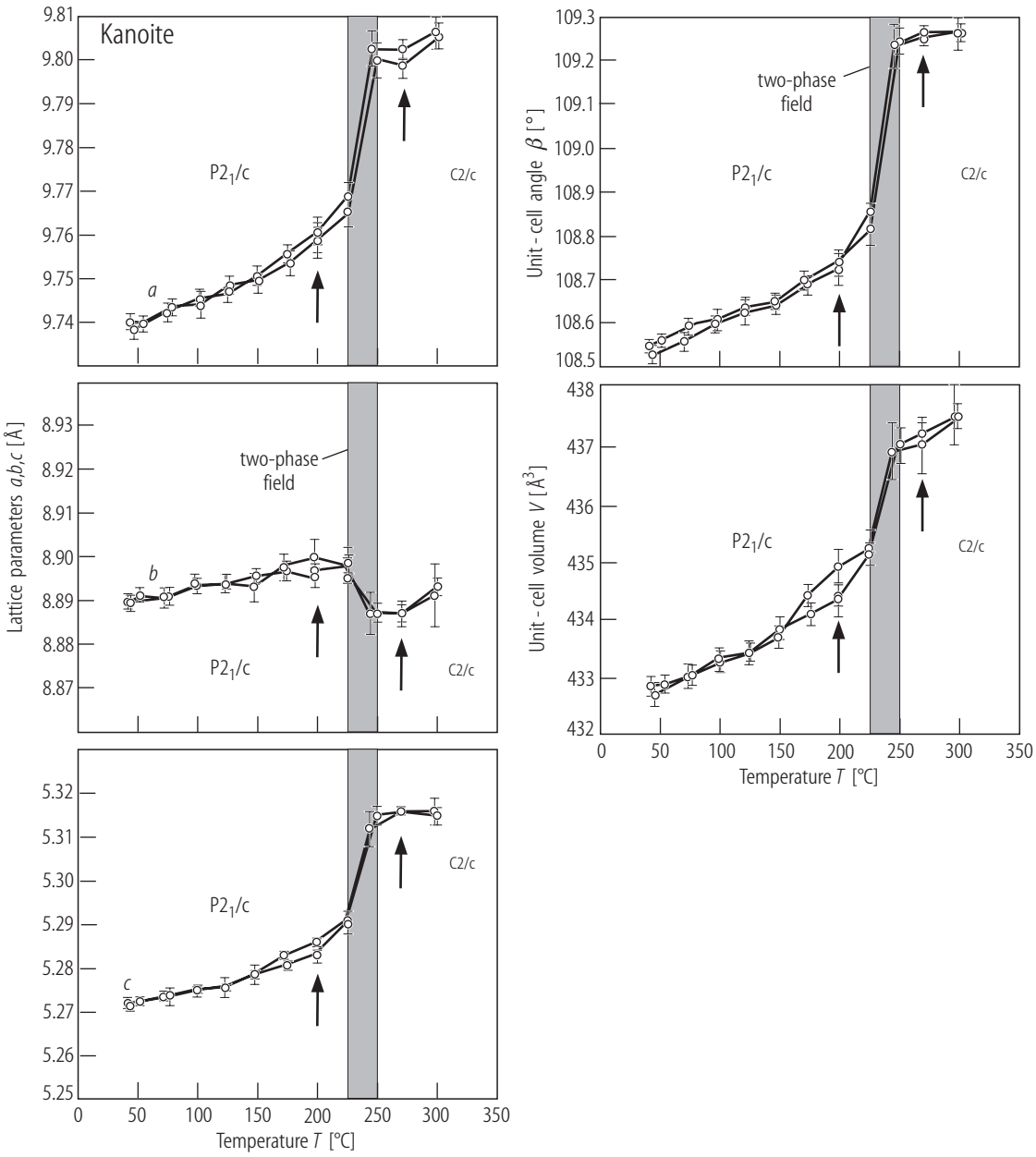

Fig. 22. Kanoite. Cell parameters and volumes as function of temperature. Arrows indicate temperatures were X-ray intensity data for structural refinements were collected [97A2].

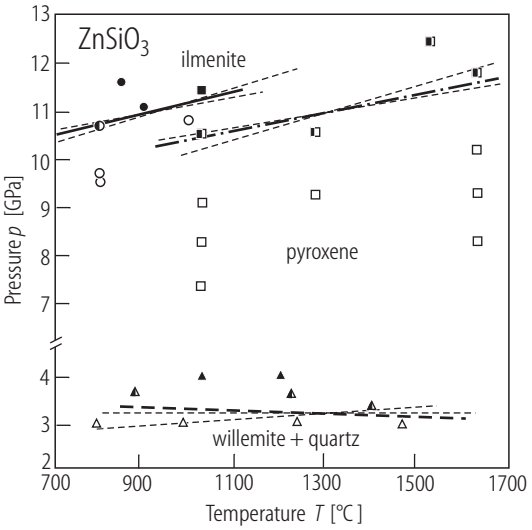

Fig. 24. $ZnSiO_3$. Pressure-temperature phase relations [89L1]. The lower-pressure stability limit of clinopyroxene is from [71S4] (heavy dashed line). The two phase boundaries for the appearance of ilmenite are from [79O4] (dash-dot line) and [77A2] (solid line). Light dashed lines show the uncertainty limits for phase boundaries calculated from the enthalpy data by assuming a fixed point on each experimental curve [89L1]. Data points are from [71S4] (triangles), [79O4] (squares) and [77A2] (circles).

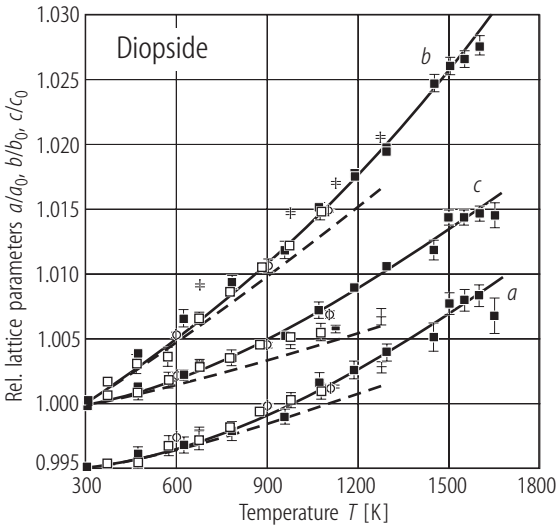

Fig. 26. Diopside. Relative changes in *a*, *b* and *c* lattice parameters as function of temperature. The data for *a* have been displaced downward by 0.005 units [98R3]. Data are from: full squares [98R3], open squares [73C1], circles [76F1], crosses [73D1]. The dashed lines represent the dilatometry data for a natural sample [33K1].

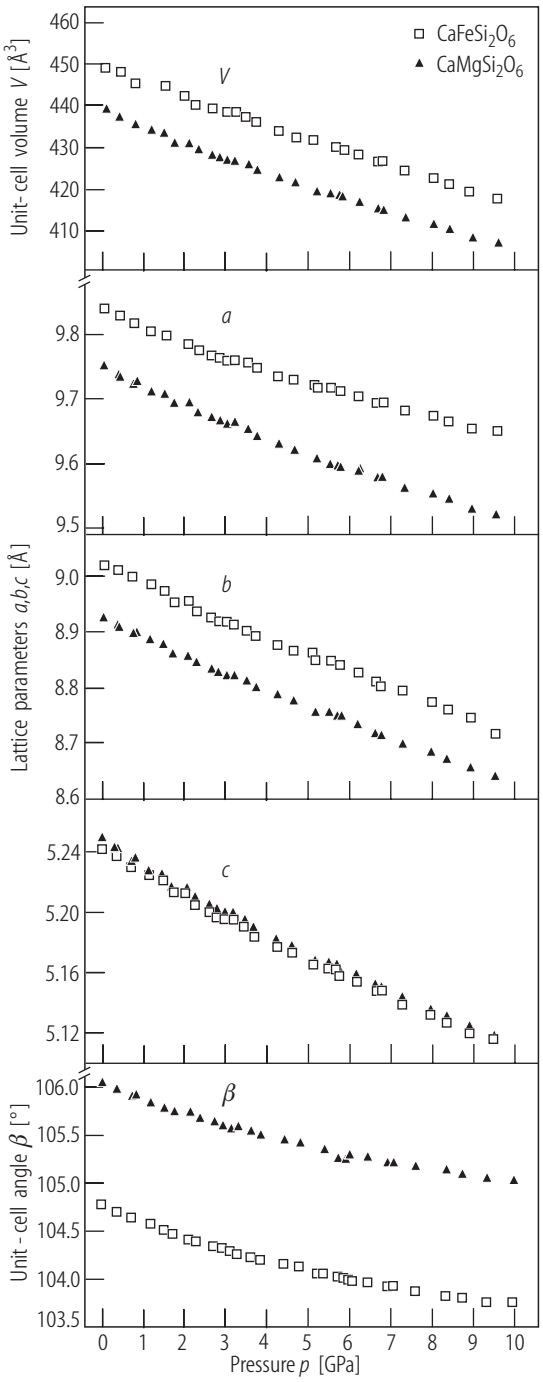

Fig. 25. $CaMgSi_2O_6$, $CaFeSi_2O_6$. Pressure dependences of the lattice parameters [97Z1].

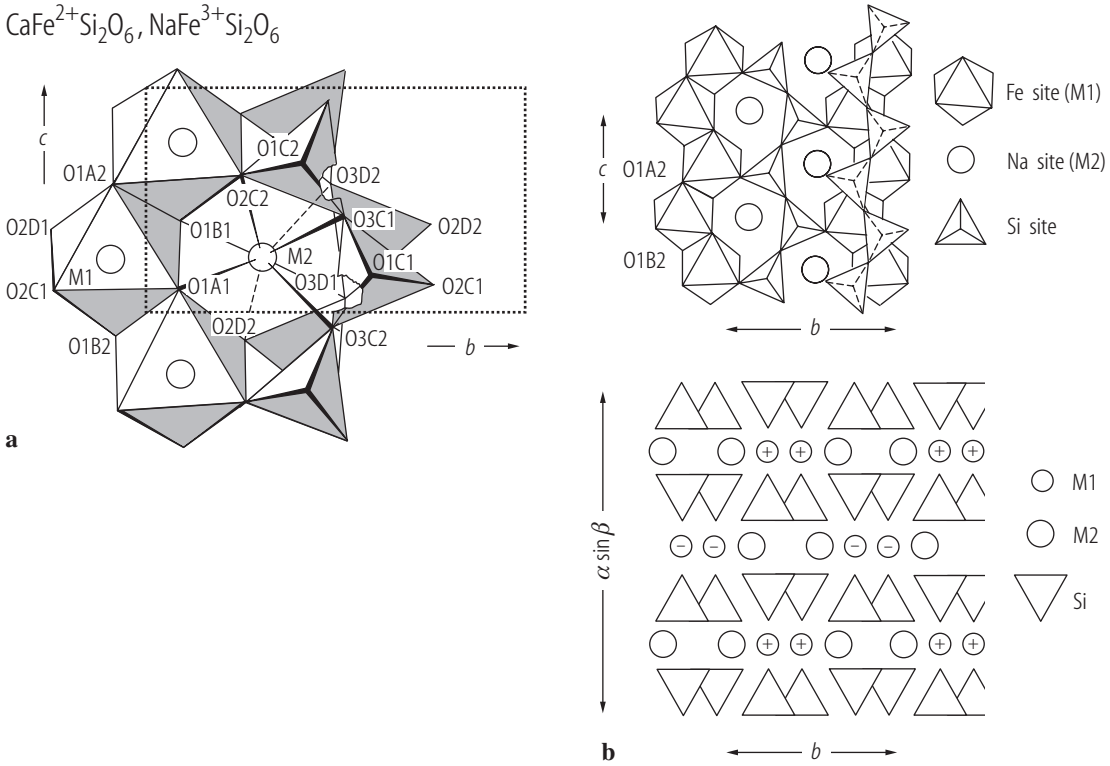

Fig. 27. $CaFe^{2+}Si_2O_6$, $NaFe^{3+}Si_2O_6$. (**a**) Crystal structure projected down ***a**** where the M1 site is occupied by Fe^{2+} or Fe^{3+} and M2 by Ca or Na [73C1]; (**b**) schematic illustration of oxygen polyhedra showing the M1 iron chains [85C2]. The magnetic structure is also indicated (+ and – signs).

For Figs. 28, 29 see next page

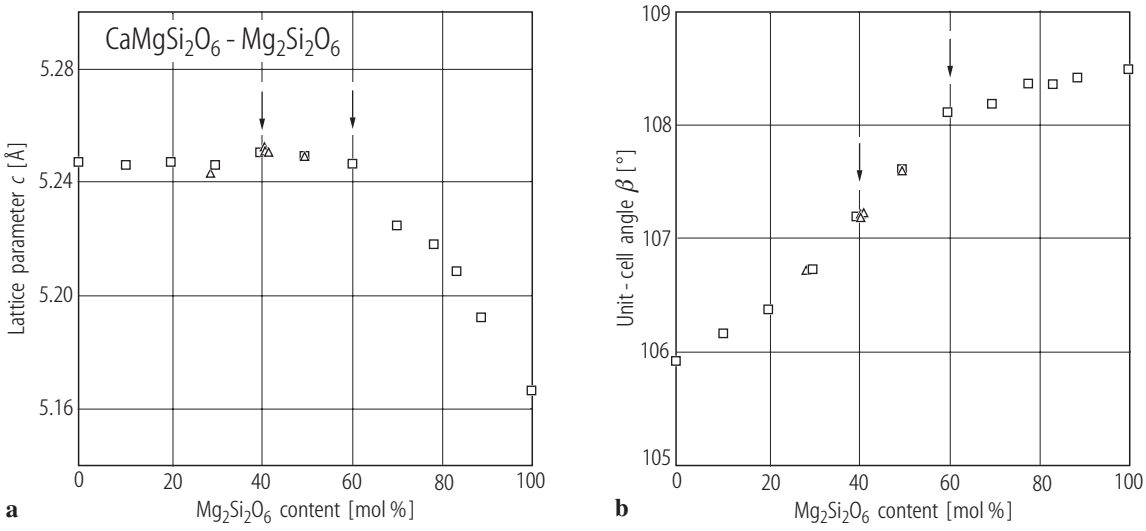

Fig. 30. $CaMgSi_2O_6$ – $Mg_2Si_2O_6$. (**a**) *c*- and *β*-parameters as function of composition [00T2]. The arrows indicate the observed C-P transition point (left) and discontinuity in cell parameters (right). Triangles [00T2]; squares [76O1, 79N1].

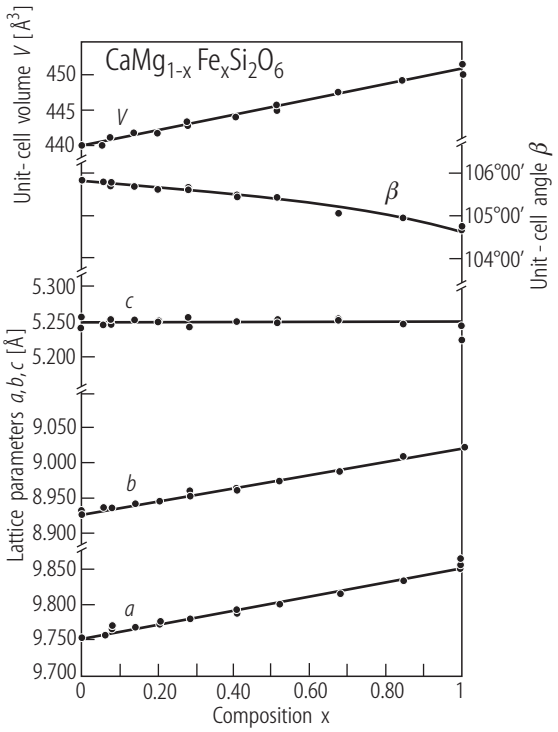

Fig. 29. $CaMgSi_2O_6$ – $CaFeSi_2O_6$. Composition dependences of lattice parameters [69R1].

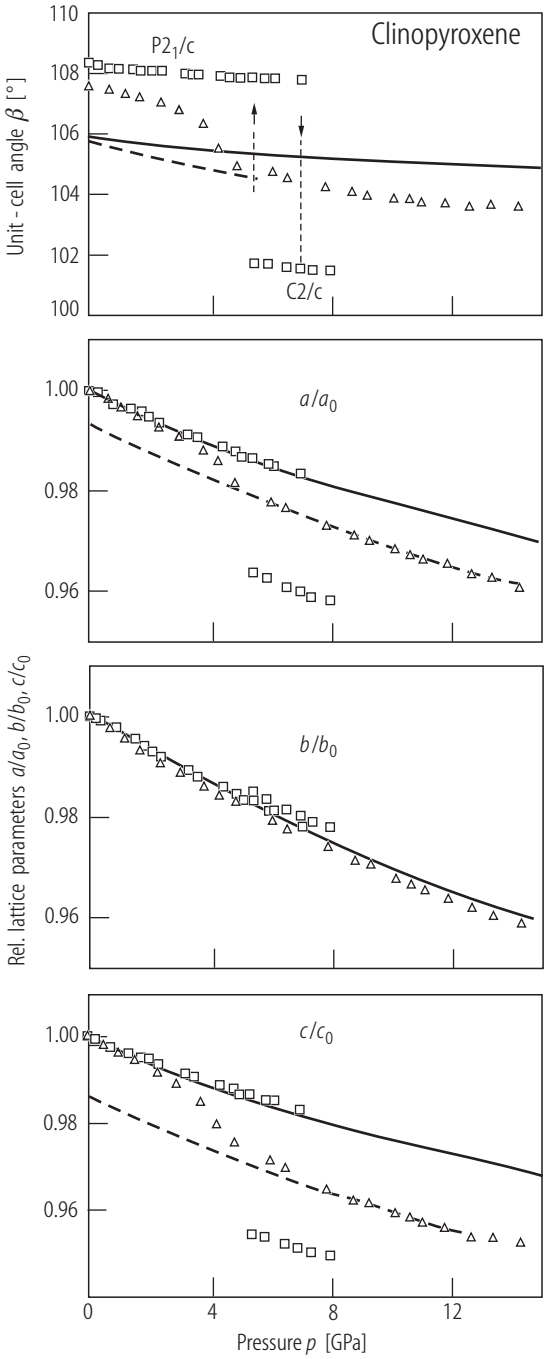

Fig. 28. Clinopyroxene. Lattice parameters as function of pressure [00T2]. Triangles indicate $Ca_{0.5}Mg_{1.5}Si_2O_6$ [00T2], squares are from clinoenstatite [94A1]. The continuous line is for diopside [00T2], the dashed line shows the trend for the C2/c high-pressure phase $Ca_{0.5}Mg_{1.5}Si_2O_6$ (not reported for *b* parameter). Vertical dashed lines show the hysteresis in clinoenstatite (β angle) [00T2].

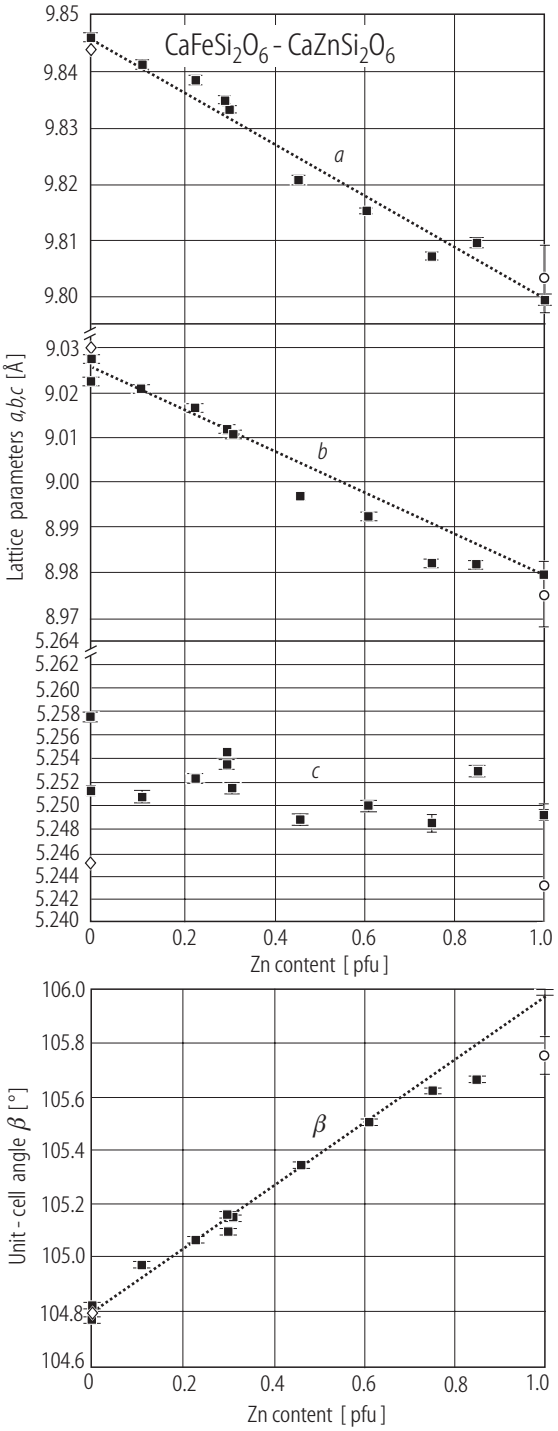

Fig. 31. $CaFeSi_2O_6$ – $CaZnSi_2O_6$. Composition dependences of the lattice parameters [04H1] (full squares). The data of [87E1] and [00R1] are also given by open circles and diamonds, respectively.

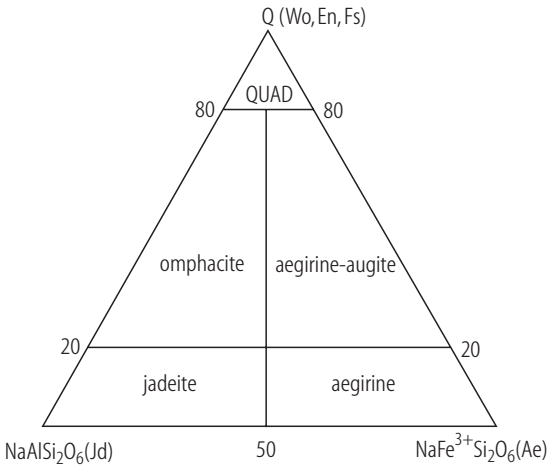

Fig. 32. Ca-Mg-Fe and Na pyroxenes with accepted names.. QUAD represents the Ca-Mg-Fe pyroxene area [88M3].

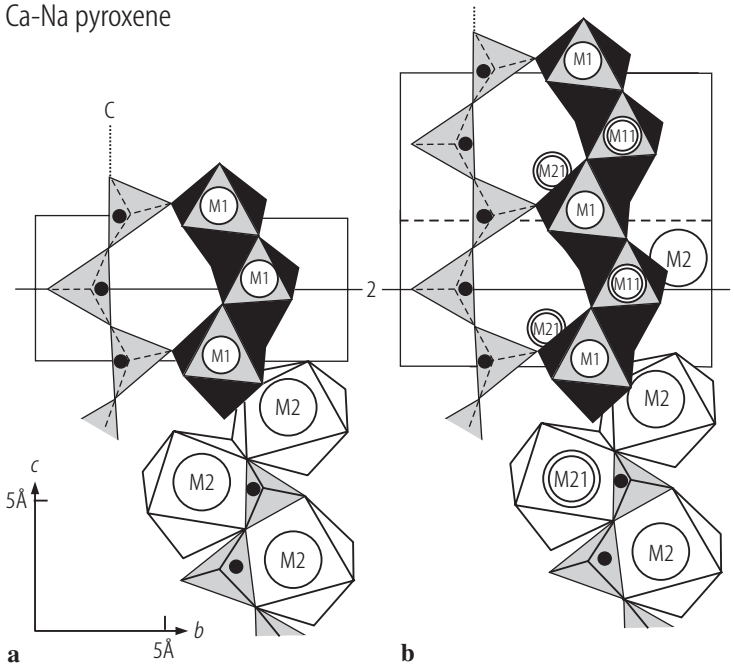

Fig. 33. Ca-Na pyroxenes. The sixfold coordinated strip (dark) for (**a**) a disordered C2/c pyroxene and (**b**) an ordered P2/n omphacite, projected onto the (100) plane, also showing the lateral relationships with tetrahedral chain (gray) and the eightfold coordinated cation (white) [99M1].

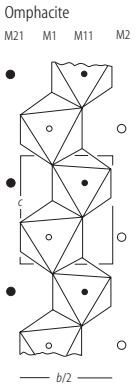

Fig. 34. Omphacite (space group P2/n). Octahedral strip at x = ¼ showing the one-dimensional arrays of M-cations parallel to the ***c***-axis: M21 (2/3Ca, 1/3Na); M1 (Mg, Fe^{2+}); M11 (A1); M2 (1/3Ca, 2/3Na) [78F1].

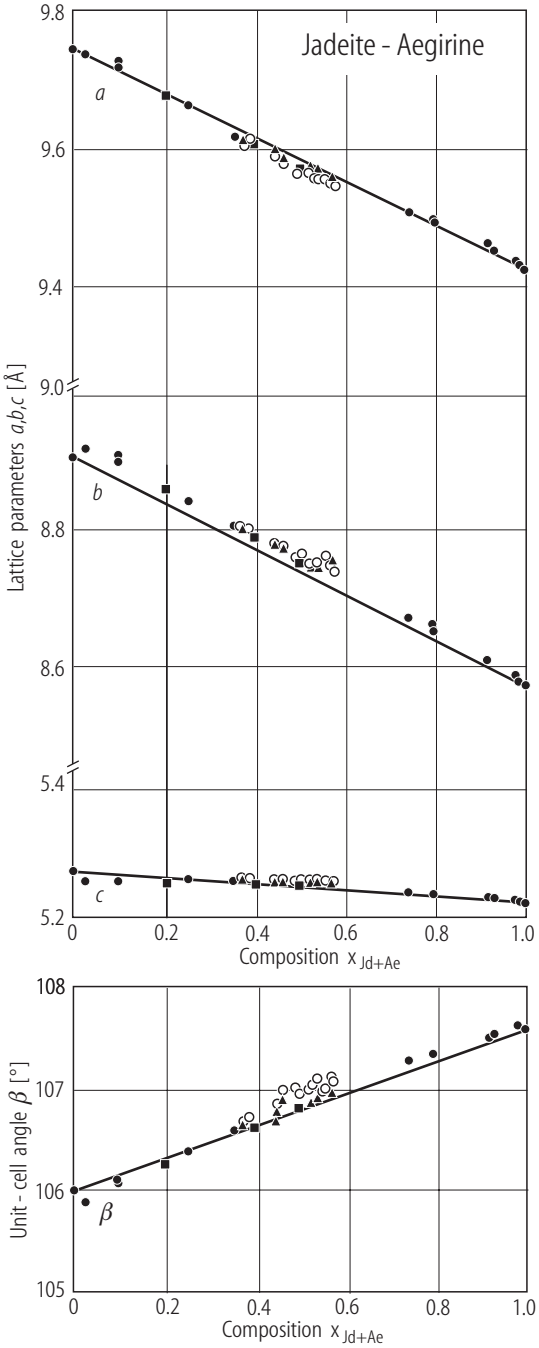

Fig. 35. $Ca(Mg,Fe^{2+})Si_2O_6$ – $Na(Fe^{3+},Al^{3+})Si_2O_6$ (jadeite-aegirine). Composition dependences of the unit cell parameters *a*, *b*, *c* and β [98B1]. Filled circles (C2/c), open circles (P2/n), filled triangles (disordered samples), filled squares (synthetic). Only for the unit cell angle β it is possible to note a difference between ordered and disordered data.

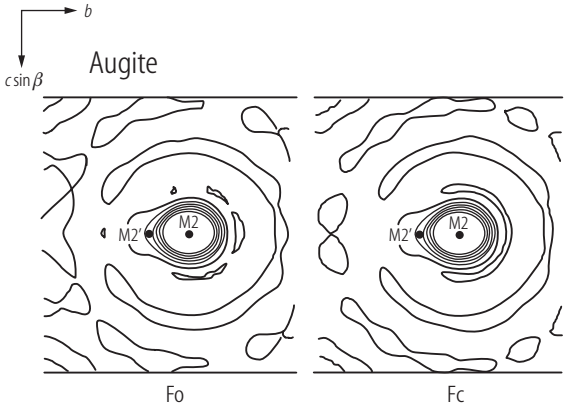

Fig. 36. Augite. Observed (Fo) and calculated (Fc) electron density maps, computed by taking into account M2' site occupancy [87R2].

$LiAlSi_2O_6$

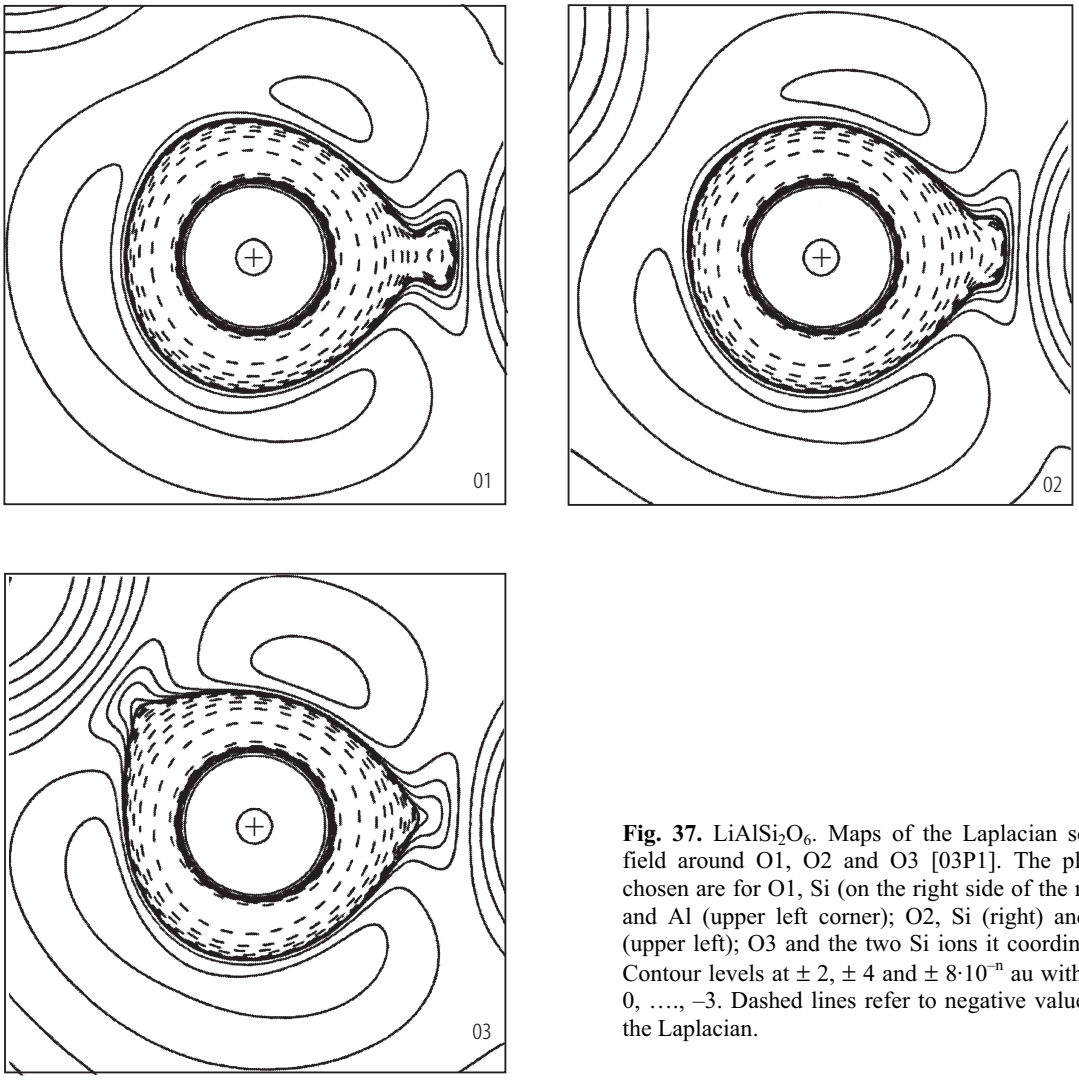

Fig. 37. $LiAlSi_2O_6$. Maps of the Laplacian scalar field around O1, O2 and O3 [03P1]. The planes chosen are for O1, Si (on the right side of the map) and Al (upper left corner); O2, Si (right) and Al (upper left); O3 and the two Si ions it coordinates. Contour levels at ± 2, ± 4 and ± $8 \cdot 10^{-n}$ au with n = 0, …., –3. Dashed lines refer to negative values of the Laplacian.

$LiAlSi_2O_6$-III

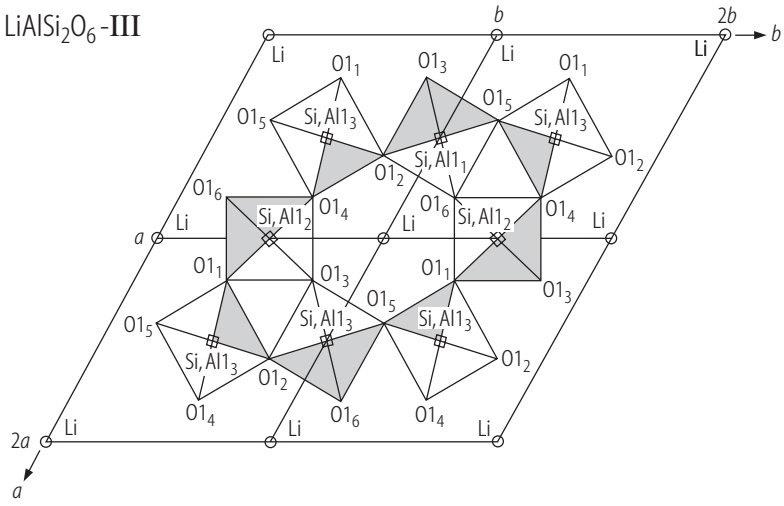

Fig. 38. $LiAlSi_2O_6$-III. Projection of the crystal structure on (001) [68L1].

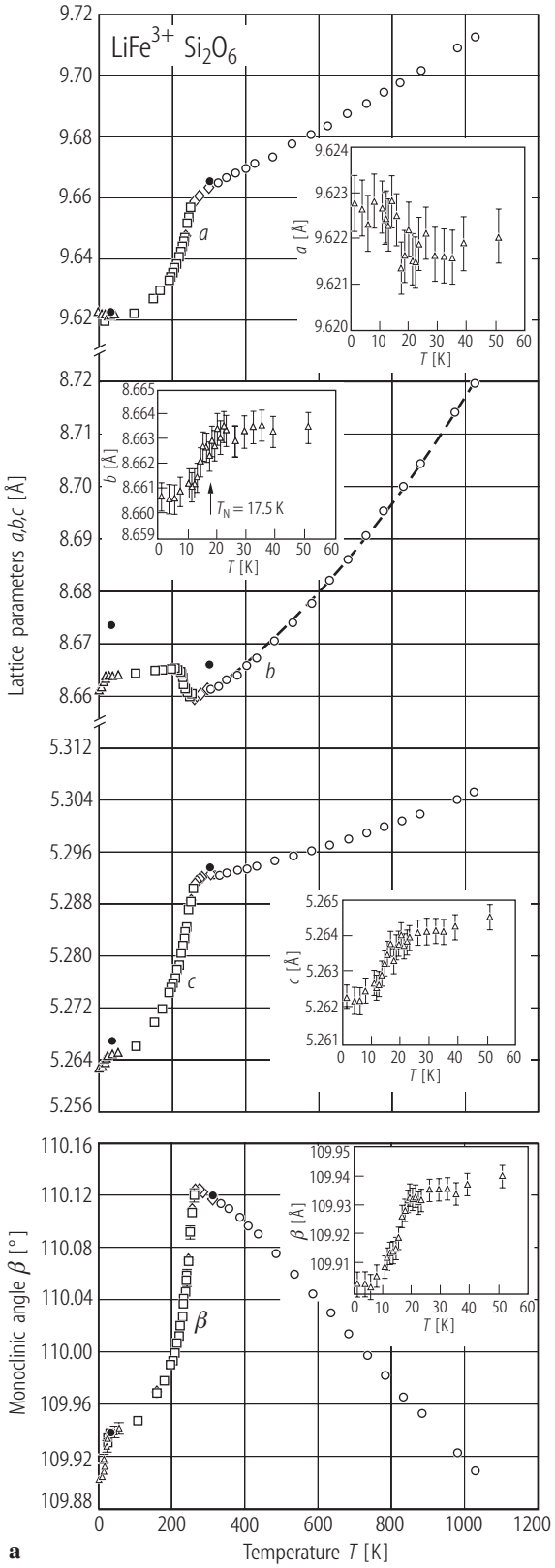

a

Fig. 39. $Li_{1-x}Na_xFeSiO_4$. (**a**) Evolution of the lattice parameters as function of temperature for x = 0 [01R1]. Open circles, diamonds and squares are due X-ray data. Filled circles and open triangles are neutron data. (**b**) Composition dependences of lattice parameters at 298K (**c**) x-*T* phase diagram for the appearance of the C2/c and $P2_1/c$ phases. Only the Li-rich part is shown [02R1].

Fig. 39b, c see next page

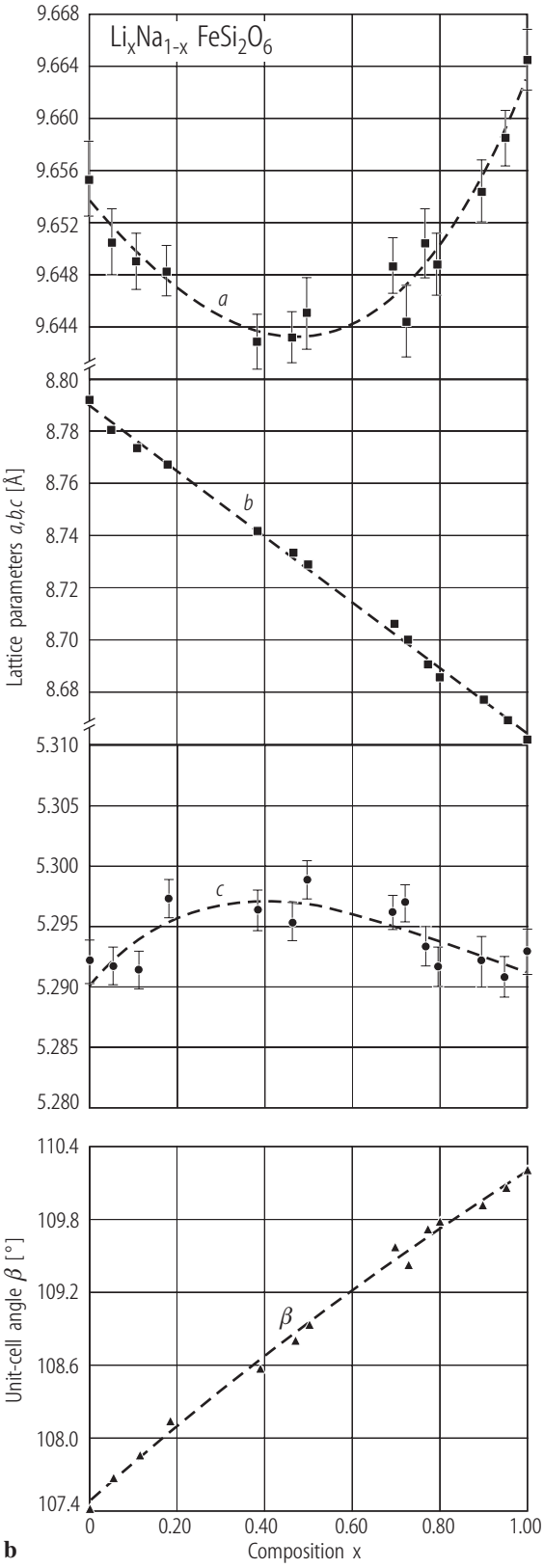

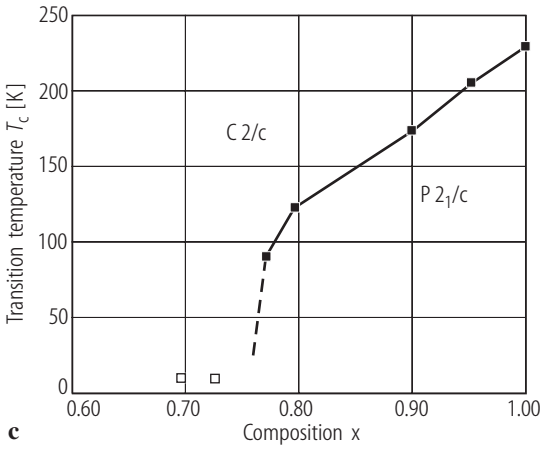

Fig. 39b, c. For caption see previous page

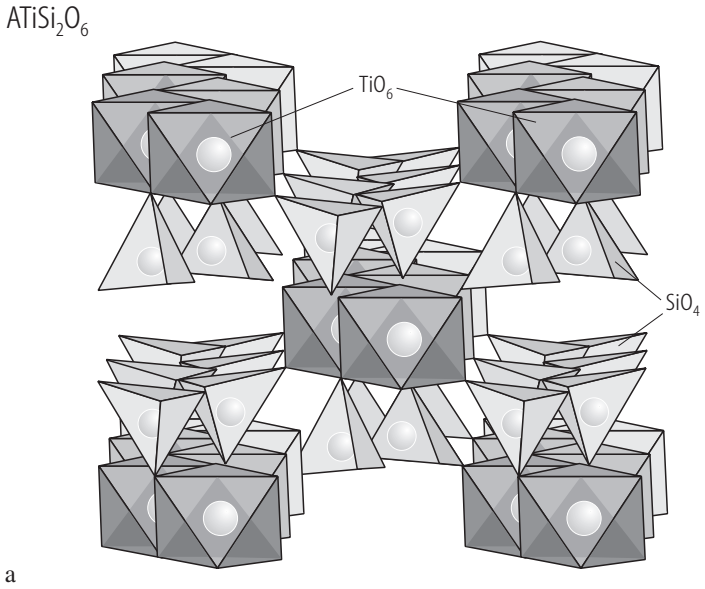

a

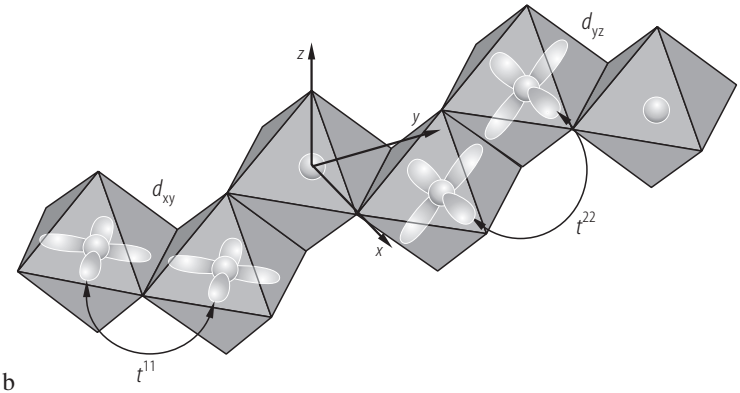

b

Fig. 40. $ATiSi_2O_6$ (A=Na,Li): (**a**) Lattice structure. Chains of TiO_6 octahedra are separated by SiO_4 tetrahedra. (**b**) Skew edge-sharing chain structure of TiO_6 octahedra. Balls in the center of each octahedron denote Ti cations, and oxygen ions are on the corners of the octahedra. The octahedra share their edges in the *xy* and *yz* planes alternatively. White figures with four lobes denote d_{xy} and d_{yz} orbitals of t_{2g} electrons and t^{11} (t^{22}) is the σ-bond transfer integrals between d_{xy} (d_{yz}) orbitals [04H2].

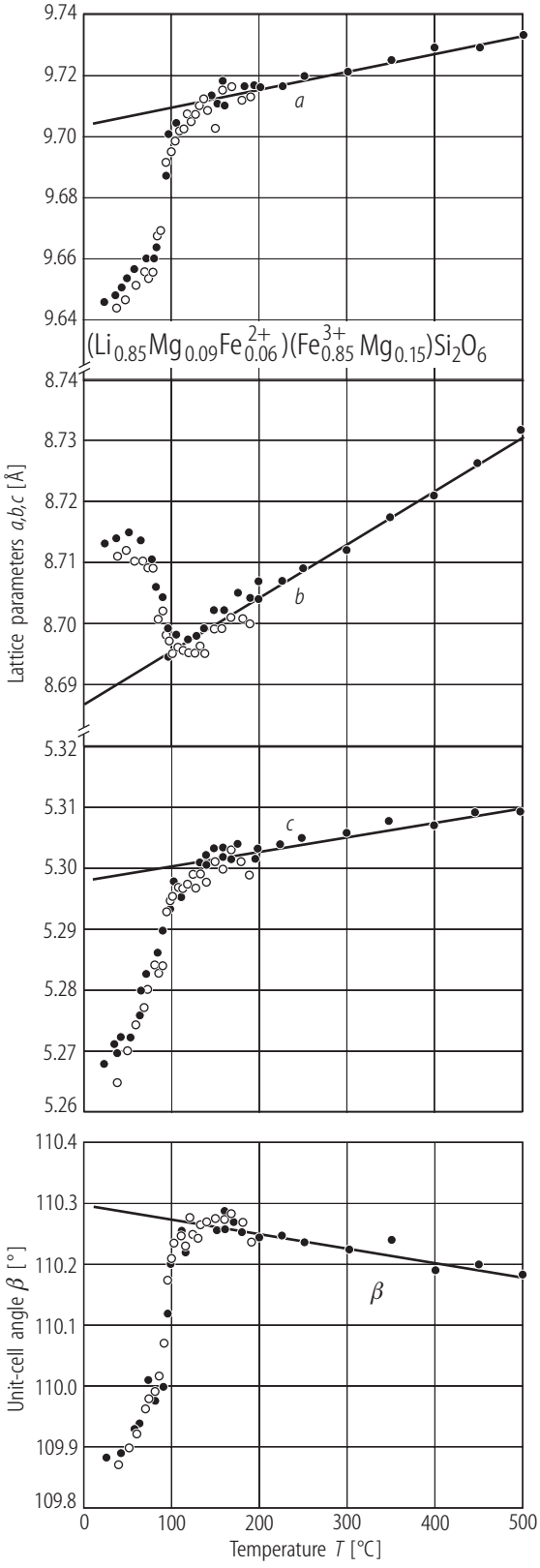

←
Fig. 41. $(Li_{0.85}Mg_{0.09}Fe^{2+}_{0.06})(Fe^{3+}_{0.85}Mg_{0.15})Si_2O_6$. Temperature dependences of the lattice parameters [03C1]. Filled dots (heating), empty dots (cooling). The lines represent regression of the values measured after the transition (T> 130°C).

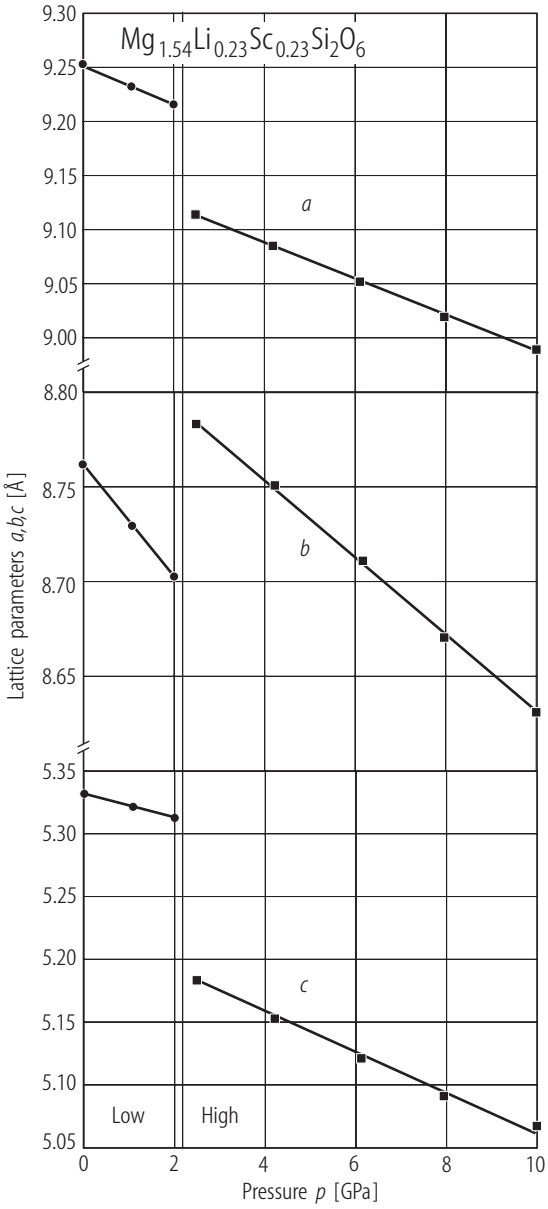

Fig. 42. $Mg_{1.54}Li_{0.23}Sc_{0.23}Si_2O_6$. Pressure dependence of lattice parameters [99Y1].

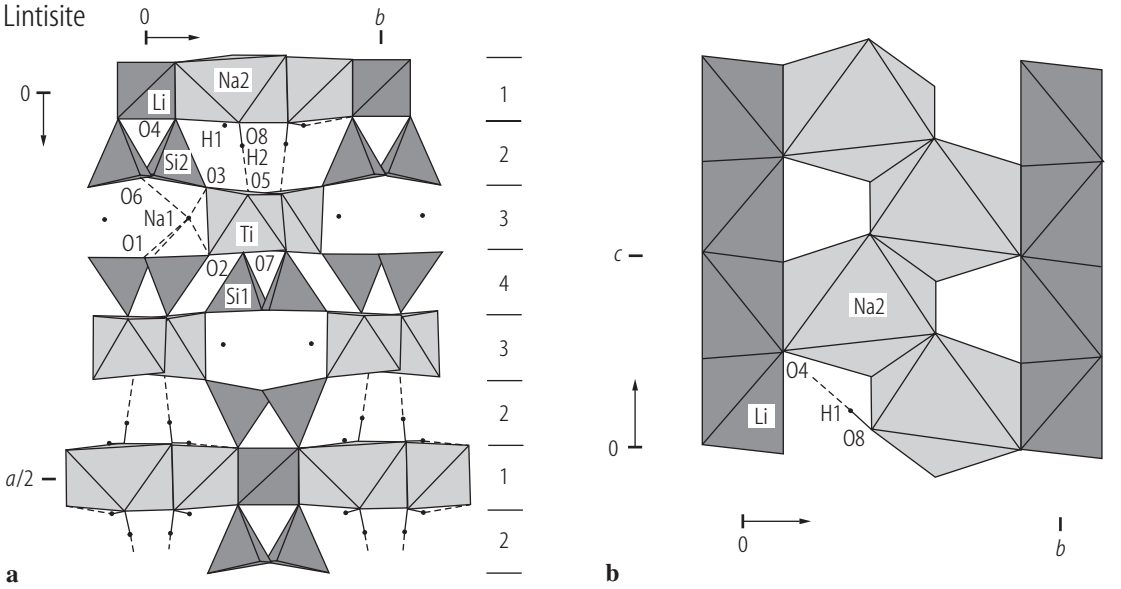

Fig. 43. Lintisite. (**a**) Crystal structure, as seen along [001]. The sequence of slabs, as defined in text, is indicated. (**b**) The structural slab 1, formed by columns of edge sharing [LiO_4] tetrahedra and zig-zag chains of edge-sharing [$Na(O, H_2O)_6$] octahedra, as seen along [100]. From [90M1].

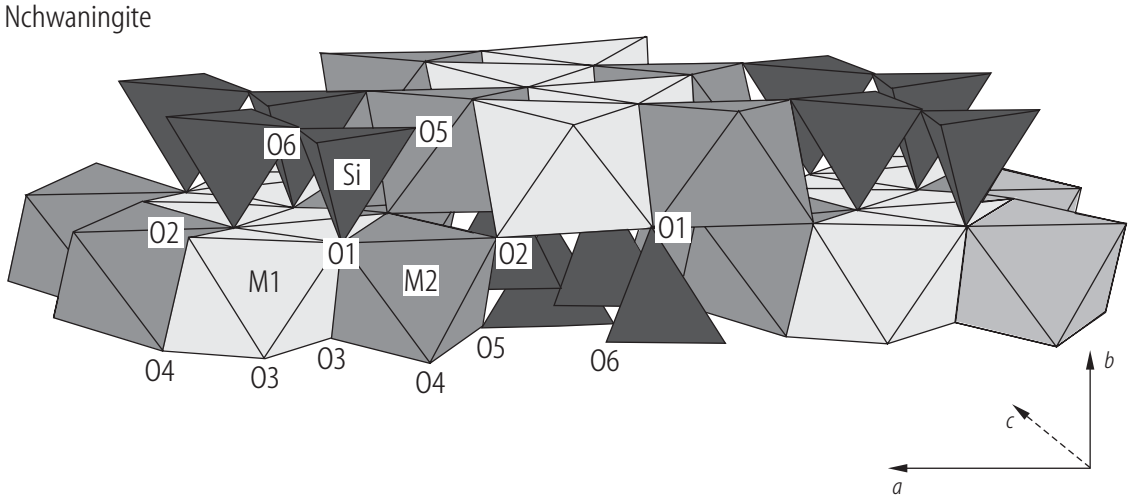

Fig. 44. Nchwaningite. Layer unit of the structure without H atoms. SiO_4 tetrahedra are shown in dark shading. Note the different shading of the two octahedra [95N1].

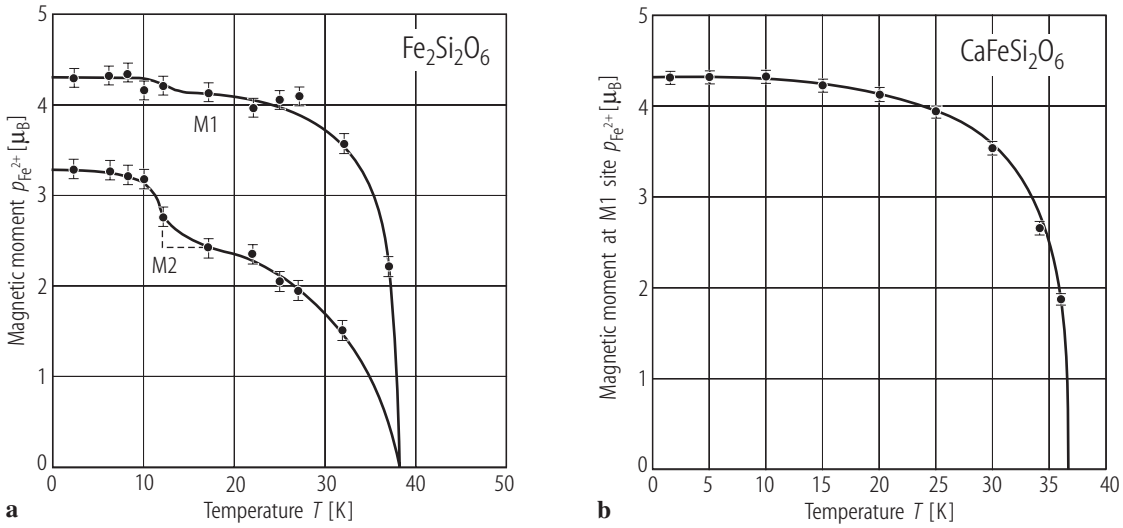

Fig. 45. $Fe_2Si_2O_6$ (**a**) and $CaFeSi_2O_6$ (**b**). In (**a**) the temperature dependences of the magnetic moments at the M1 and M2 sites [88G2] and in (**b**) that of Fe^{2+} magnetic moment at M1 site [88G2] are plotted.

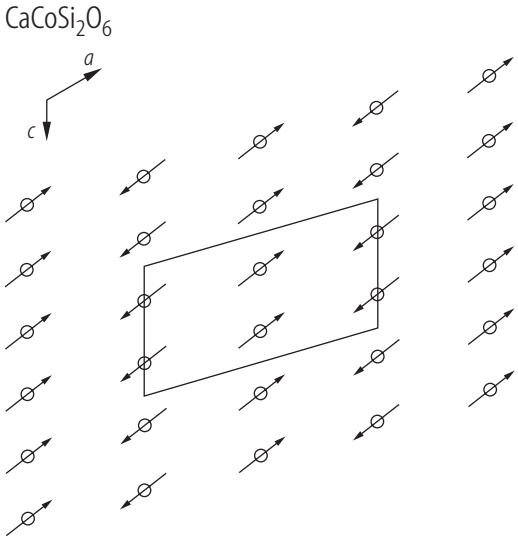

Fig. 46. $CaCoSi_2O_6$. Schematic illustration of the magnetic moment arrangement [96D3].

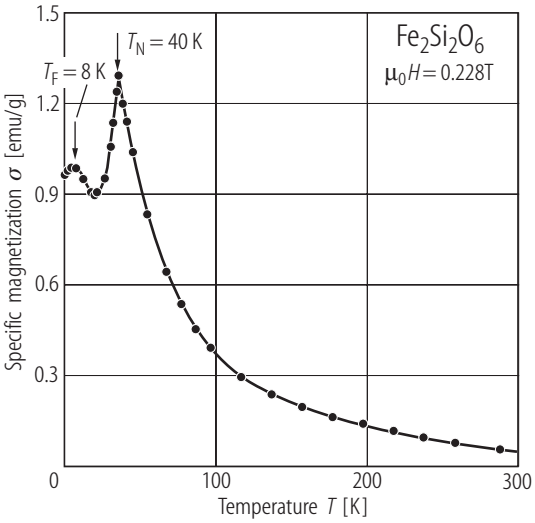

Fig. 48. $Fe_2Si_2O_6$. Temperature dependence of the magnetic susceptibility (specific magnetization) [88G2].

For Fig. 47 see next page

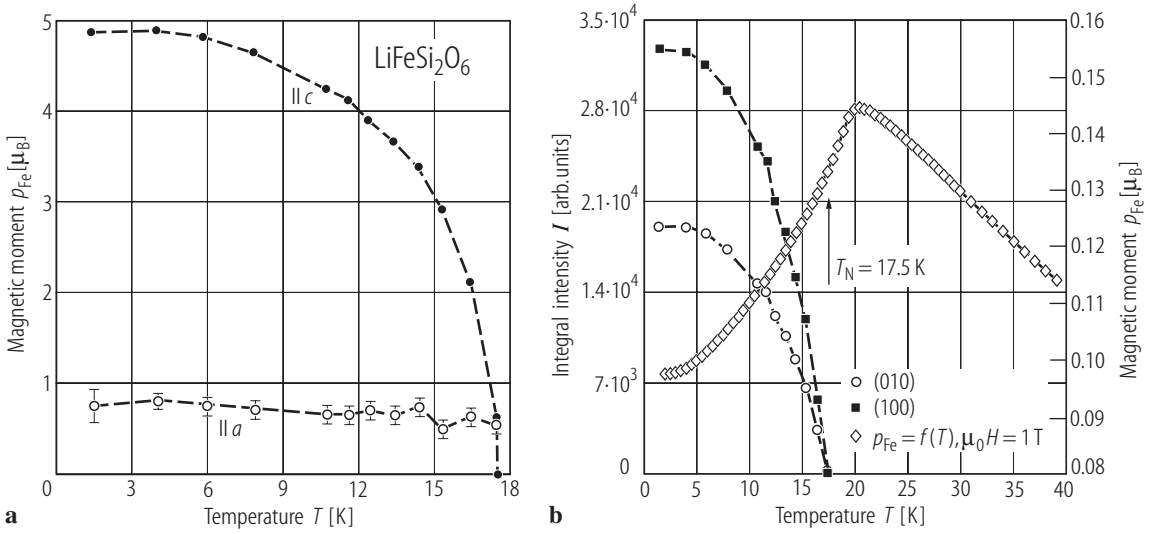

Fig. 47. $LiFeSi_2O_6$. (**a**) Evolution of the components of the magnetic moments (from neutron diffraction) along the axes ***a*** and ***c*** as function of temperature; (**b**) integrated intensity of the magnetic Bragg reflections $(100)_m$ and $(010)_m$ and the magnetic susceptibility (magnetic moment) as function of temperature [01R1].

For Fig. 49 see next page

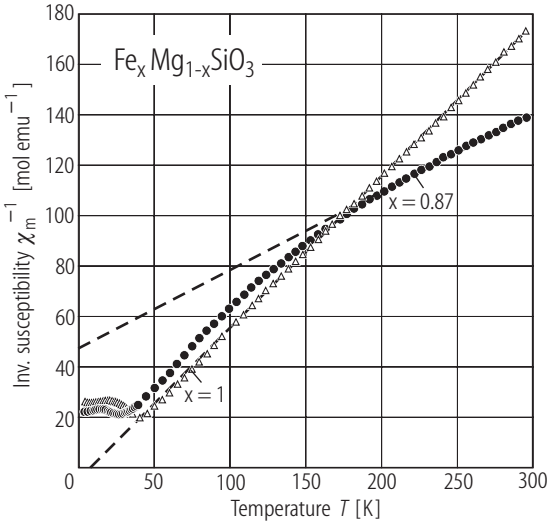

Fig. 50. $Fe_xMg_{1-x}SiO_3$ (x = 1.0 and 0.87) clinopyroxenes. Temperature dependences of the inverse susceptibilities [01E1].

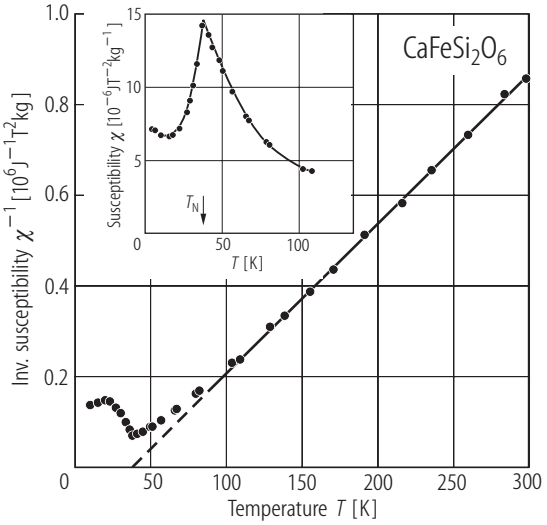

Fig. 51. $CaFeSi_2O_6$. Temperature dependence of the inverse susceptibility. In inset, the temperature dependence of susceptibility at low temperatures is plotted [85C2].

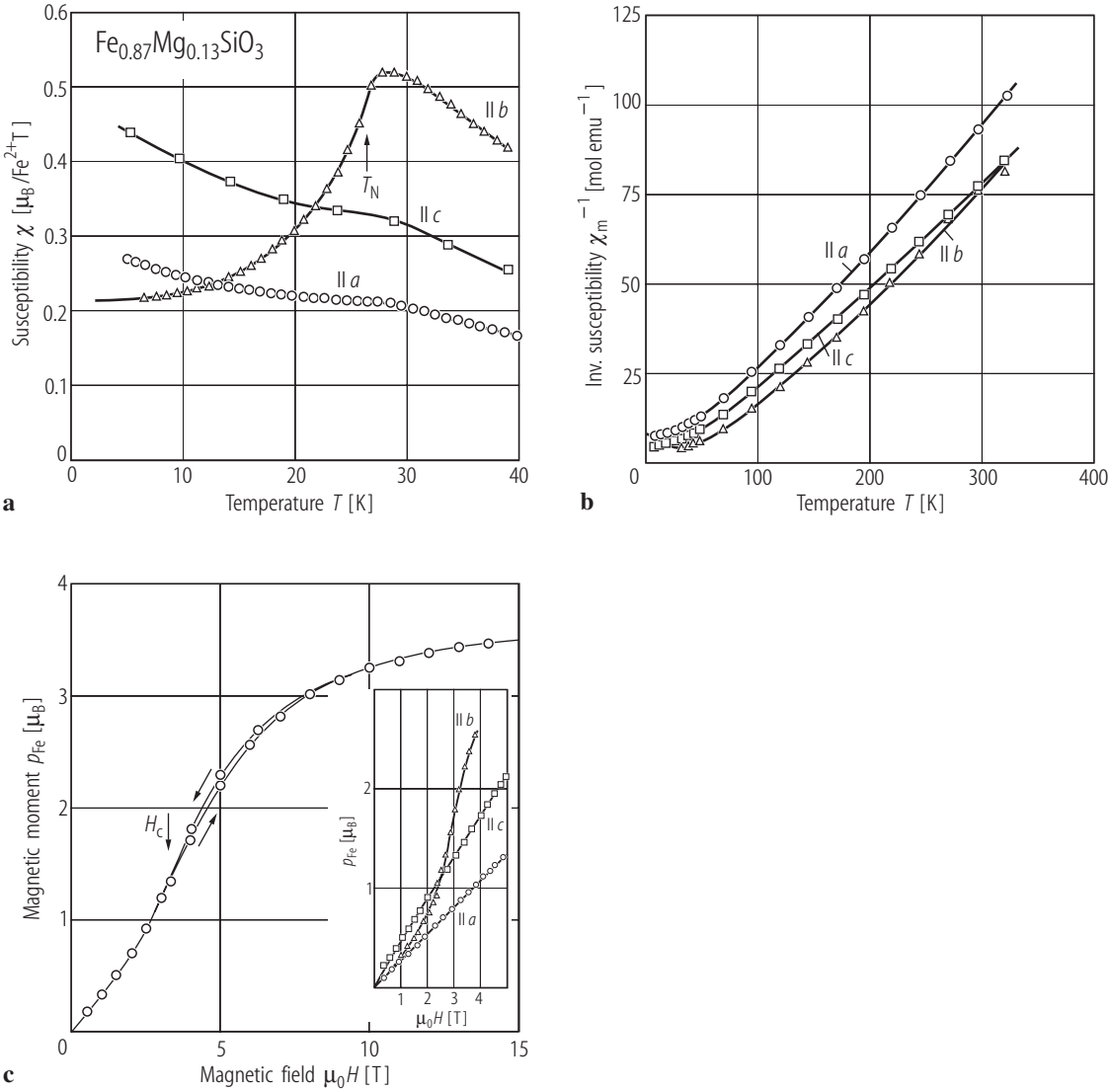

Fig. 49. $Fe_{0.87}Mg_{0.13}SiO_3$ orthopyroxene single crystal. Temperature dependences of (**a**) magnetic susceptibilities along ***a***, ***b*** and ***c***-axes, (**b**) inverse susceptibilities. In (**c**) the high-field magnetization isotherm for a powder sample at 4.2 K is plotted. The inflexion point defines the critical field, H_c, of the metamagnetic transition. In inset of (**c**), the magnetization curves for a single crystal along ***a***, ***b*** and ***c*** axis are plotted [86W4].

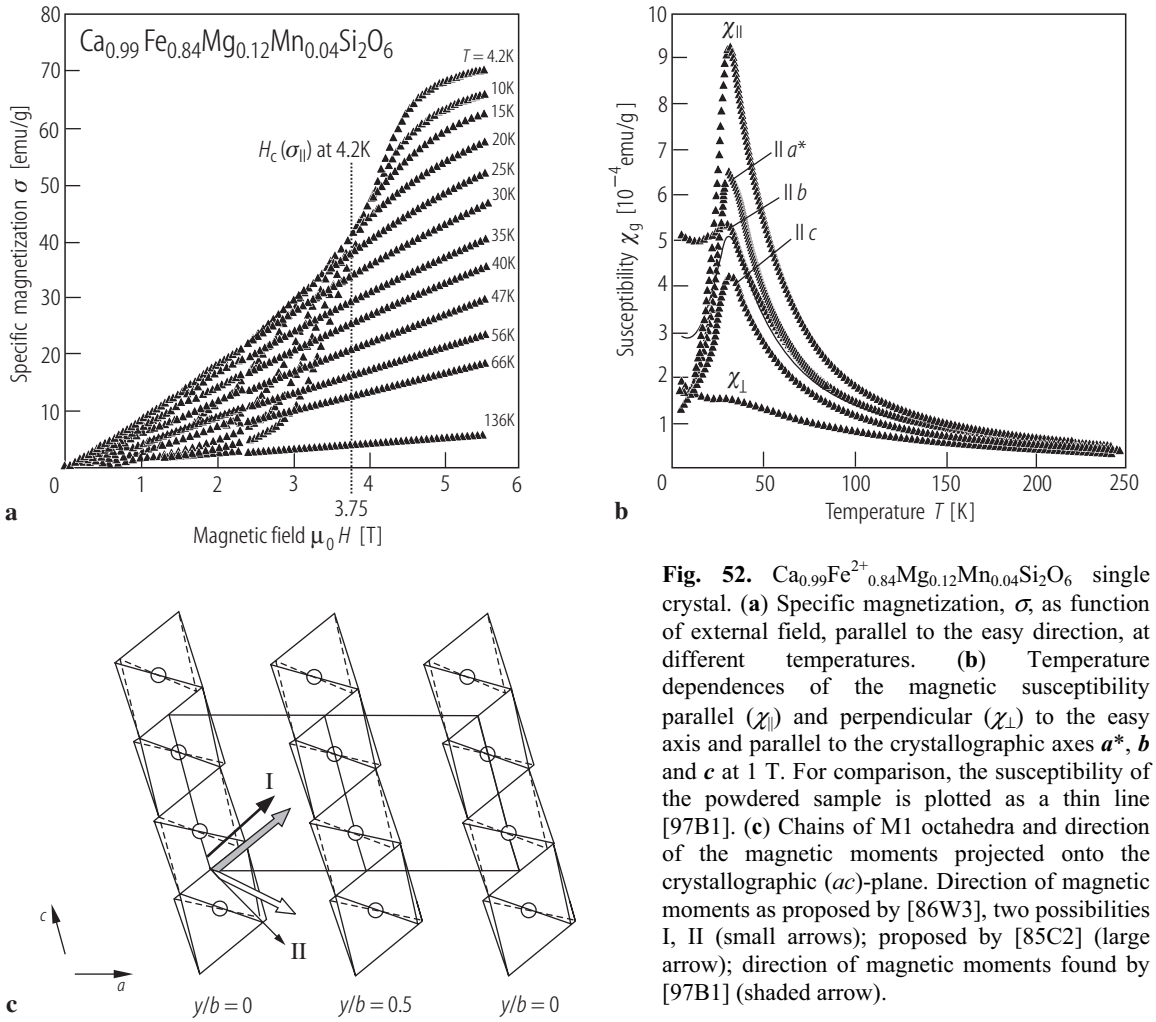

Fig. 52. $Ca_{0.99}Fe^{2+}_{0.84}Mg_{0.12}Mn_{0.04}Si_2O_6$ single crystal. (**a**) Specific magnetization, σ, as function of external field, parallel to the easy direction, at different temperatures. (**b**) Temperature dependences of the magnetic susceptibility parallel ($\chi_{\|}$) and perpendicular ($\chi_{\perp}$) to the easy axis and parallel to the crystallographic axes ***a****, ***b*** and ***c*** at 1 T. For comparison, the susceptibility of the powdered sample is plotted as a thin line [97B1]. (**c**) Chains of M1 octahedra and direction of the magnetic moments projected onto the crystallographic (*ac*)-plane. Direction of magnetic moments as proposed by [86W3], two possibilities I, II (small arrows); proposed by [85C2] (large arrow); direction of magnetic moments found by [97B1] (shaded arrow).

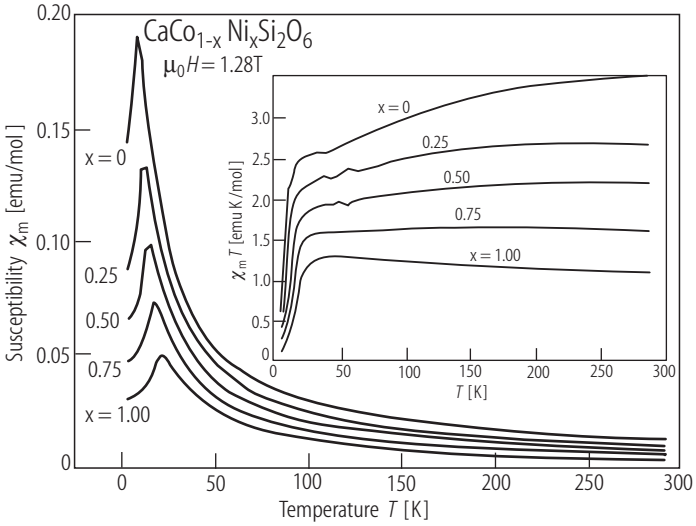

Fig. 53. $CaCo_{1-x}Ni_xSi_2O_6$. Temperature dependences of the magnetic susceptibilities as well as of the $\chi_m T$ product in a field $\mu_o H$ = 1.28 T [96D3].

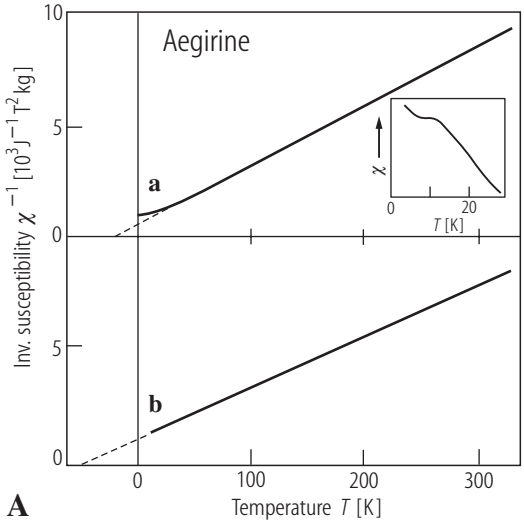

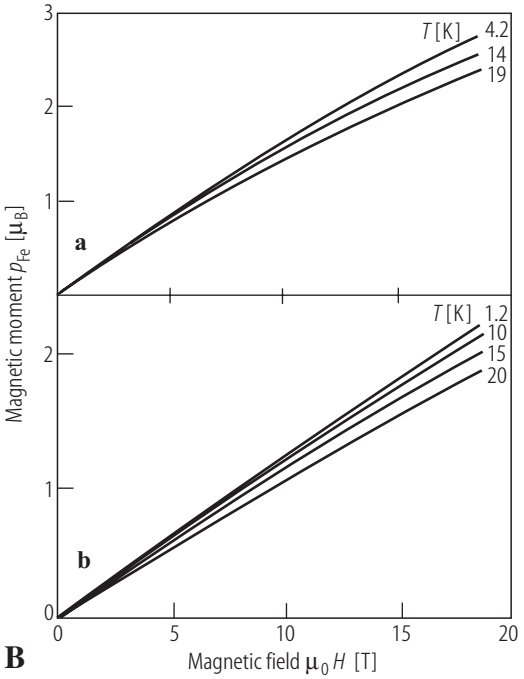

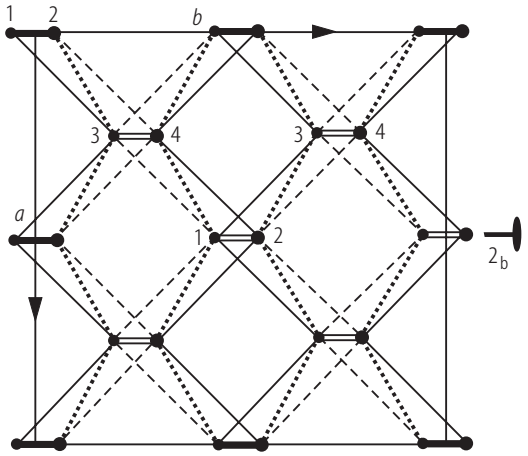

Fig. 54. Aegirine, natural (**a**) and synthetic (**b**). (**A**) Temperature dependences of the inverse susceptibilities (in J/T^2 kg units). The insert shows the susceptibility around the magnetic ordering point. (**B**) Magnetic moment p_{Fe} isotherms at various temperatures. (**C**) Exchange couplings. Four unit cells as represented, projected along the ***c***-axis. The intrachain exchange parameter J_{12}(=) corresponds to direct and Fe-O-Fe indirect exchange. The interchain parameters J'_{13} (solid lines) and J''_{13} (dashed lines) correspond to Fe-O-Si-O-Fe indirect exchange within planes parallel to the (*ab*)-plane, and J_{14} (dotted lines) to Fe-O-Si-O-Fe indirect exchange between ions which belong to different *z*-levels. The M1-positions which are indicated by the bigger dots are at the level 3/4, while the others lie in the z = 1/4 plane. Note the frustrating triangles 134 and 234 [89B1].

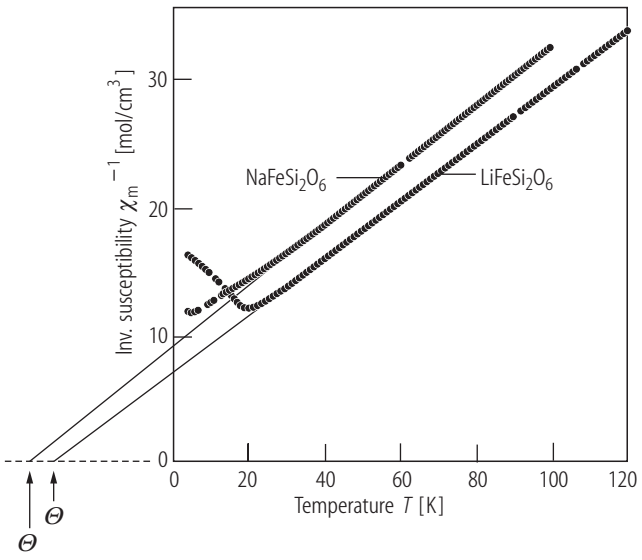

Fig. 55. $NaFeSi_2O_6$, $LiFeSi_2O_6$. Inverse magnetic susceptibilities as function of temperature [88B1].

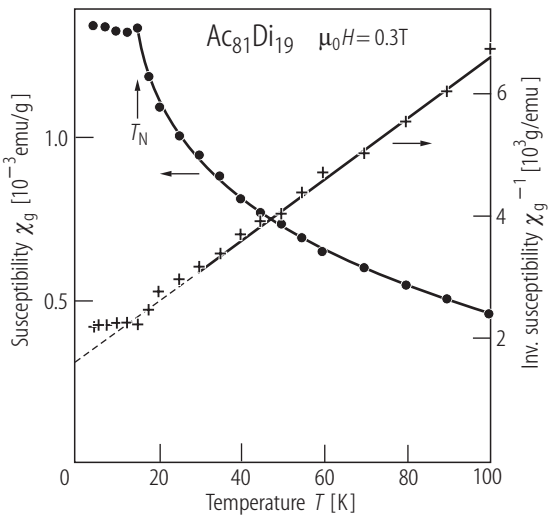

Fig. 56. $Ac_{81}Di_{19}$. Temperature dependence of the magnetic susceptibility and their reciprocal values [88D1].

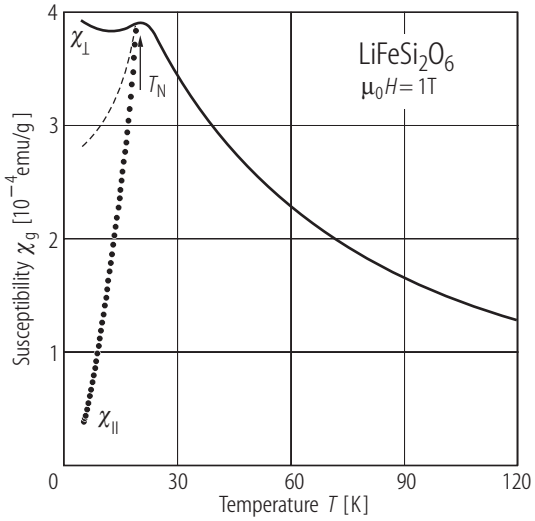

Fig. 57. $LiFeSi_2O_6$. Magnetic susceptibilities parallel ($\chi_\parallel$) and perpendicular ($\chi_\perp$) to the ***c***-axis in the field of 1 T. For comparison, the susceptibility of the powdered sample is plotted as dashed line [88B1].

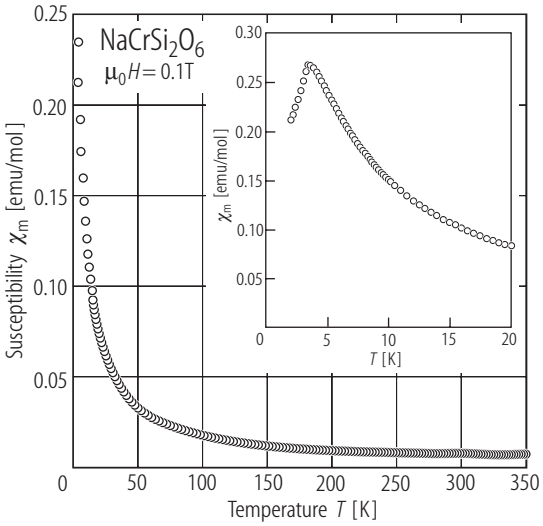

Fig. 60. $NaCrSi_2O_6$. Temperature dependence of the magnetic susceptibility. The low-temperature region is enlarged in the inset [04I1].

For Figs. 58, 59 see next page

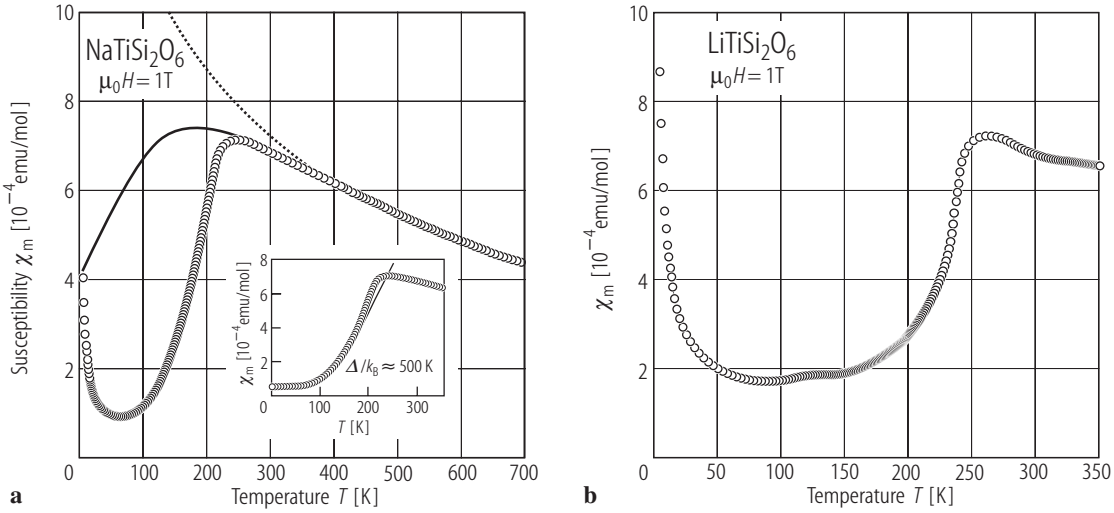

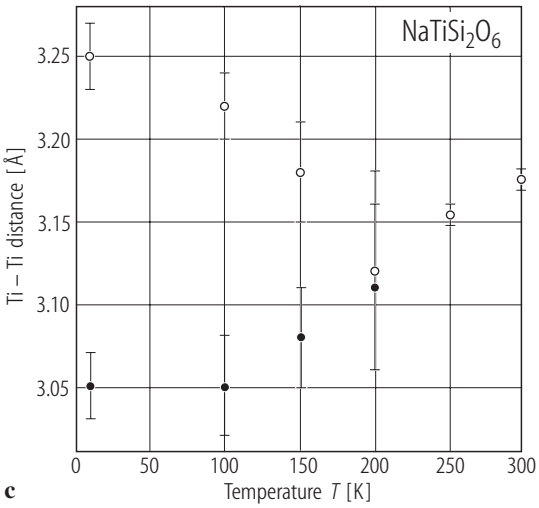

Fig. 58. $NaTiSi_2O_6$(**a**), $LiTiSi_2O_6$(**b**). Temperature dependences of the magnetic susceptibilities [02I1]. In (**a**) the inset shows the magnetic susceptibility by subtracting the contribution due to possible impurities. The dotted line is a Curie-Weiss curve for $C = 0.375$ emu K/mol and $\Theta = -255$ K; the solid line is a Bonner-Fisher curve for $g = 2.0$ and $J/k_B = 295$ K. In (**c**) the distances between Ti ions along chains in $NaTiSi_2O_6$ as function of temperature is plotted [03N1].

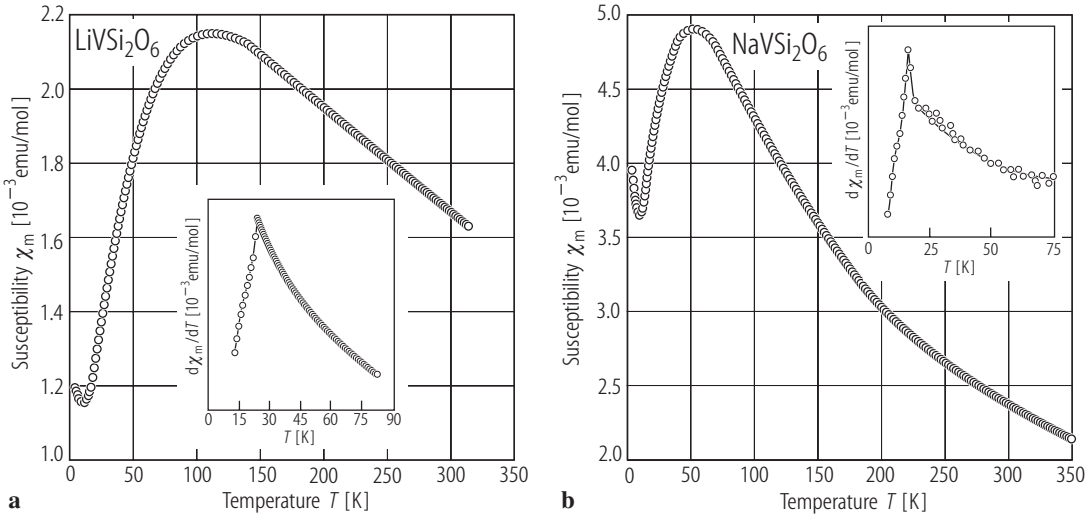

Fig. 59. $LiVSi_2O_6$(**a**), $NaVSi_2O_6$ (**b**). Temperature dependences of the magnetic susceptibilities [04V1].

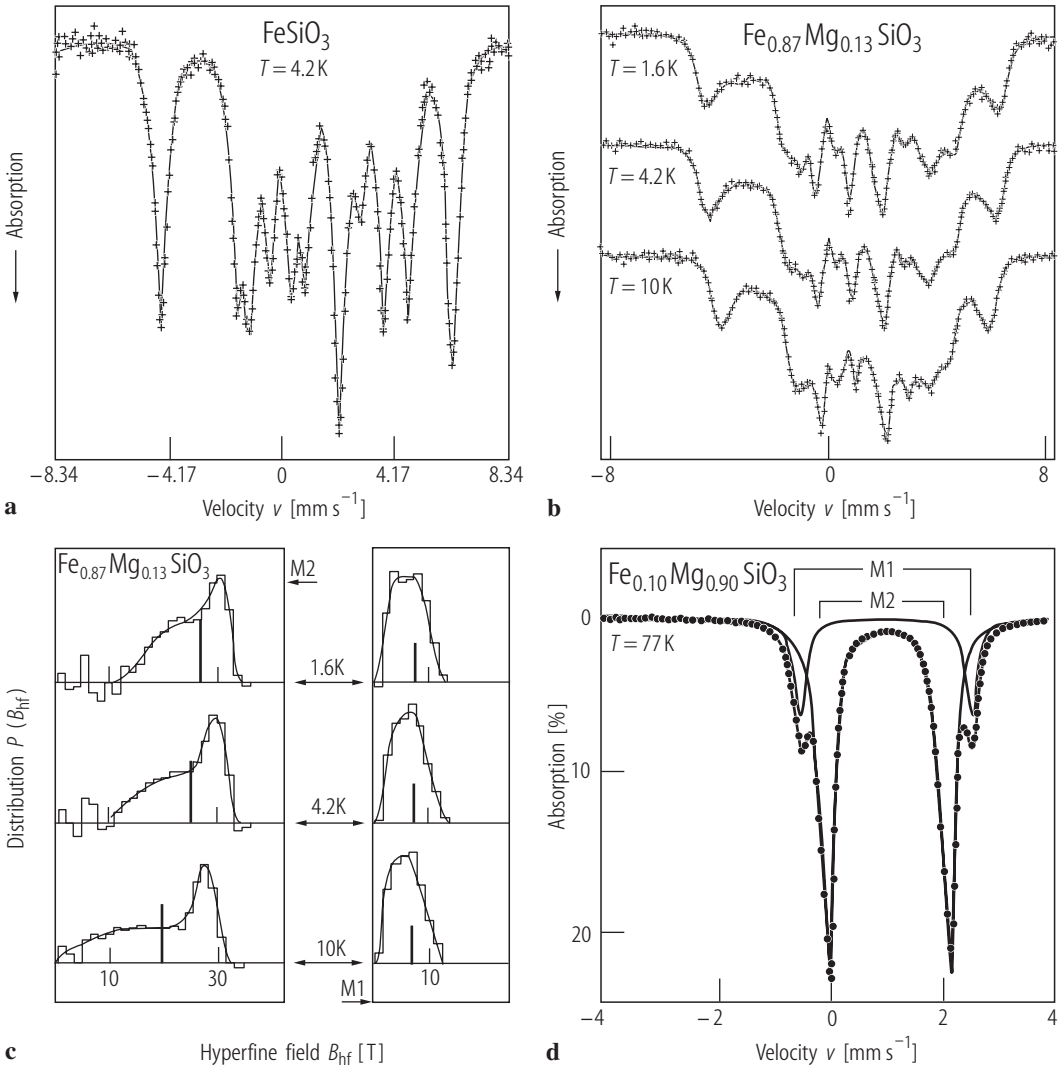

Fig. 61. $Fe_xMg_{1-x}SiO_3$ OPx (space group Pbca). ^{57}Fe NGR spectra (**a**) $FeSiO_3$ at 4.2 K [86W4]; (**b**) $Fe_{0.87}Mg_{0.13}SiO_3$ at 1.6 K, 4.2 K and 10 K. Full traces represent the best fits of the spectra using a discrete distribution of hyperfine fields, $P(B_{hf})$; (**c**) histograms showing the hyperfine field distributions, $P(B_{hf})$ for Fe^{2+} in the M1 and M2 sites, at different temperatures for same sample as in (**b**). The full curves result from a smoothing procedure. Vertical bars represent mean hyperfine field [87R1]. In (**d**) the spectrum of the sample with x = 0.10 at 77 K is plotted [94F2]. Solid line through data points is a least square fit.

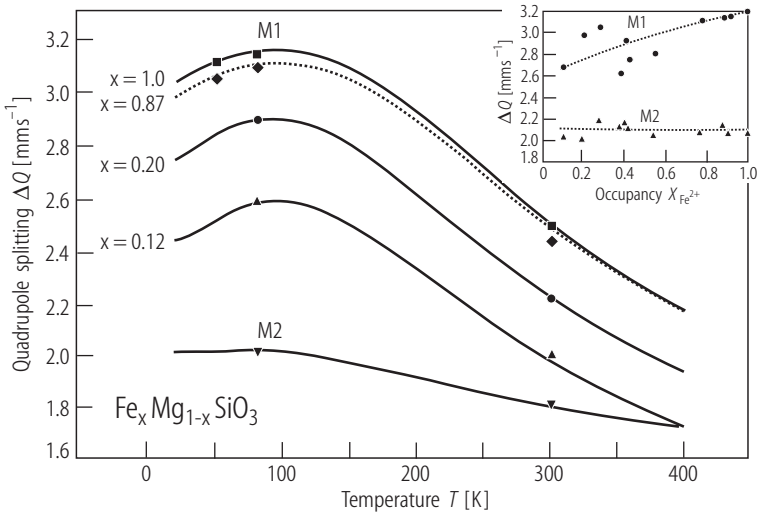

Fig. 62. $Fe_xMg_{1-x}SiO_3$ with x = 1.00, 0.87, 0.20, 0.12. Quadrupole splitting as function of temperature. In inset the ΔQ values as function of occupancy are plotted [86S1, 86W4, 01V1].

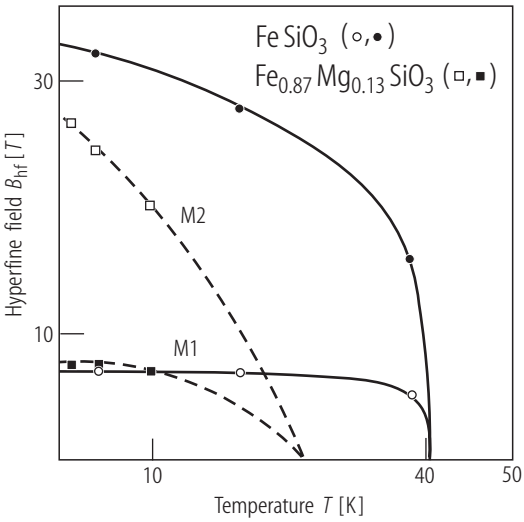

Fig. 63. $FeSiO_3$, $Fe_{0.87}Mg_{0.13}SiO_3$. Temperature dependences of the hyperfine fields in the M1 and M2 sites ($FeSiO_3$) and the corresponding mean values $<B_{hf}$ (M1)> and $<B_{hf}$(M2)> in $Fe_{0.87}Mg_{0.13}SiO_3$ [87R1].

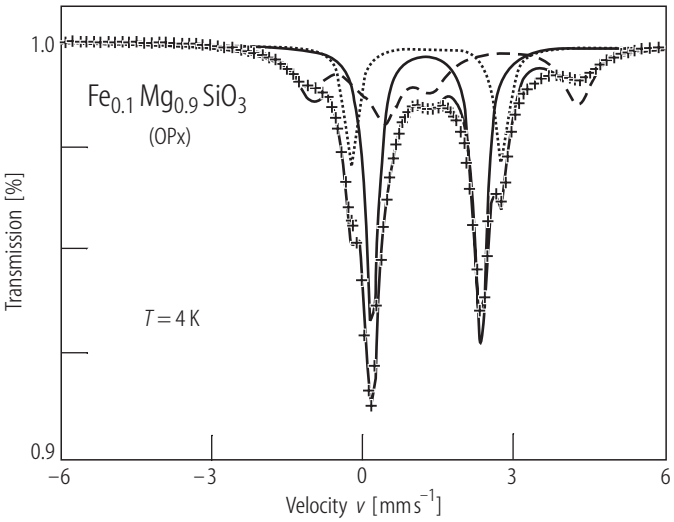

Fig. 64. $Fe_{0.1}Mg_{0.9}SiO_3$ OPx. ^{57}Fe NGR spectrum at 4 K [92P1]. The computed subspectra correspond to nonmagnetic M1, nonmagnetic M2 and magnetic M2m sites, respectively – Table 10. The magnetic interactions are due to spin-spin relaxation, but the fitting was performed assuming a static field with artificially broad lines.

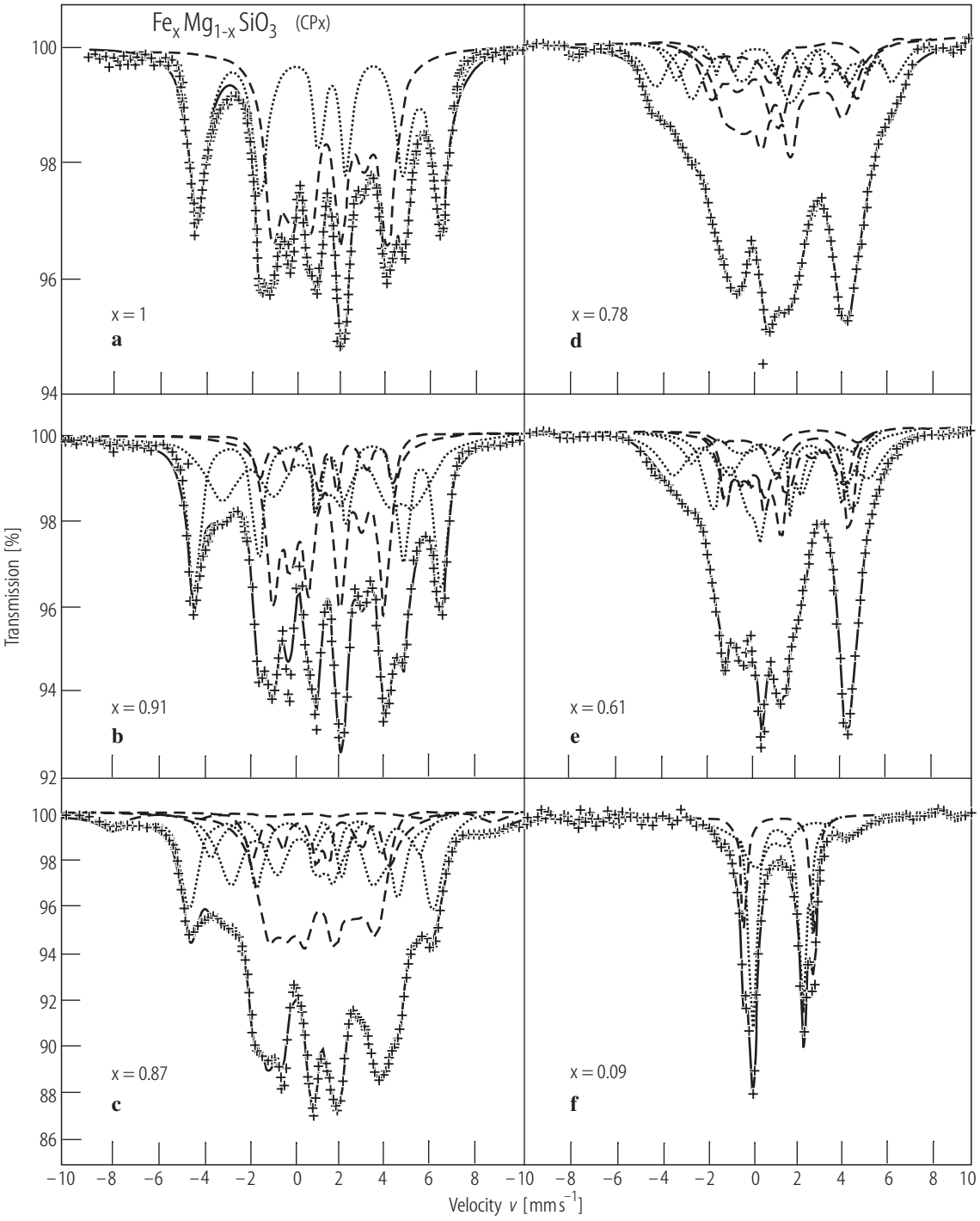

Fig. 65. $Fe_xMg_{1-x}SiO_3$ CPx (space group $P2_1/c$). ^{57}Fe NGR spectra, experimental (crosses) and calculated (solid lines): (**a**) $FeSiO_3$ at 4.2 K; (**b**) $Mg_{0.09}Fe_{0.91}SiO$ at 0.3 K; (**c**) $Mg_{0.13}Fe_{0.87}SiO_3$ at 4.2 K; (**d**) $Mg_{0.22}Fe_{0.78}SiO_3$ at 0.3 K; (**e**) $Mg_{0.39}Fe_{0.61}siO_3$ at 0.3 K; (**f**) $Mg_{0.91}Fe_{0.09}SiO_3$ at 4.2 K. The dashed lines represent the distinct M1 components and the dotted lines the M2 components [01E1].

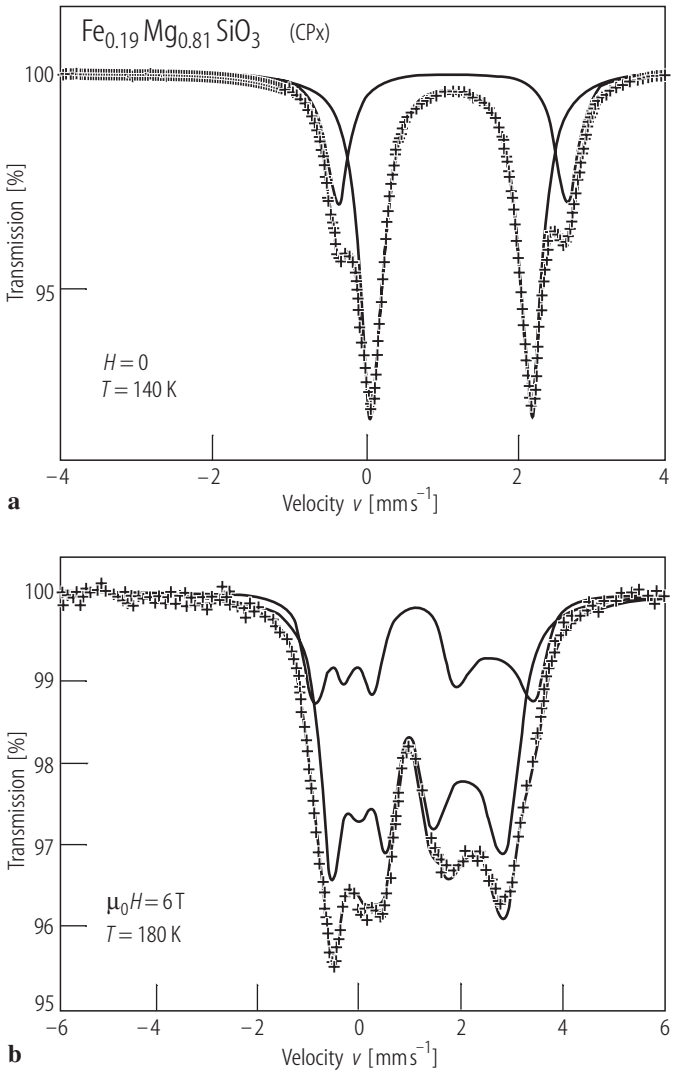

Fig. 66. $Fe_{0.19}Mg_{0.81}SiO_3$ CPx at 140 K and $\mu_o H = 0$ (**a**) and at 180 K in a field of 6 T (**b**) [00E1]. Solid lines represent the calculated subspectra and their superposition.

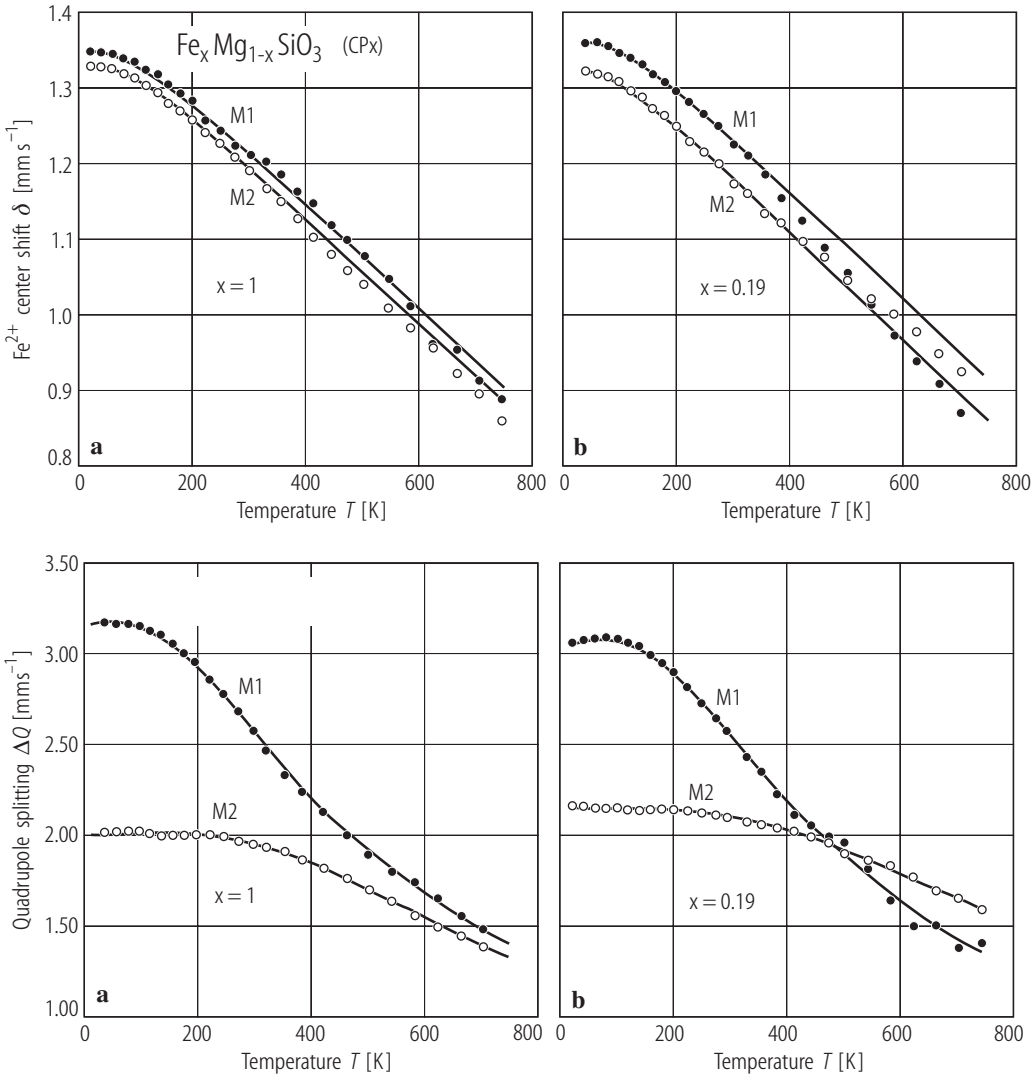

Fig. 67. $FeSiO_3$ (**a**); $Fe_{0.19}Mg_{0.81}SiO_3$ (**b**). Temperature dependences of the center shifts (upper figures) and quadrupole splitting (lower figures). In the lower figures the solid lines represent the theoretical curves calculated from the static crystal field model [00E1].

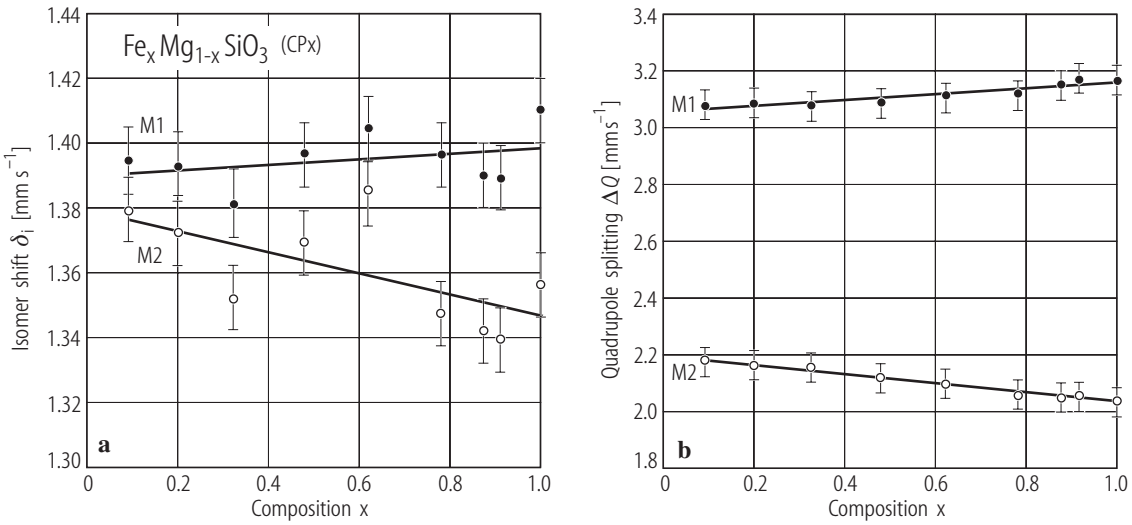

Fig. 68. $Fe_xMg_{1-x}SiO_3$ CPx. (**a**) Intrinsic isomer shift determined from the Debye model and (**b**) quadrupole splitting, ΔQ, measured at 40 K as function of composition [00E1].

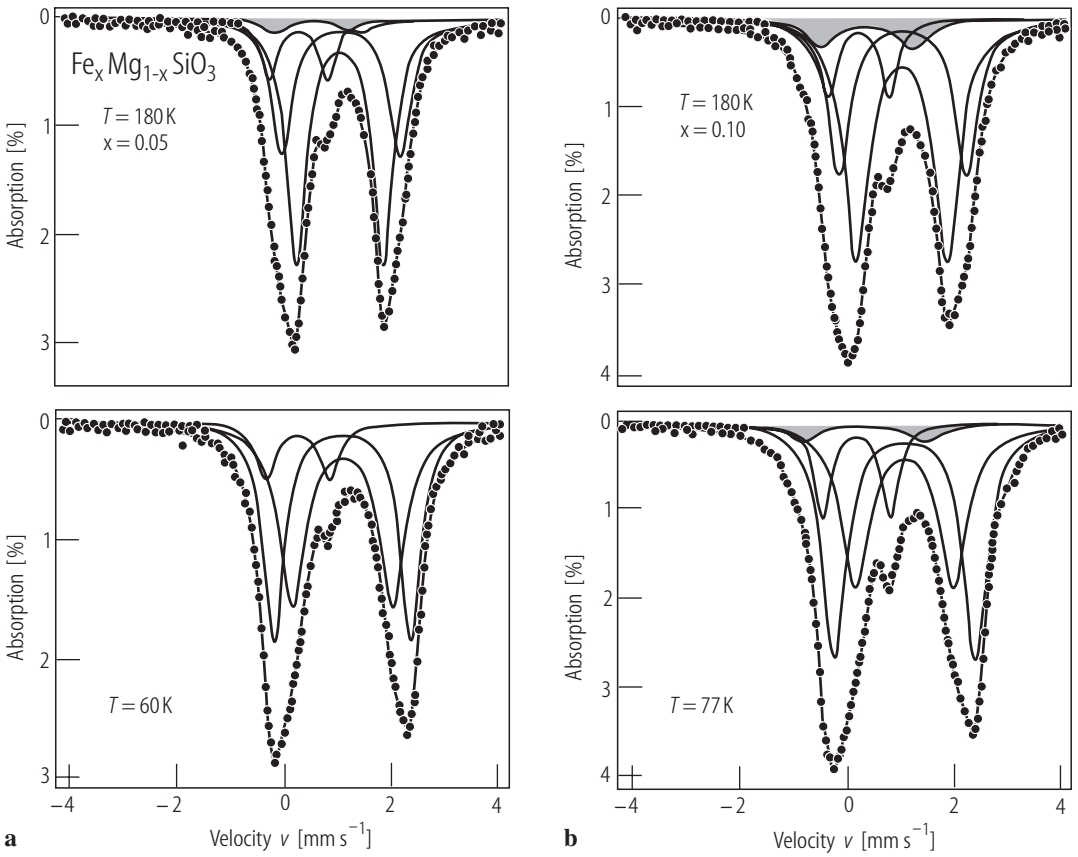

Fig. 69. $Fe_xMg_{1-x}SiO_3$ perovskite. ^{57}Fe NGR spectra of samples with x = 0.05 (**a**) and x = 0.10 (**b**) at two different temperatures [94F2]. The shaded area indicates the absorption due to electron delocalization. The solid line through data points is a least-squares fit.

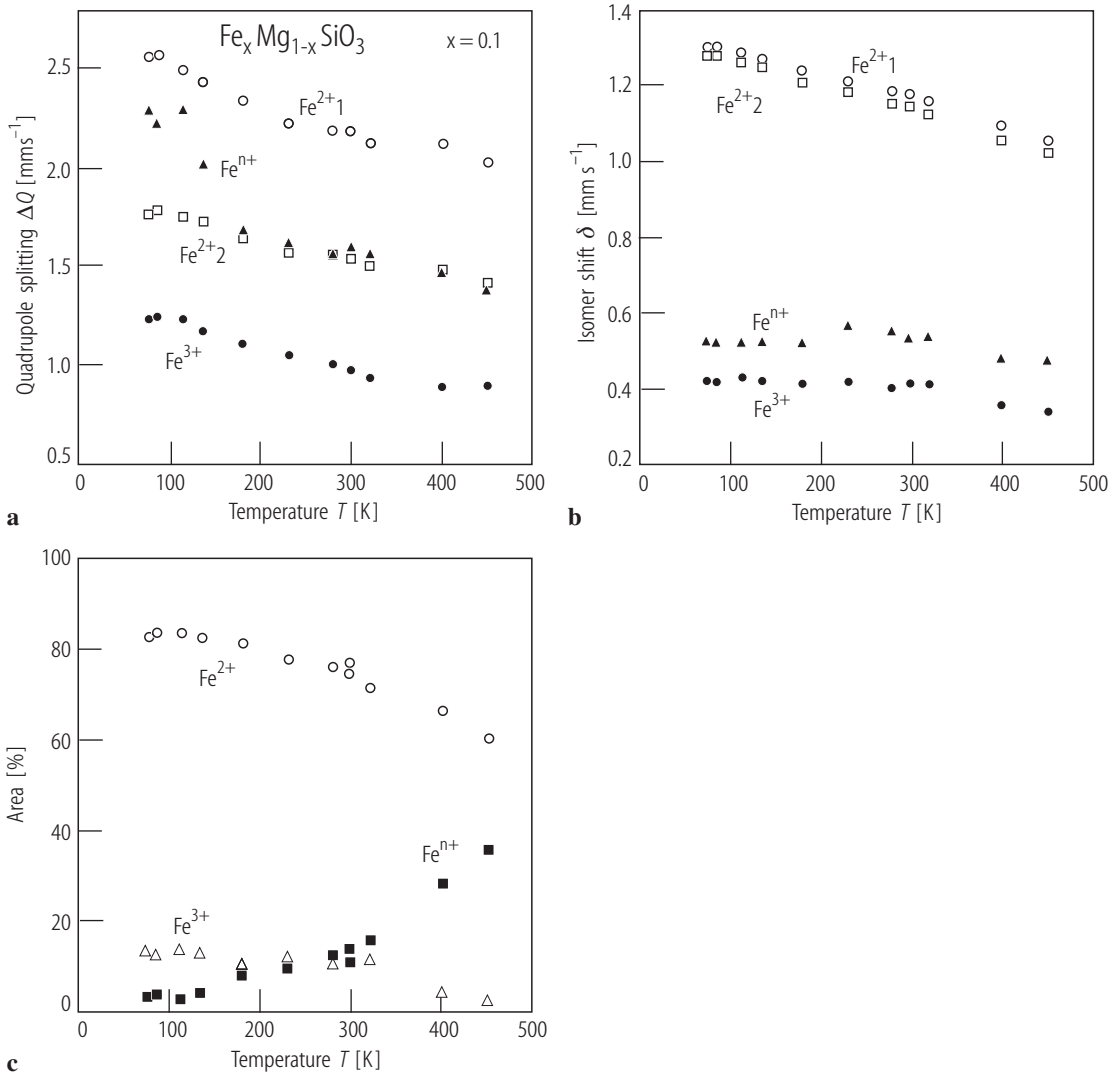

Fig. 70. $Fe_xMg_{1-x}SiO_3$ perovskite. The temperature dependences of quadrupole splitting (**a**) and isomer shift (**b**) for x = 0.10 samples. In (**c**) the temperature dependences of the relative area of the doublets are shown [94F2].

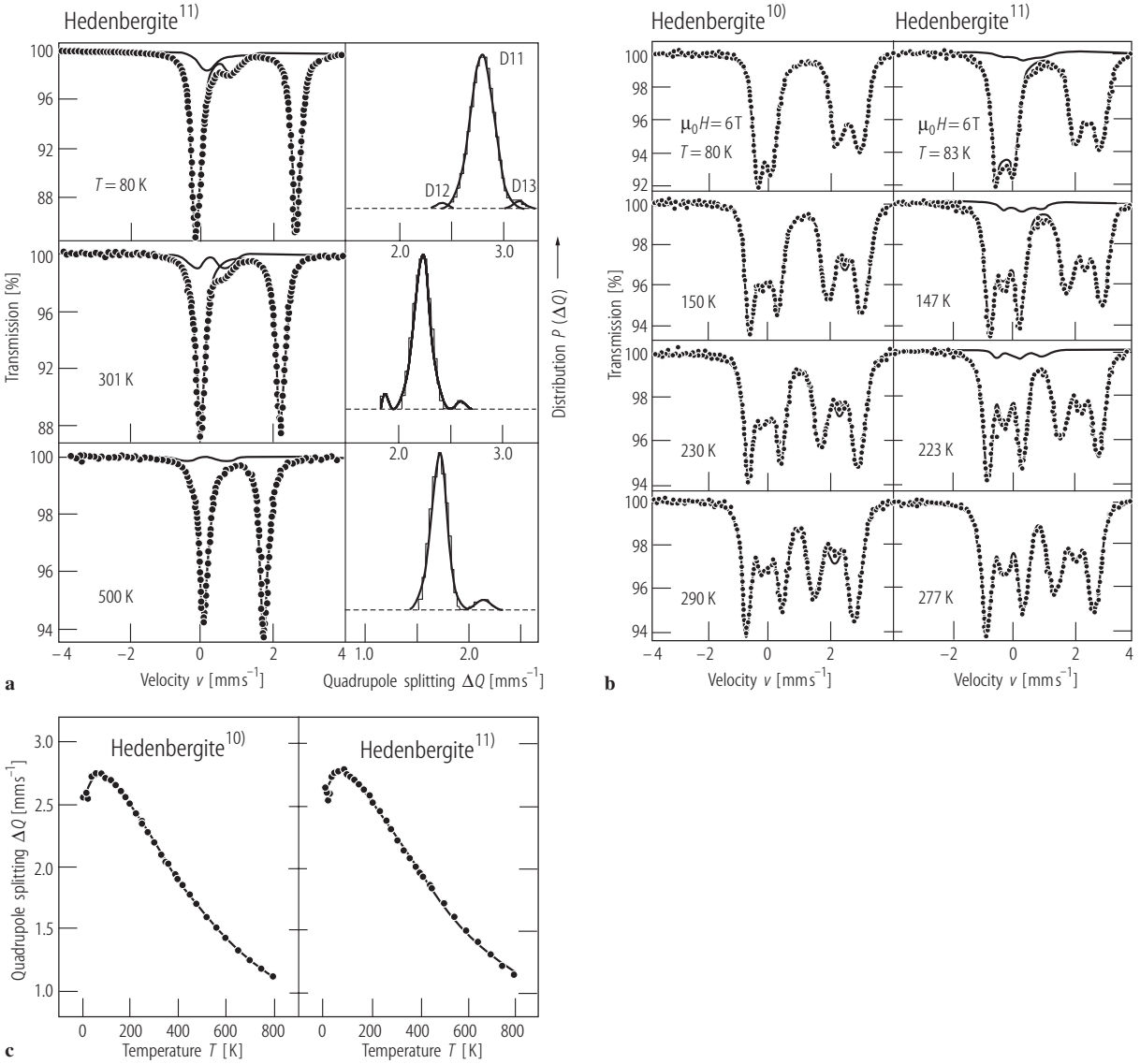

Fig. 71. Hedenbergite. (**a**) Experimental (dots) and calculated (solid lines) ^{57}Fe NGR spectra and the corresponding ferrous QSD for sample[11)]. In (**b**) the spectra for samples[10)] (left) and[11)] (right) in field $\mu_0 H$ = 6 T are given. The temperature dependences of the quadrupole splittings (for sample[10)] and sample[11)]) are shown in (**c**) [03E1]. For composition of samples [10)], [11)] see Table 10.

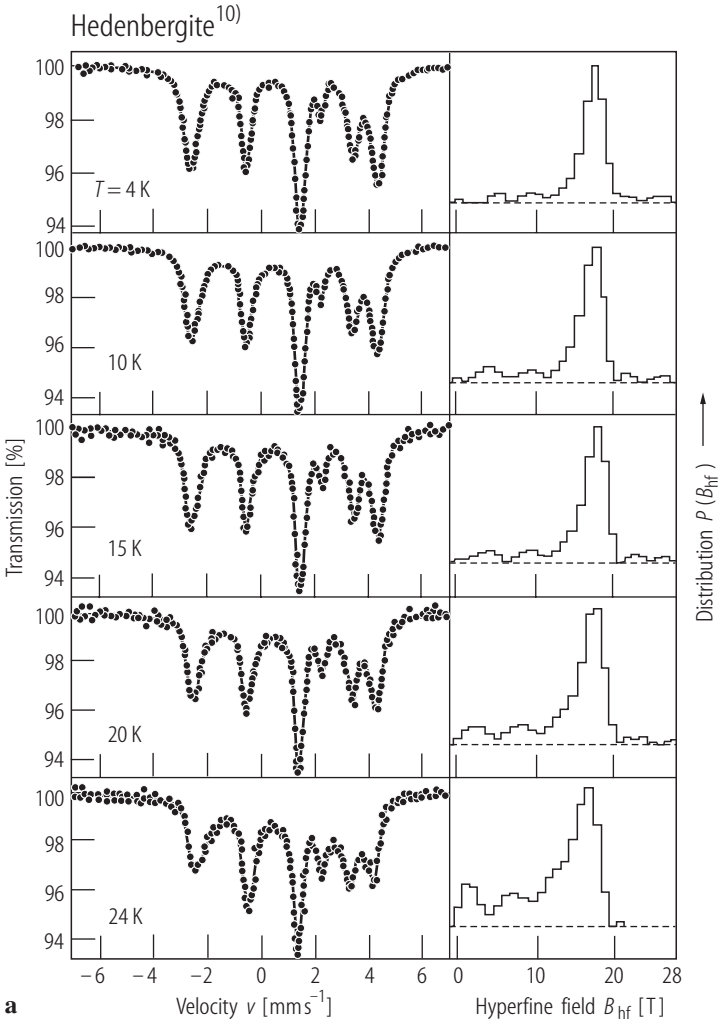

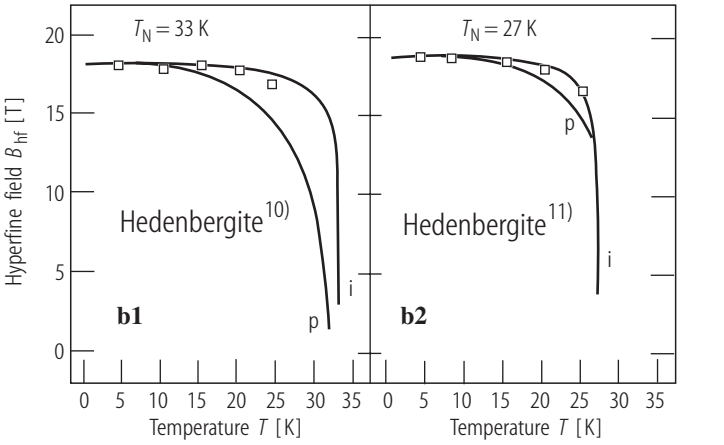

Fig. 72. Hedenbergite. (**a**) Experimental (circles) and calculated (solid lines) ^{57}Fe NGR spectra and the corresponding hyperfine field, B_{hf}, distribution at $T < T_N$, for sample[10)]. (**b**) Experimental (open squares) and calculated (solid lines) temperature dependence of B_{hf} values using the point charge approach (p curves) and the two-dimensional rectangular Ising model (i curves) for sample[10)] (b1) and sample[11)] (b2) [03E2]. For composition of samples [10), 11)] see Table 10.

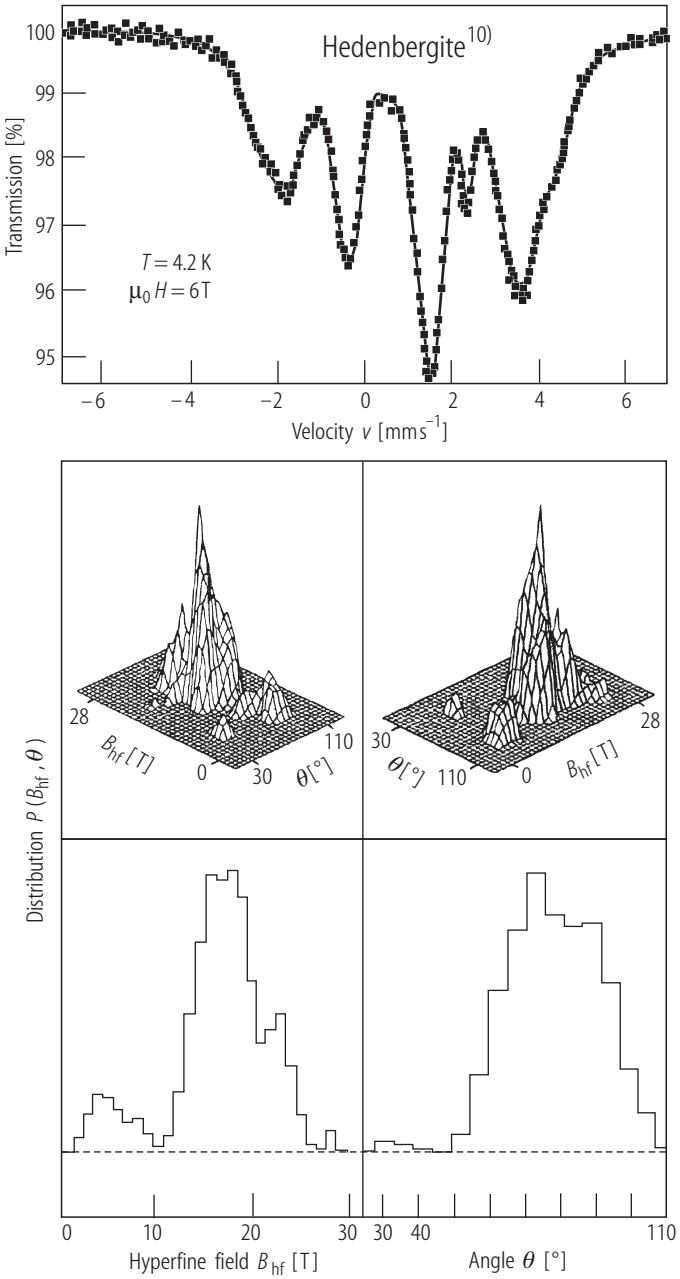

Fig. 73. Hedenbergite[10)]. Experimental (squares) and calculated (solid lines) ^{57}Fe NGR spectrum at 4.2 K in external field $\mu_o H$ = 6 T. The corresponding three-dimensional view of the (B_{hf}, θ) distribution and the distribution of the integrated probabilities for θ and B_{hf} are depicted in the bottom drawings [03E2]. For composition see Table 10.

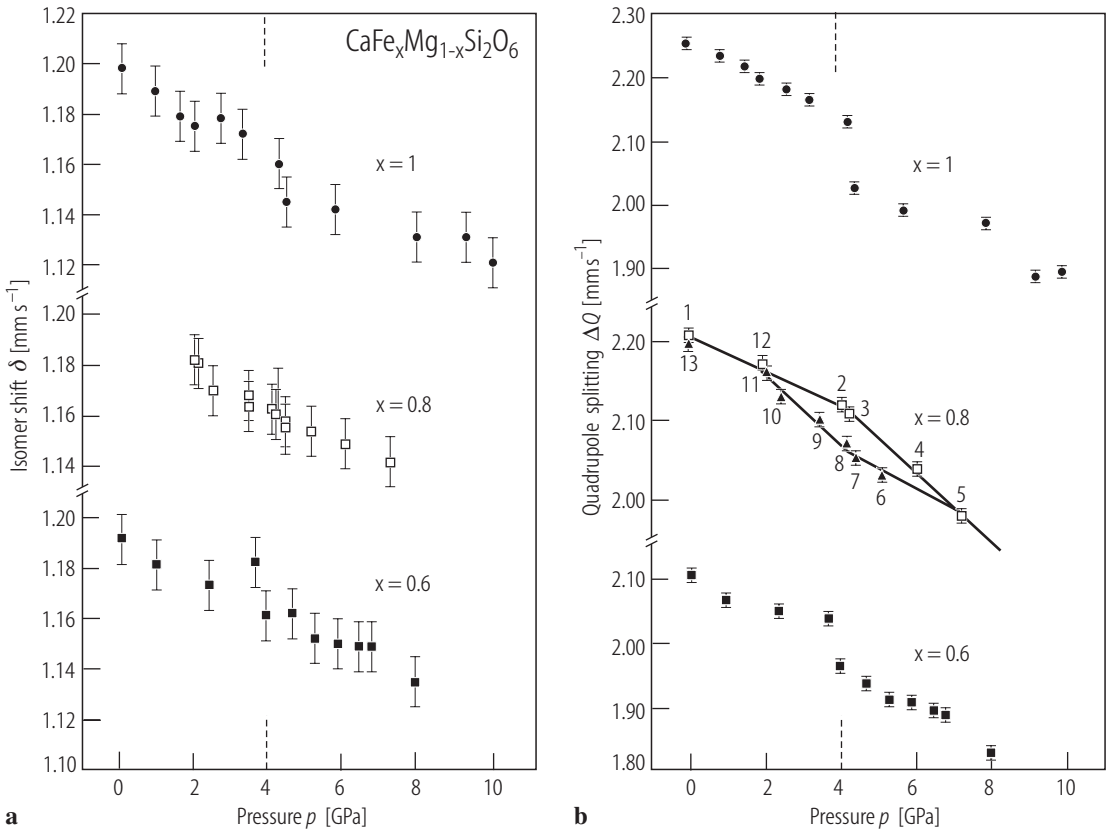

Fig. 74. $CaFe_xMg_{1-x}Si_2O_6$ with x = 1.0; 0.8 and 0.6. Pressure dependences of isomer shift (**a**) and of quadrupole splitting, (**b**) There is a discontinuity at approximately 4 GPa. [92Z1]. The data for x = 0.8 were taken consecutively. They yield a pressure hysteresis.

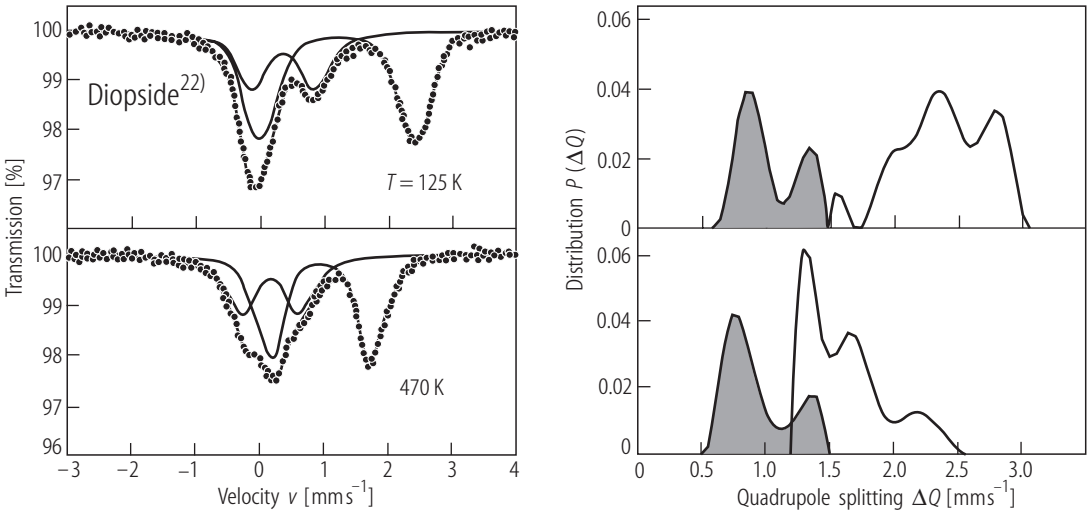

Fig. 75. Diopside[22)]. ^{57}Fe NGR spectra at 125 K and 470 K and calculated probability distributions of the quadrupole splittings for the ferrous and ferric (shaded) ions [02D1]. For composition see Table 10.

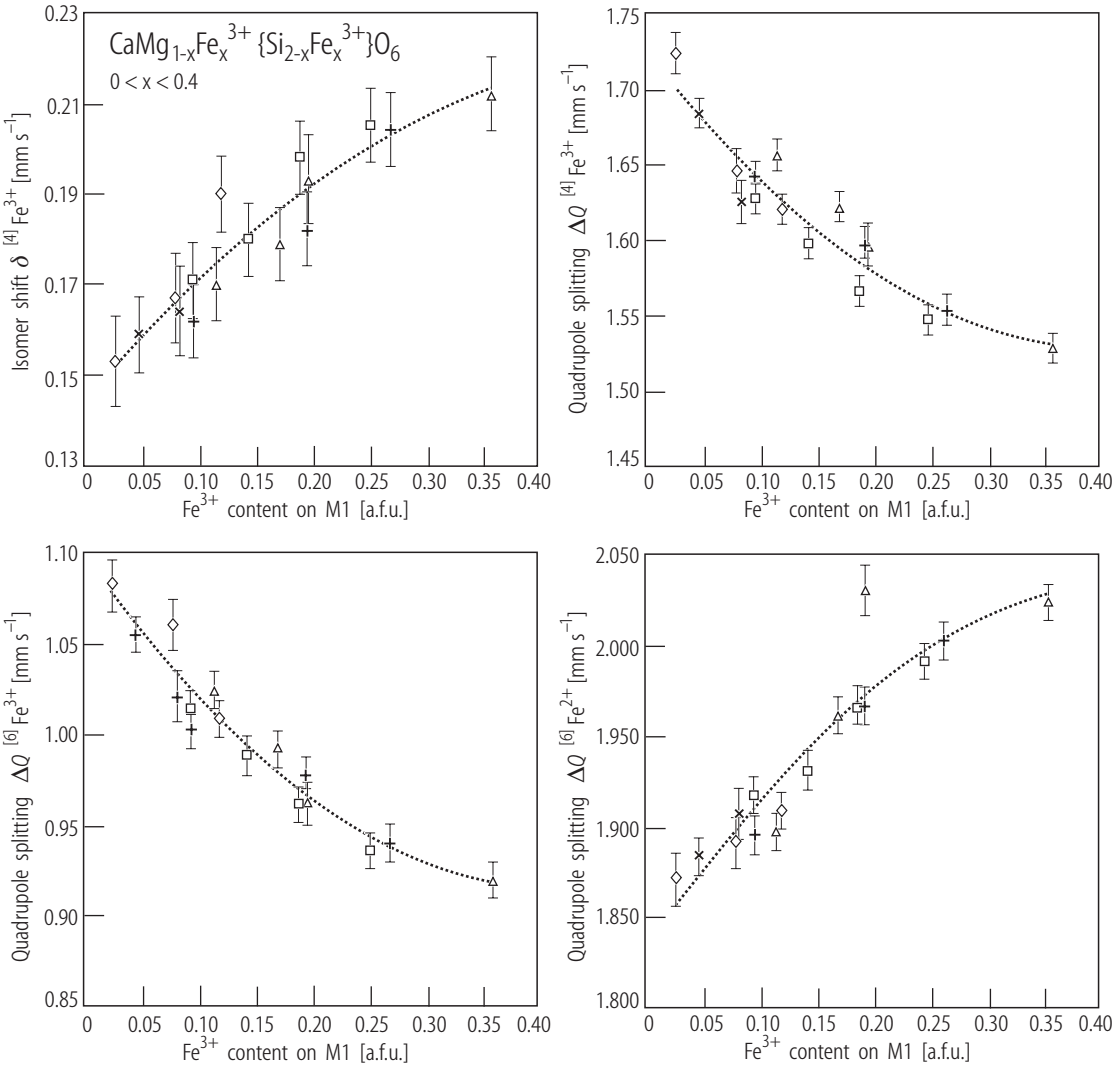

Fig. 76. $CaMg_{1-x}Fe^{3+}{}_x\{Si_{2-x}Fe^{3+}{}_xO_6\}$. Dependences of the isomer shift and quadrupole splittings as result of the Fe for Mg substitution on M1 [98R1]. The sintering temperatures were noted by: 1325°C (diamond), 1250°C (triangles), 1200°C (squares), 1150°C (stars), 1050°C (crosses). Dotted lines are guide for the eyes.

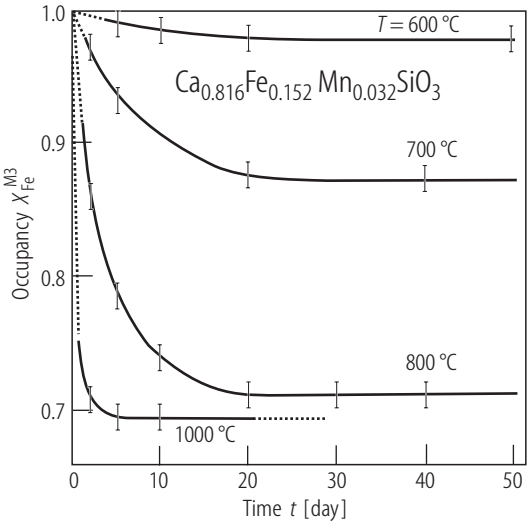

Fig. 77. $Ca_{0.816}Fe_{0.152}Mn_{0.032}SiO_3$ ferrobustamite. Site occupancy of Fe atom at the M3 site in the disordering processes of the thermal intracrystalline Fe-Ca exchange [79Y2].

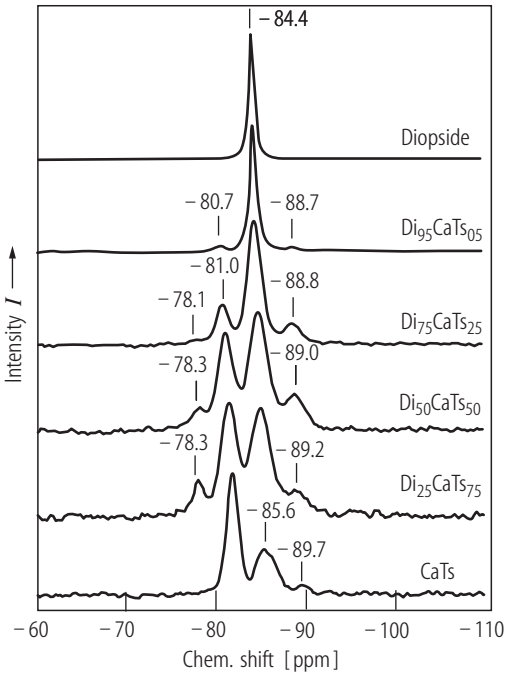

Fig. 80. $CaMgSi_2O_6$ – $CaAl_2SiO_6$. ^{29}Si MAS NMR spectra. Number refer to chemical shifts in ppm [02F1].

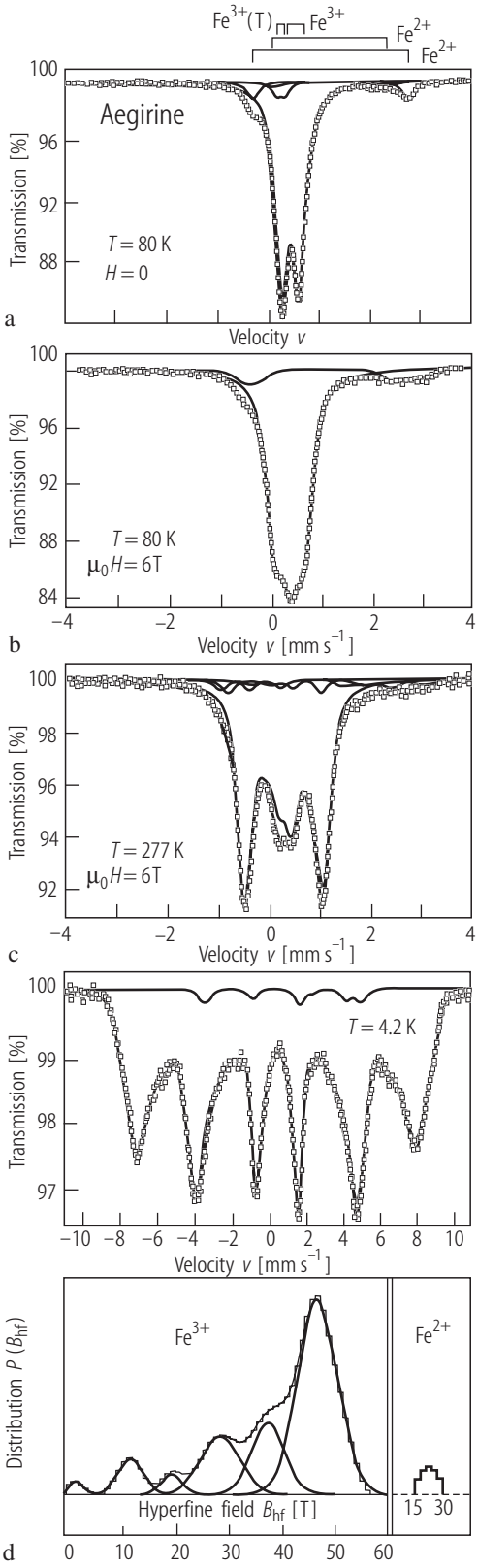

Fig. 78. Natural aegirine. ^{57}Fe NGR spectra at 80 K, at $\mu_o H$ = 0 (**a**) and at 80 K (**b**) and 277 K (**c**) with absorber subjected to an external field $\mu_o H$ = 6 T applied parallel to the incident γ-ray beam. (**d**) ^{57}Fe NGR spectrum at 4.2 K. The resulting probability distributions are shown in lower part, the one referring to Fe^{3+} being decomposed into Gaussians [98D1].

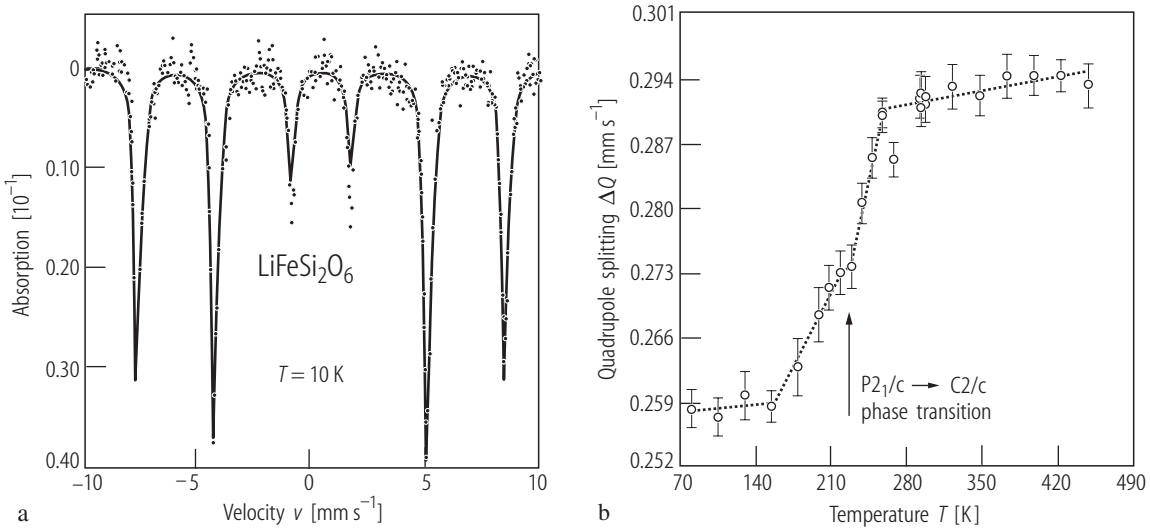

Fig. 79. $LiFeSi_2O_6$. (**a**) ^{57}Fe NGR spectrum of a synthetic single crystal, section with $\boldsymbol{k} \parallel \boldsymbol{b}$, at 10 K [98L1]; (**b**) variation of the quadrupole splitting of Fe^{3+} as a function of temperature [01R1].

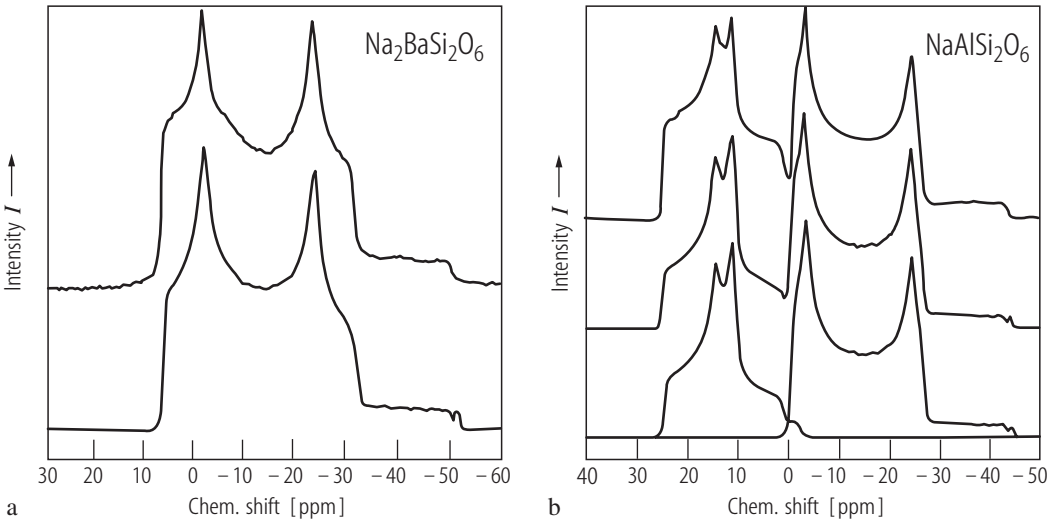

Fig. 81. $Na_2BaSi_2O_6$ (**a**) and $NaAlSi_2O_6$ jadeite (**b**). ^{23}Na MAS NMR spectra and computer simulations [93X1]. In each plot, the upper spectrum is the experimental one and below it is the simulated spectrum. In (**b**) the components of the simulation are also shown at the bottom. All the spectra were collected with 0.9 μs of pulse length, 1s delay and 1000…7000 signal averages.

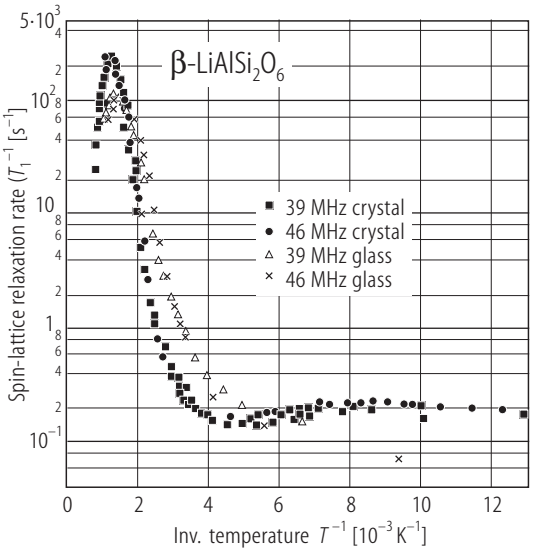

Fig. 81A. β-$LiAlSi_2O_6$. Spin-lattice relaxation rate of polycrystalline and glassy spodumene as function of inverse temperature for two Larmor frequencies $\omega_L/2\pi$ [92F2, 05Q1]

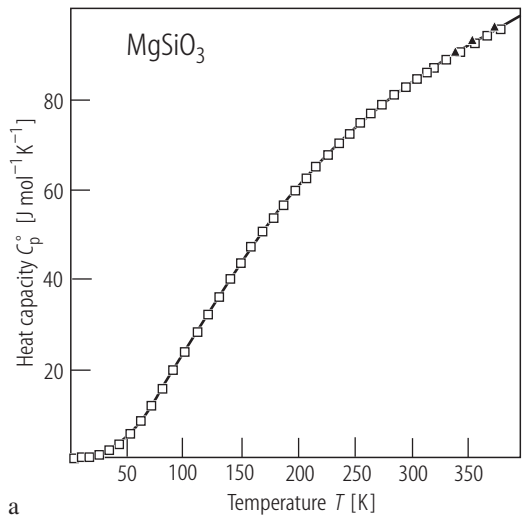

a

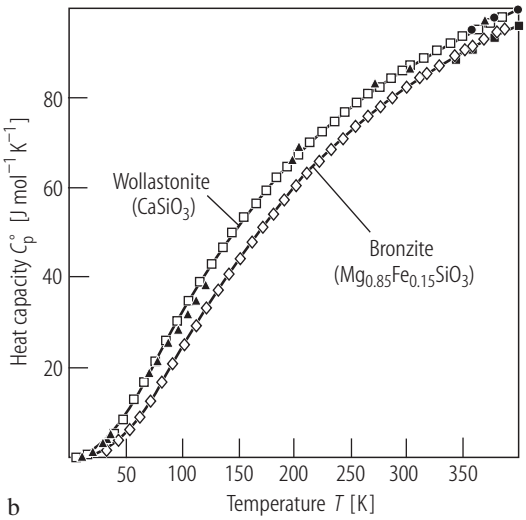

b

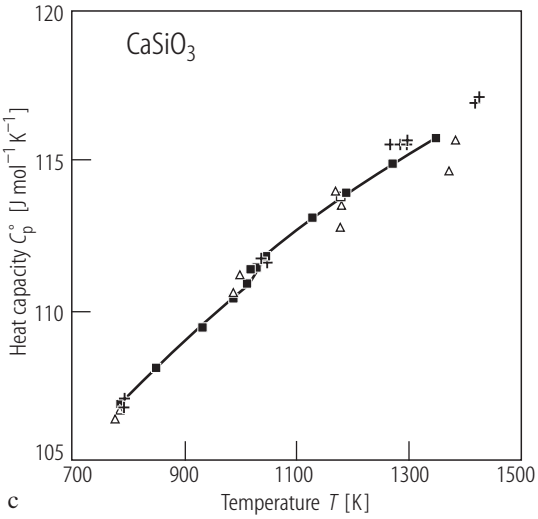

c

Fig. 82. $MgSiO_3$ (**a**), $Mg_{0.85}Fe_{0.15}SiO_3$ and $CaSiO_3$ (**b**, **c**). Molar heat capacities as function of temperature [85K5]. The open diamonds and open square are data determined by adiabatic calorimetry [85K5]. The solid triangles in (**a**) and solid squares and solid circles in (**b**) are data determined by DSC analysis [85K6]. The solid triangles (in (**b**)) are the low-temperature data for $CaSiO_3$ [32W1]. In (**c**) are the high-temperature data for $CaSiO_3$ samples from various sources. Fig. from [91R1]. The solid curves are least-squares fits to experimental data.

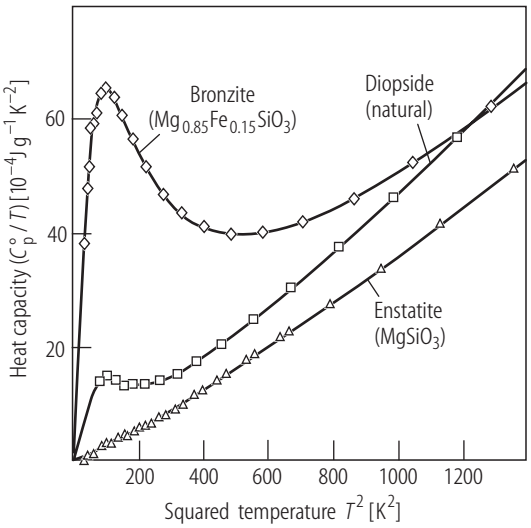

Fig. 83. $MgSiO_3$, $Mg_{0.85}Fe_{0.15}SiO_3$; natural diopside. Heat capacities as function of T^2 [85K5].

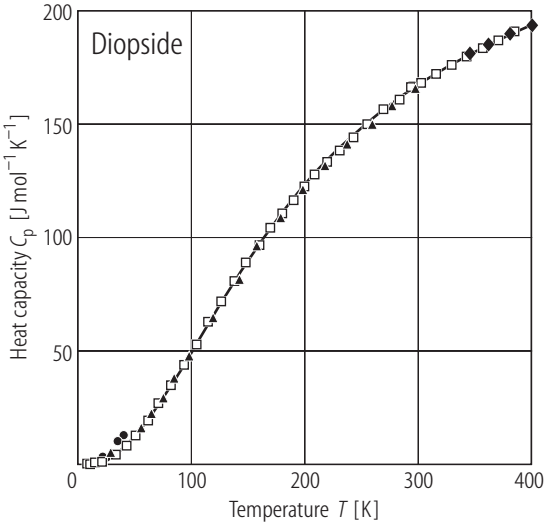

Fig. 85. Diopside. Molar heat capacity. The open squares and solid diamonds were determined by an adiabatic calorimetry [85K5] and DSC analysis [85K6], respectively. The solid circles and solid triangles are the low-temperature C_p data of [32W1] and [57K1], respectively. The solid line is a least-squares fit to the experimental data [85K5].

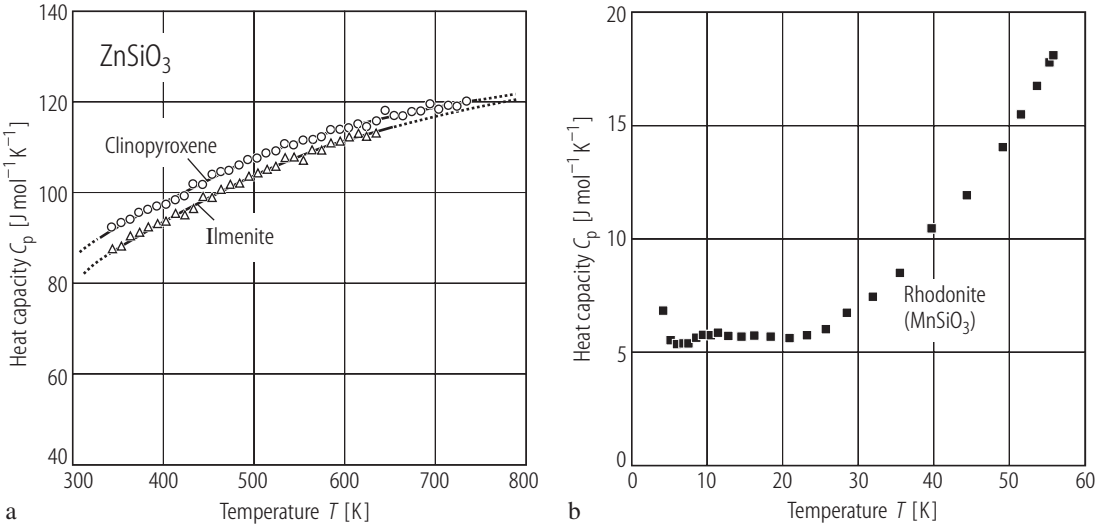

Fig. 84. $ZnSiO_3$ clinopyroxene and ilmenite (**a**) [90A1] and rhodonite (**b**) [95R1]. Heat capacities as function of temperature.

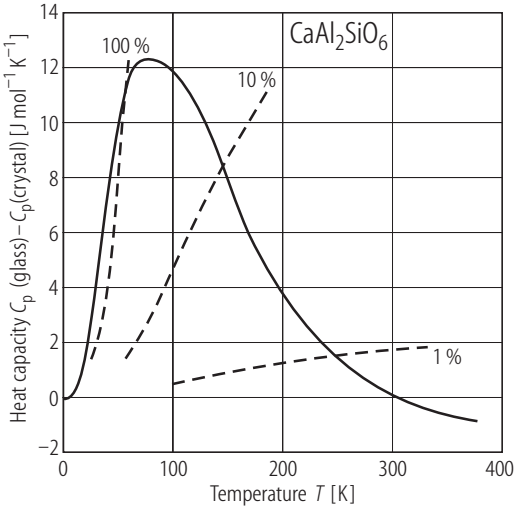

Fig. 86. $CaAl_2SiO_6$. Differences in heat capacities of glass and pyroxene as a function of temperature [84H1]. Differences relative to the heat capacity of the pyroxene are indicated by dashed curves.

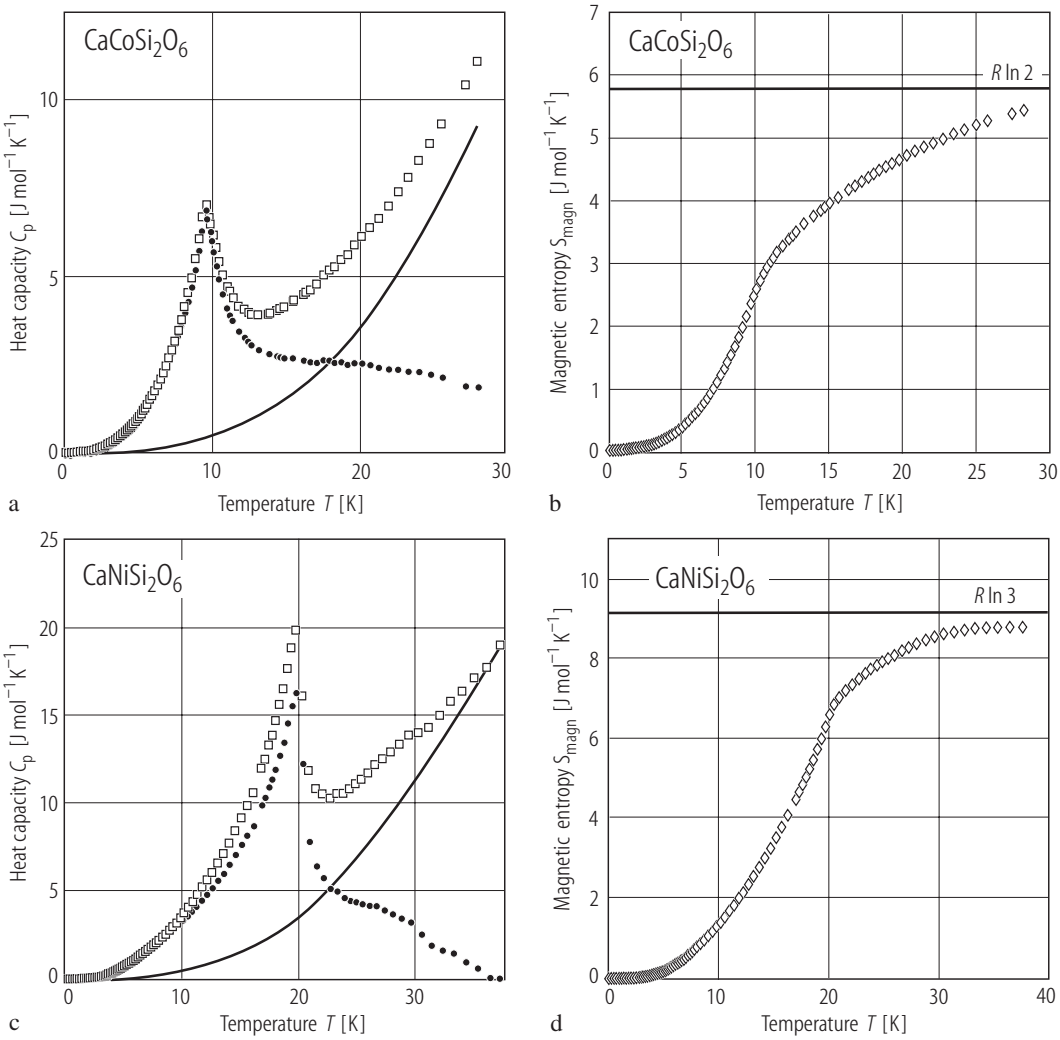

Fig. 87. $CaCoSi_2O_6$ (**a**, **b**), $CaNiSi_2O_6$ (**c**, **d**). Temperature dependences of heat capacity (**a**, **c**). The full line and dotted line represent the lattice and magnetic contributions, respectively. The evolutions with temperature of magnetic entropy are shown in (**b**, **d**) [96D3].

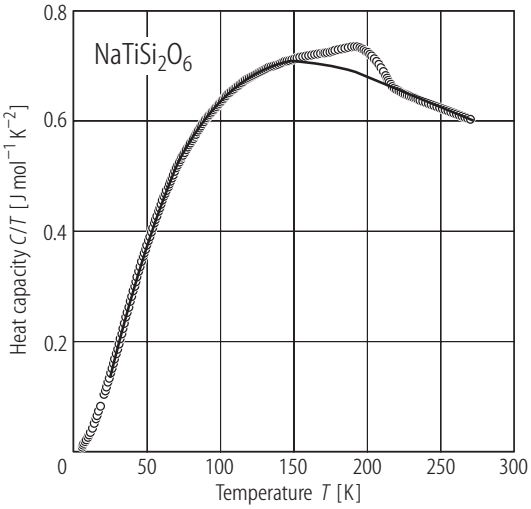

Fig. 88. $NaTiSi_2O_6$. Temperature dependence of the heat capacity [02I1].

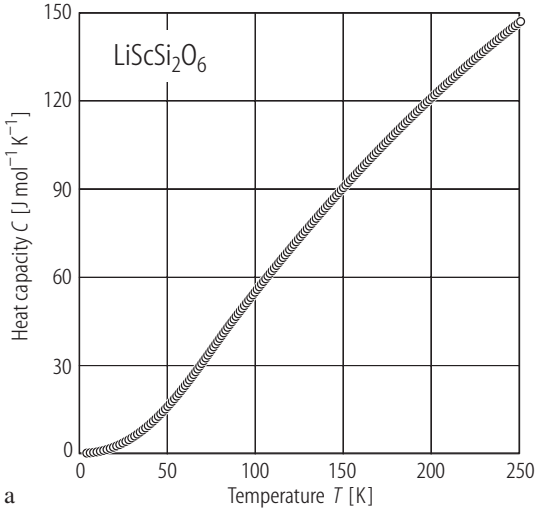

a

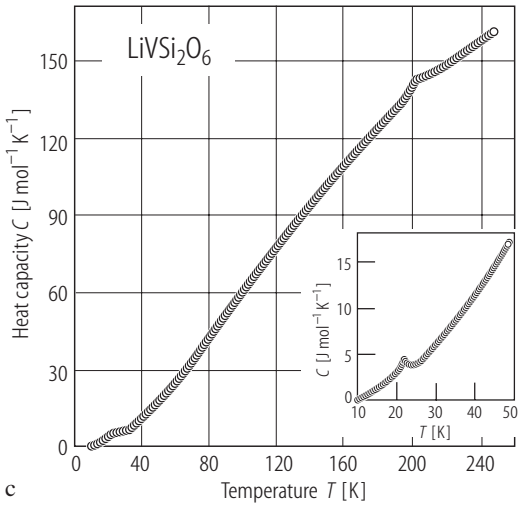

c

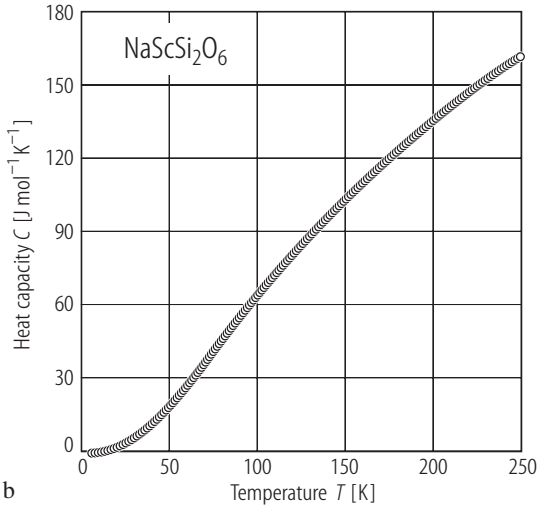

b

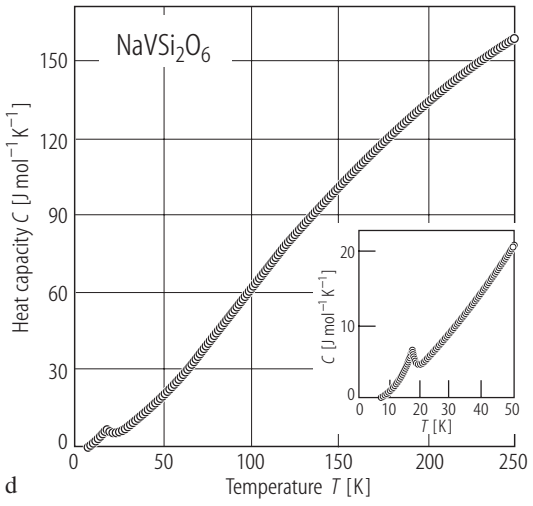

d

Fig. 89. $AMSi_2O_6$. Temperature dependences of the heat capacity (**a**) A = Li, M = Sc; (**b**) A = Na, M = Sc; (**c**) A = Li, M = V; (**d**) A = Na, M = V [04V1]. Insets of Figs. **c**, **d** show the low-*T* range on an enlarged scale.

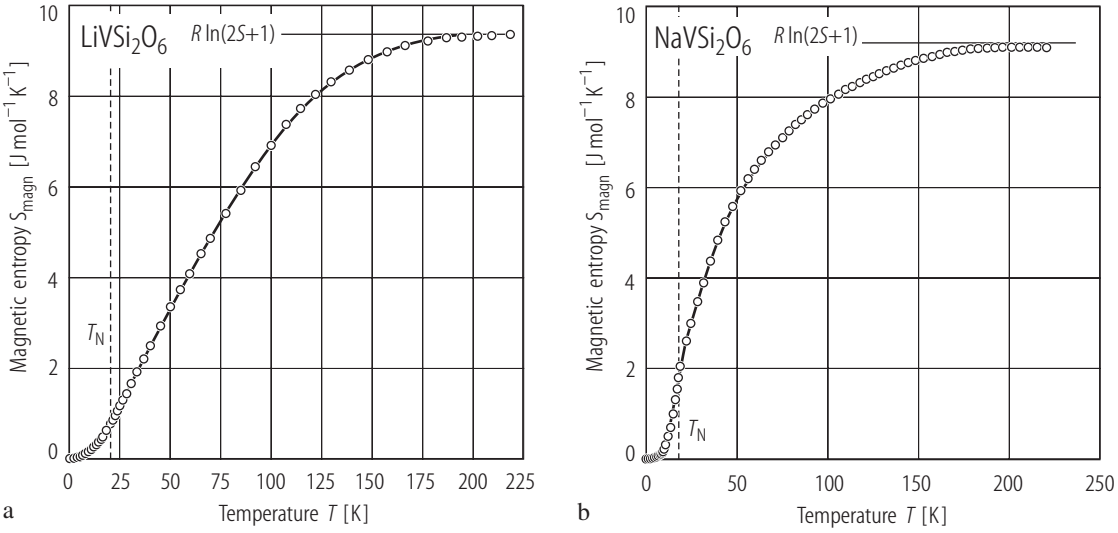

Fig. 90. $AVSi_2O_6$. Temperature dependences of the magnetic entropy (**a**) A = Li; (**b**) = Na [04V1].

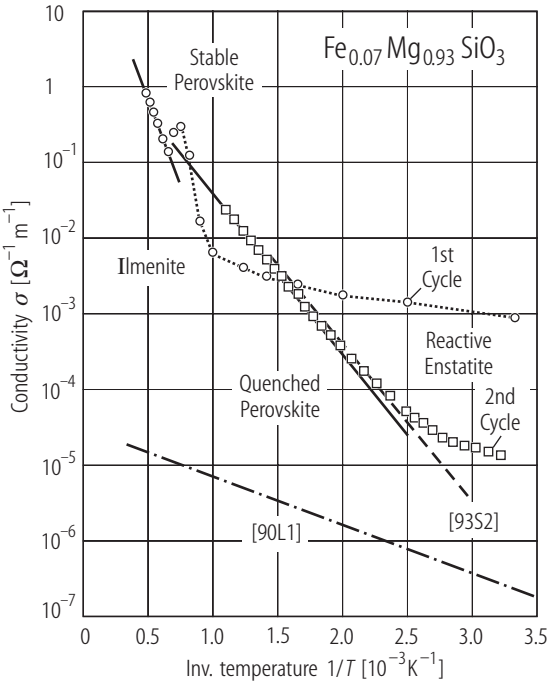

Fig. 91. $Fe_xMg_{1-x}SiO_3$. Electrical conductivity of stable and quenched perovskite (x = 0.07). The circles and squares correspond to conductivity values measured in the first and second heating cycles, respectively. In the first cycle, the samples should be perovskite at $T > 1500$ K. In the second cycle, it should be perovskite over the whole temperature range, although the values were affected by the insufficient electrical insulation of the assembly [98K1]. The conductivity values in diamond anvil cell were reported by [90L1] for x = 0.12 perovskite at 57 GPa and by [93S2] for x = 0.11 perovskite at 23 GPa.

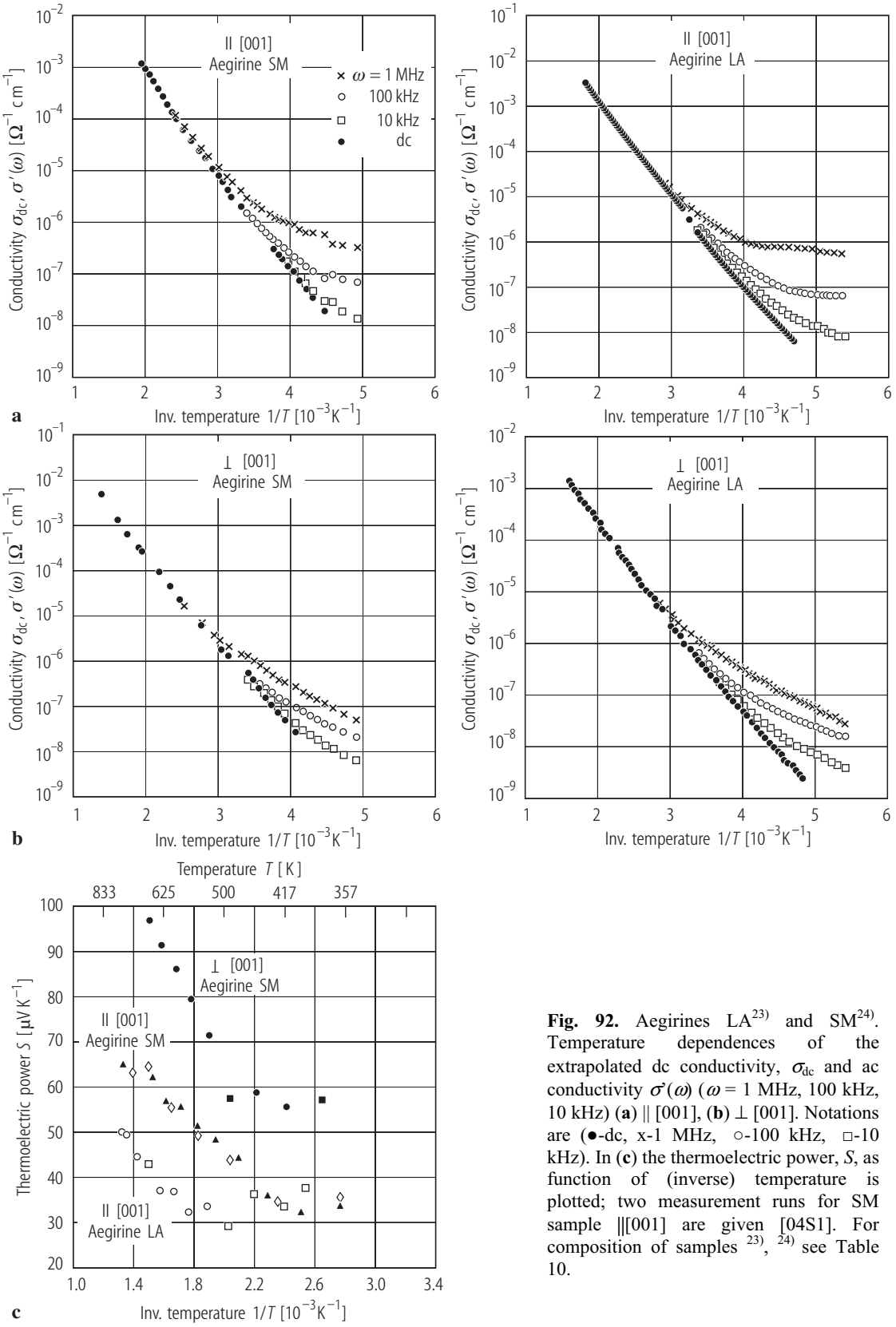

Fig. 92. Aegirines LA[23] and SM[24]. Temperature dependences of the extrapolated dc conductivity, σ_{dc} and ac conductivity $\sigma'(\omega)$ (ω = 1 MHz, 100 kHz, 10 kHz) (**a**) || [001], (**b**) ⊥ [001]. Notations are (●-dc, x-1 MHz, ○-100 kHz, □-10 kHz). In (**c**) the thermoelectric power, *S*, as function of (inverse) temperature is plotted; two measurement runs for SM sample ||[001] are given [04S1]. For composition of samples [23], [24] see Table 10.

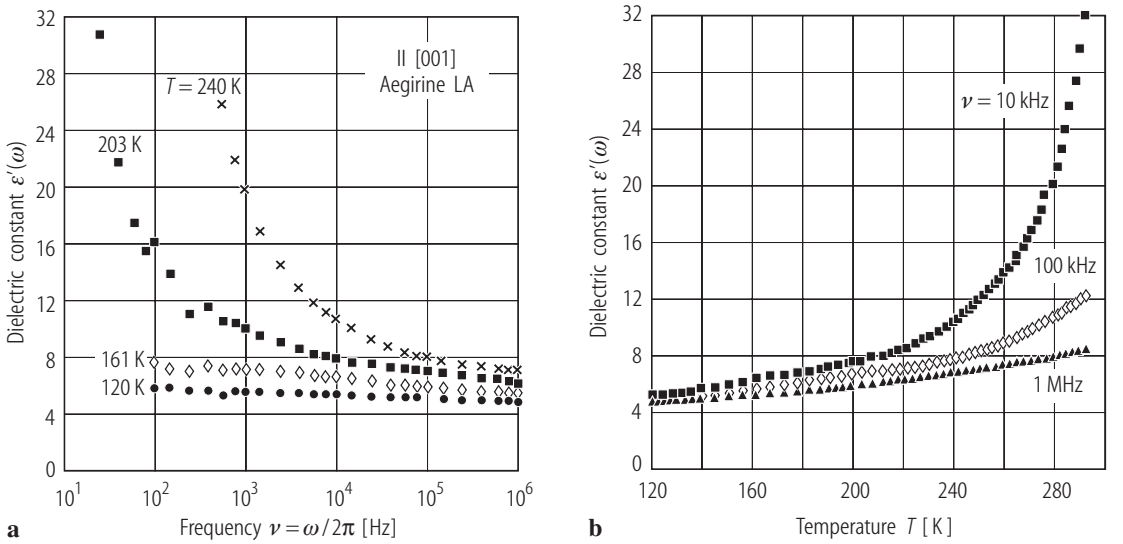

Fig. 93. Aegirine LA[22)]. Relative dielectric permittivity (**a**) as a function of frequency, at several temperatures, (**b**) vs. temperature for several frequencies [04S1]. For composition of sample [23)] see Table 10.

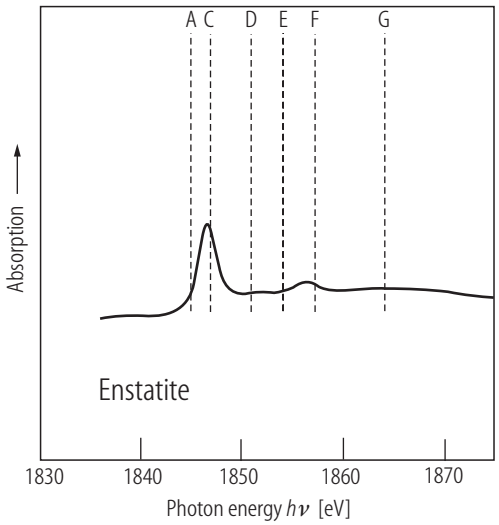

Fig. 94. Enstatite. Si K-edge XANES spectrum [95L1].

For Fig. 95 see next page

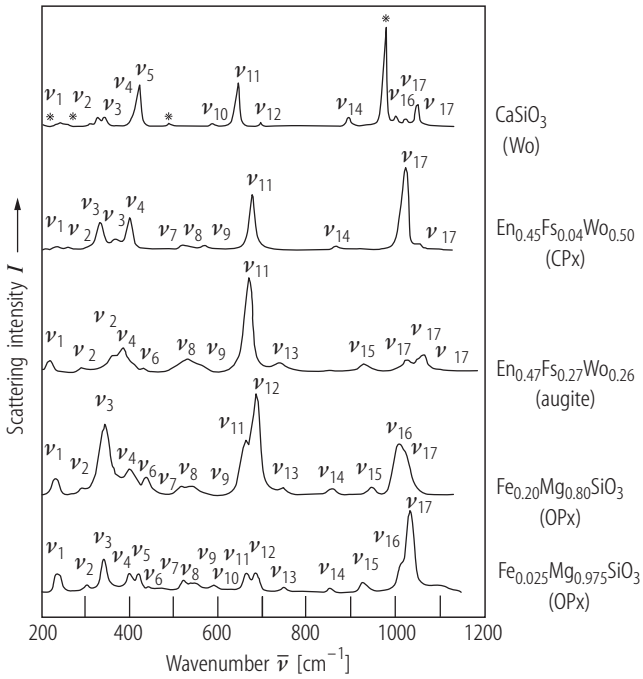

Fig. 96. $Fe_{0.025}Mg_{0.975}SiO_3$, $Fe_{0.20}Mg_{0.80}SiO_3$, $En_{0.45}Fs_{0.04}Wo_{0.50}$ and $En_{0.47}Fe_{0.27}Wo_{0.26}$ and $CaSiO_3$ (Wo). Representative Raman spectroscopic patterns [00H1].

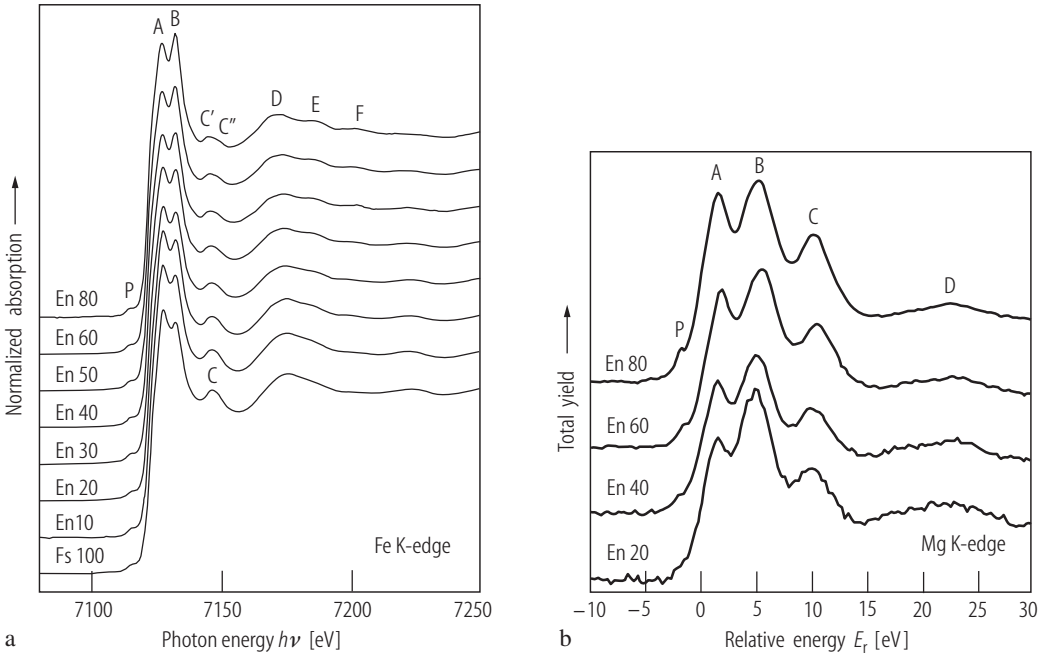

Fig. 95. $Mg_2Si_2O_6$ (En) – $Fe_2Si_2O_6$ (Fs) synthetic orthopyroxenes. (**a**) Fe K-edge XANES spectra, (**b**) Mg K-edge XANES spectra [02G1].

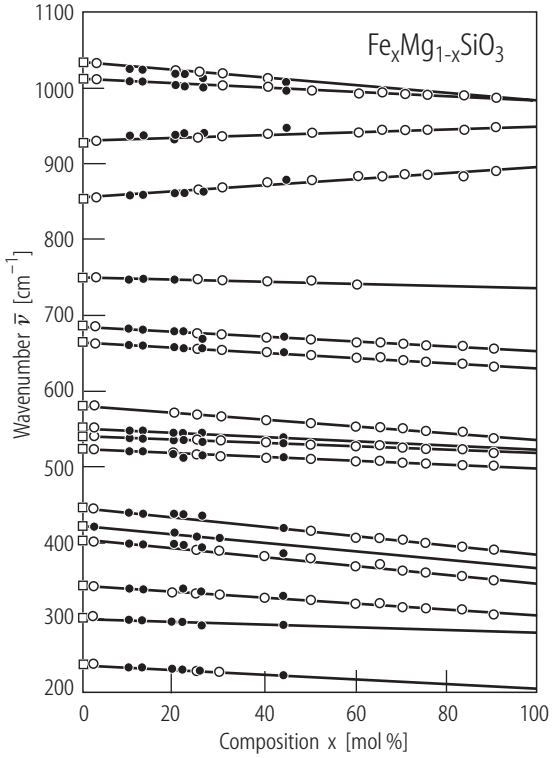

Fig. 97. $Fe_xMg_{1-x}SiO_3$. Raman frequencies versus Fe content. Solid circles are natural crystals; open circles are synthetic polycrystals [00H1]. Data for enstatite [99C2] are shown as open squares.

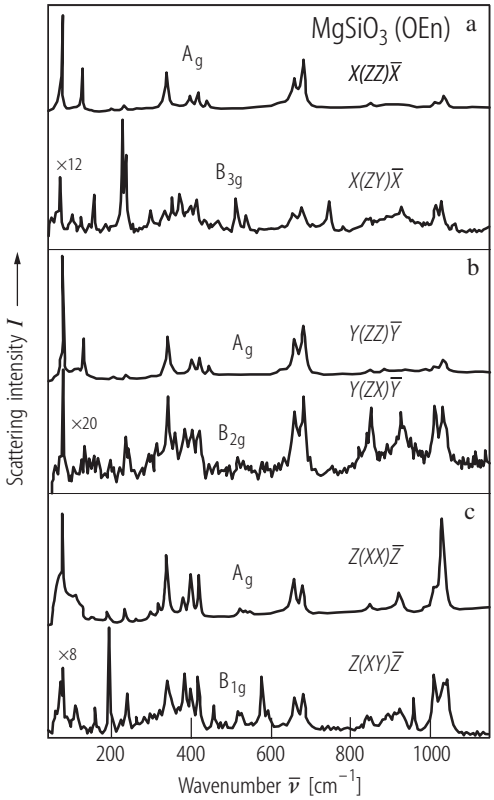

Fig. 98. $MgSiO_3$ orthoenstatite single crystal. Polarized Raman spectra using the (**a**) (100); (**b**) (010); (**c**) (001) planes. The spectra were recorded using the 514.5 nm line of the Ar^+ ion laser [98C3].

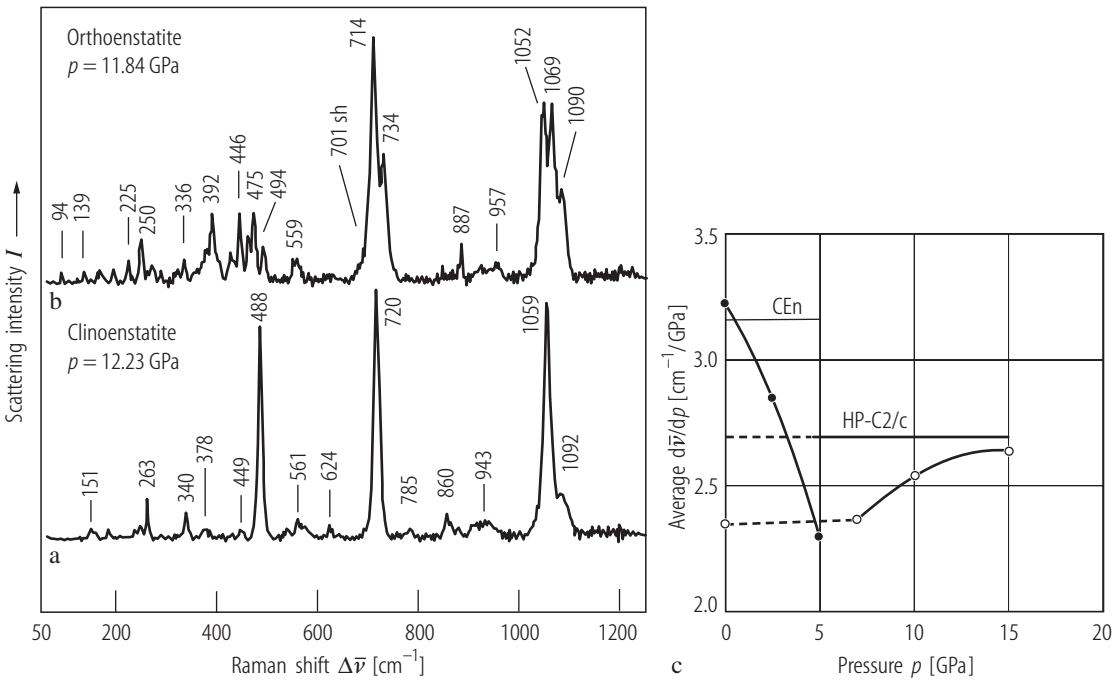

Fig. 99. High-pressure polymorphs of (**a**) clinoenstatite (at 12.23 GPa) and (**b**) orthoenstatite (at 11.84 GPa). Raman spectra at room temperature. (**c**) The average pressure derivatives of Raman frequency ($d\bar{\nu}/dp$) as function of pressure. Solid and open circles denote clinoenstatite and high-p C2/c enstatite, respectively [04L1]. The two horizontal lines are based on the results of [92C2], the upper for clinoenstatite (CEn) and the lower for the high-p C2/c enstatite (HP-C2/c).

For Fig. 100 see next page

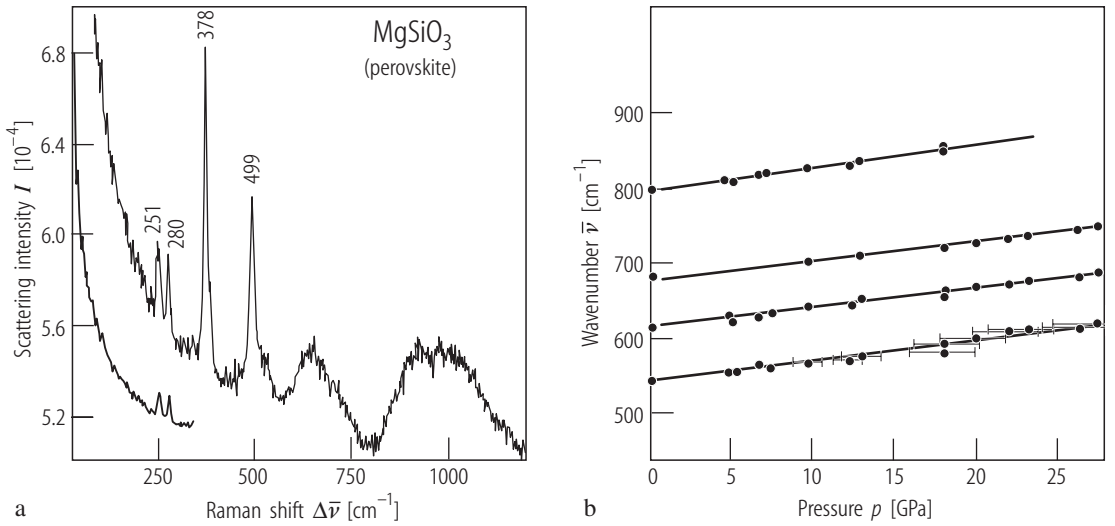

Fig. 101. $MgSiO_3$ perovskite. (**a**) Zero-pressure Raman spectrum; (**b**) peak positions in mid-IR spectrum as function of pressure [87W1].

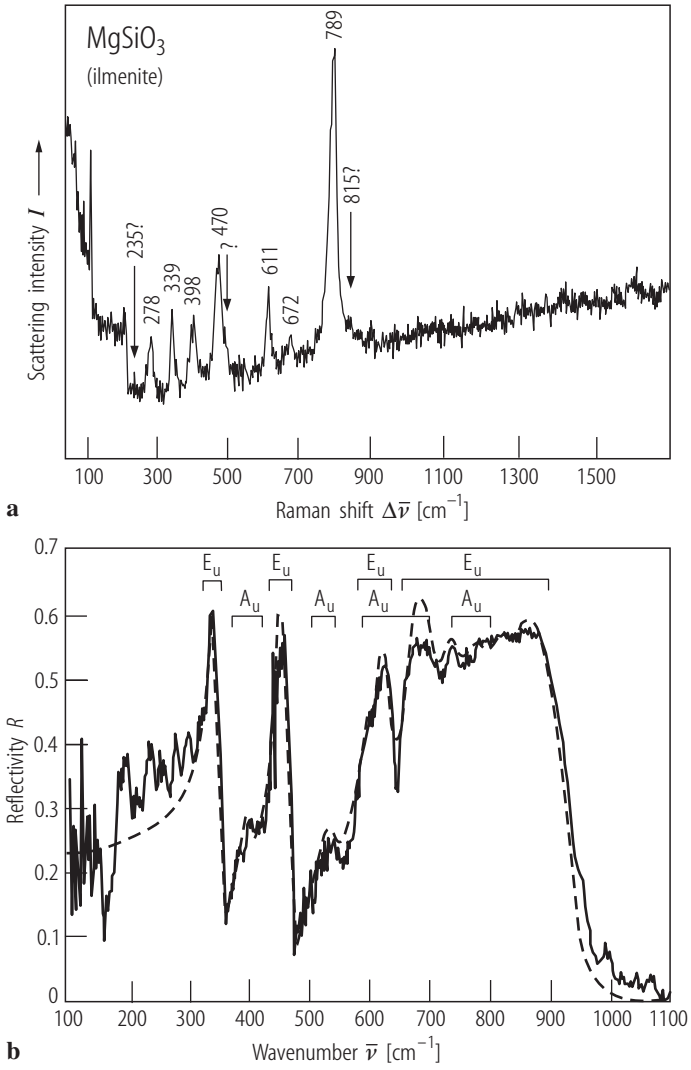

Fig. 100. $MgSiO_3$ ilmenite. (**a**) Raman spectrum. The asymmetric "band" near 200 cm^{-1} is due to a spectrometer ghost and the sharp peaks below 100 cm^{-1} are laser plasma lines and rotational lines of N_2 and O_2 in the air [84R2]. (**b**) IR single crystal unpolarized reflectance spectrum [92H2].

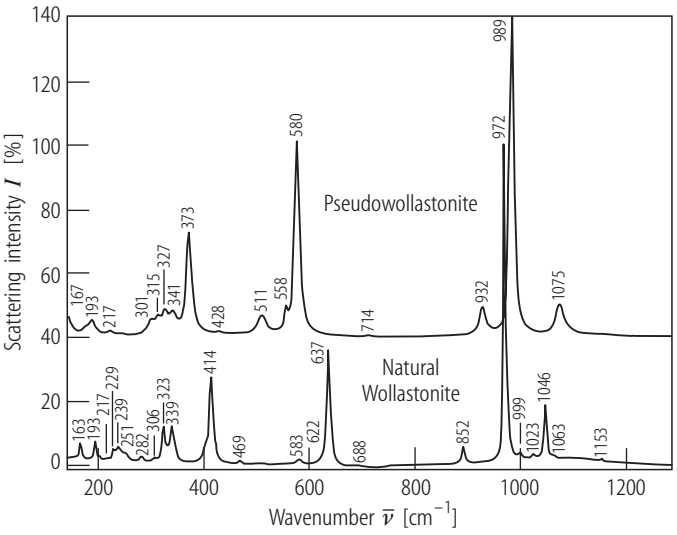

Fig. 102. Pseudowollastonite, wollastonite (natural). Raman spectra [98R3].

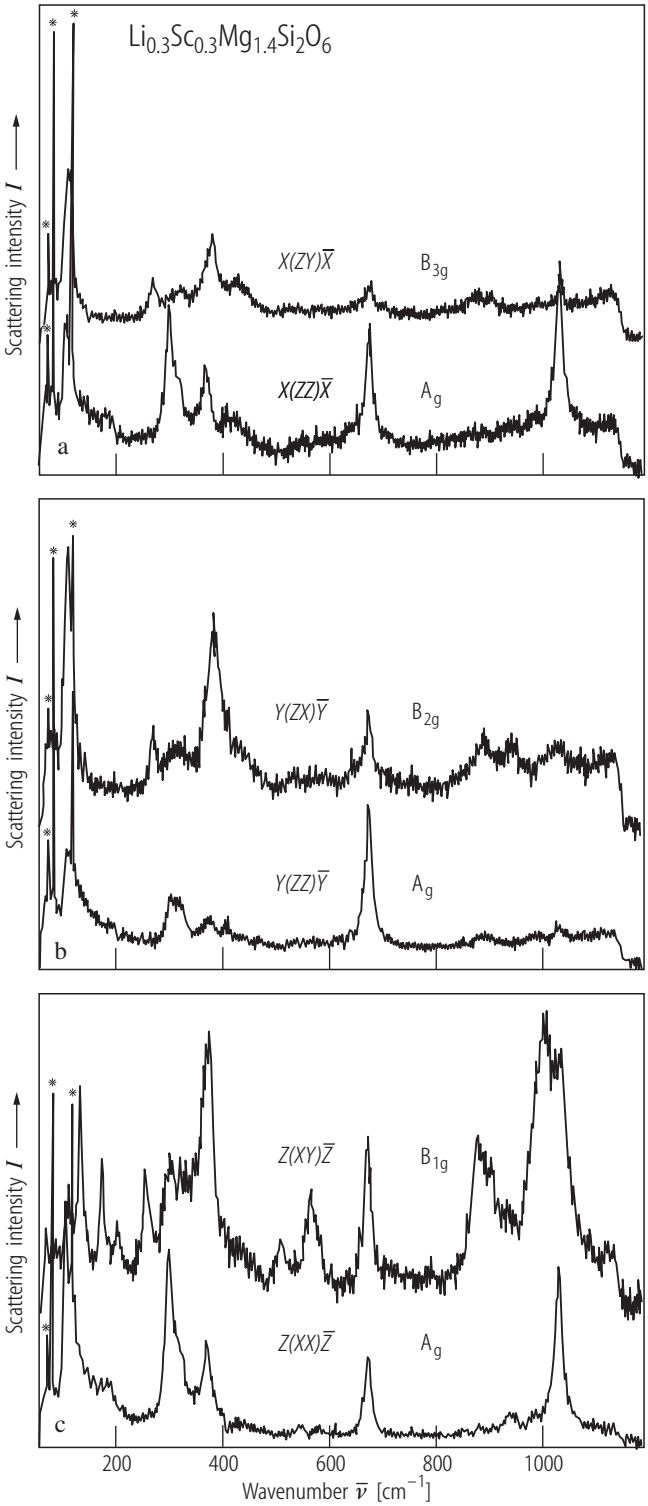

Fig. 103. $Li_{0.3}Sc_{0.3}Mg_{1.4}Si_2O_6$. Polarized Raman spectra using (**a**) (100), (**b**) (010) and (**c**) (001) faces of the single crystal. The spectra were recorded using the 514.4 nm line of the Ar^+ ion laser; the plasma lines are indicated by * [94G3].

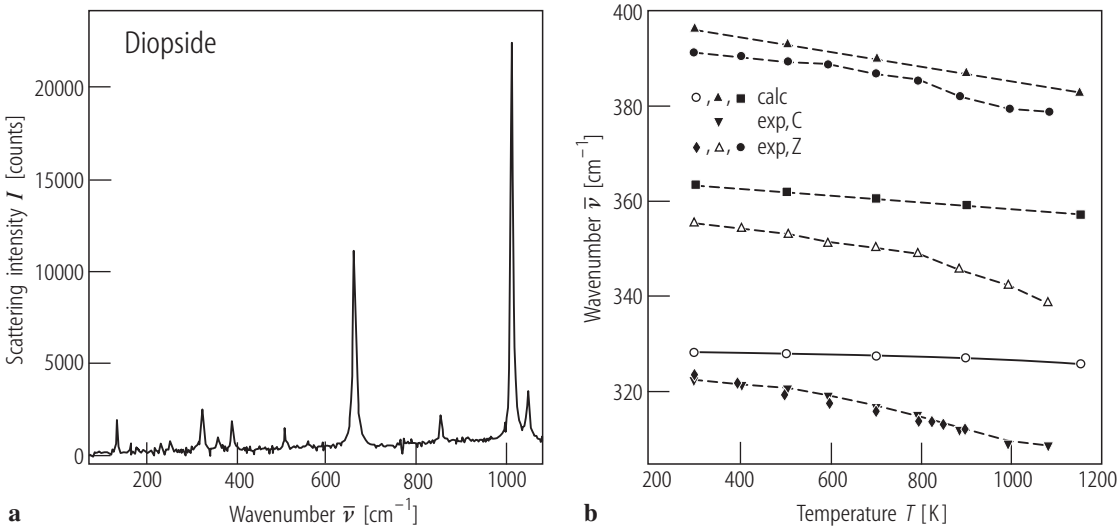

Fig. 104. Diopside (natural). (**a**) Polarized Raman spectrum showing the A_g modes (in orientation $Y(XX)\bar{Y}$); (**b**) experimental and calculated temperature evolution of the A_g Raman modes in the 300…400 cm^{-1} region. The data for two natural diopsides were denoted by Z (poor iron) and C (Fe-rich) [97S2]. The curves reaching the highest temperature (1150 K) belong to the calculated spectra.

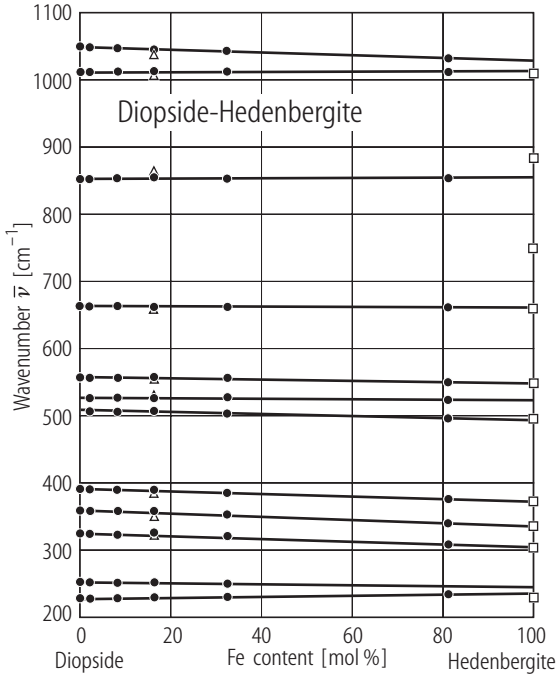

Fig. 105. Diopside – hedenbergite. Raman frequencies versus Fe content. Solid circles: composition with 50 mol % Wo, open triangles: 44 mol % Wo, open squares: some previous unpublished data by the same authors [00H1]. For representative Raman spectra see Fig. 96.

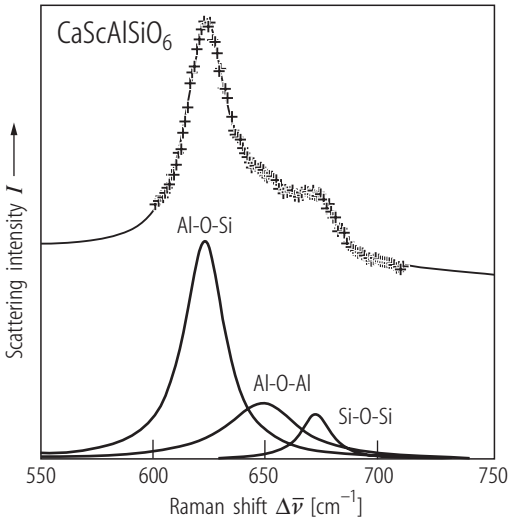

Fig. 106. $CaScAlSiO_6$. Deconvolution of the Raman spectrum. (+) Experimental data, solid lines are Lorentzian component and composite spectra [88S3].

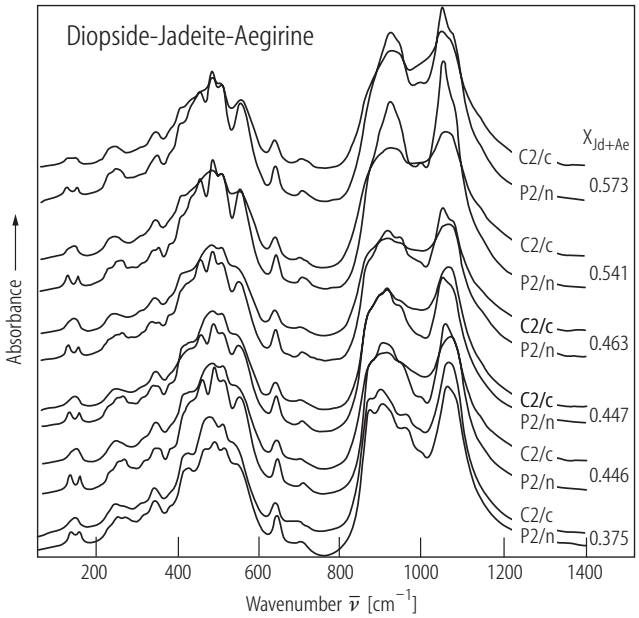

Fig. 107. Diopside – jadeite – aegirine. IR powder absorption spectra of natural ordered and experimentally disordered omphacites of the same composition, measured at RT. Changes in the frequency region 100…200 cm^{-1} are apparent [98B2]. The content of jadeite – aegirine is denoted on the right side.

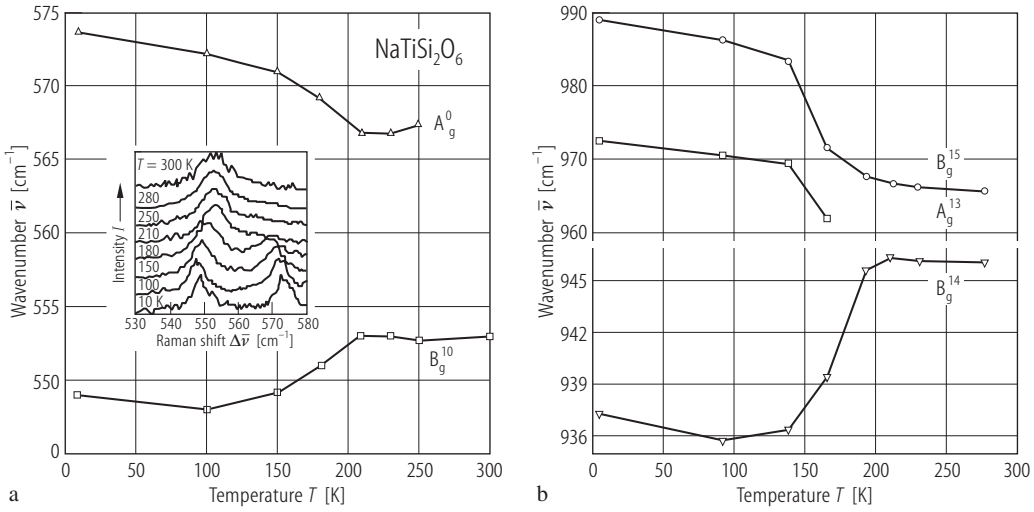

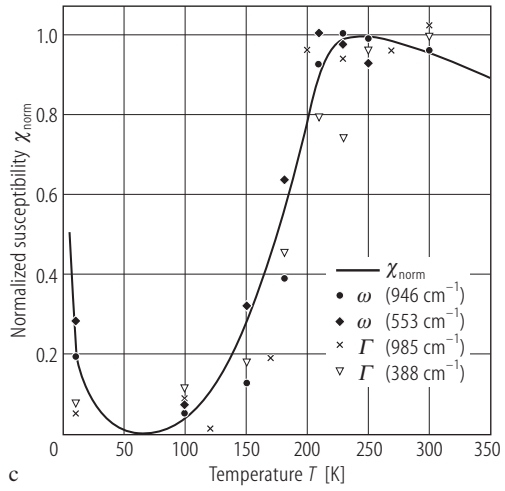

Fig. 108. $NaTiSi_2O_6$. (**a**) Temperature dependence of the frequency and broadening of the 553 cm^{-1} Raman mode. In inset Raman spectra at various temperatures in the range 530…580 cm^{-1} are shown. (**b**) Frequency versus temperature for B_g^{14}, A_g^{13} and B_g^{15} (Ti-O1,2 and Si-O1,2 stretching) modes. (**c**) Temperature dependence for several modes (frequencies and linewidths) together with the normalized magnetic susceptibility [05P2].

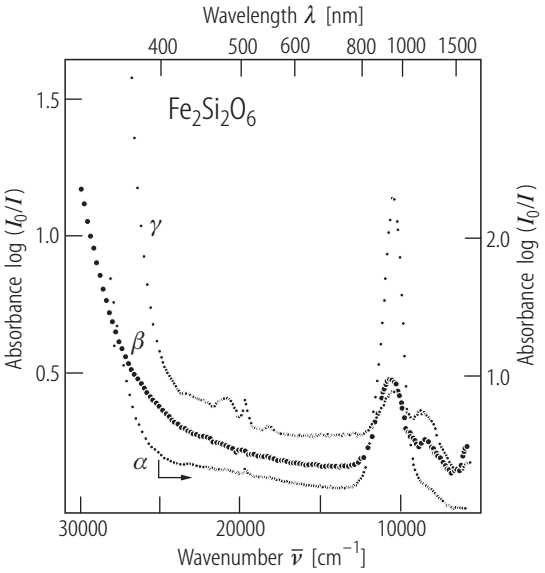

Fig. 109. $Fe_2Si_2O_6$. Polarized spectra of a synthetic sample. The α-spectrum was obtained from a (100) slab 24(4) µm thick, the β- and γ-spectra from a (010) slab, 43(4) µm thick. The ordinate on the right applies to the α-spectrum [88S5].

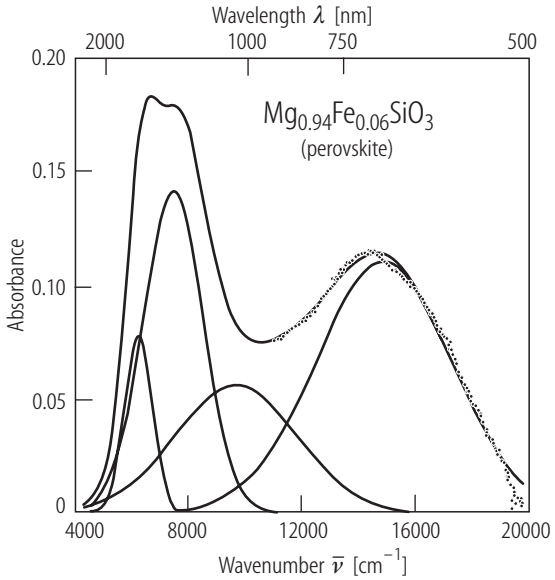

Fig. 110. $Mg_{0.94}Fe_{0.06}SiO_3$ perovskite. Unpolarized absorption spectrum after background correction and deconvolution into Gaussian components. Measured data are shown as dots [94K2].

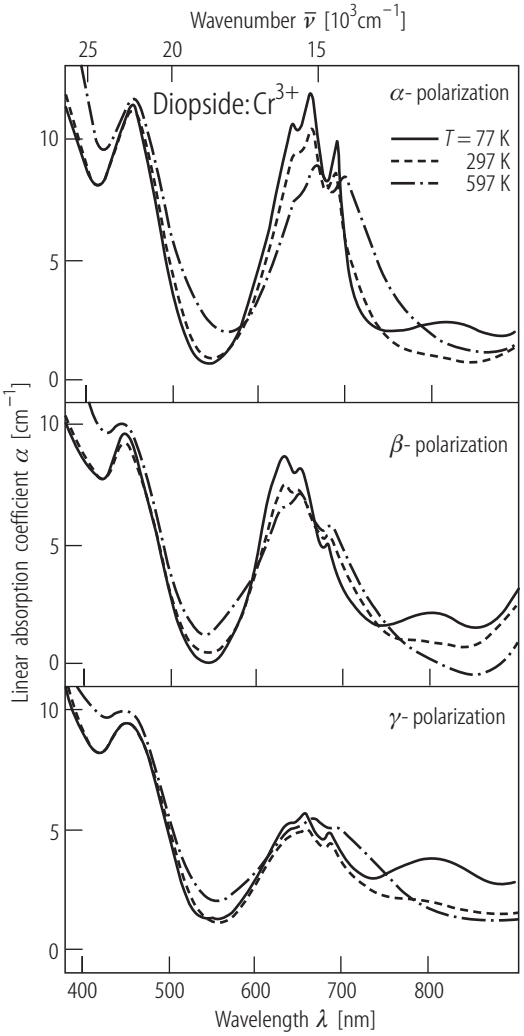

Fig. 111. Cr^{3+} bearing diopside. Polarized spectra α, β and γ in the temperature range 77…597 K [94T1].

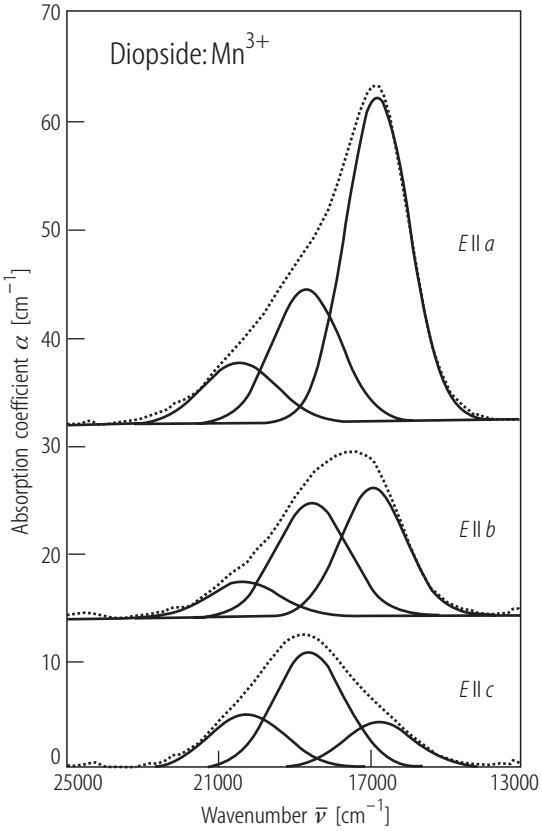

←

Fig. 112. $Co_{0.967}Na_{0.013}Mg_{0.958}Mn^{2+}_{0.059}Mn^{3+}_{0.012}Si_{1.988}B_{0.011}O_6$ synthetic diopside. Curve resolved net absorption spectra for $\boldsymbol{E} \parallel \boldsymbol{a}$, $\boldsymbol{E} \parallel \boldsymbol{b}$ and $\boldsymbol{E} \parallel \boldsymbol{c}$. The stippled lines represent the obtained net absorption spectra and full lines show the fitted absorption bands as well as the sum of the fitted component [96H1].

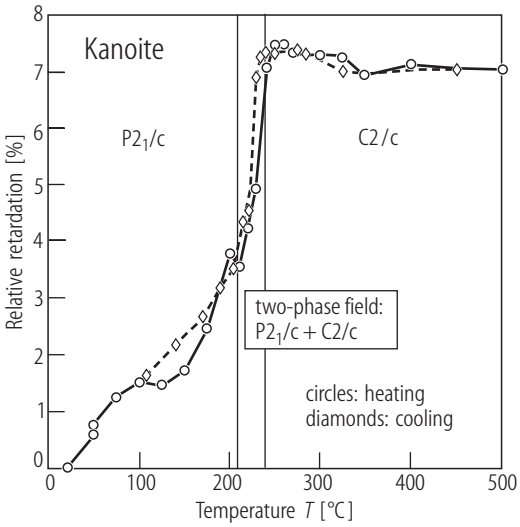

Fig. 113. Kanoite. Relative retardation as function of temperature [97A2]. Composition (in wt %): MnO – 26.42, MgO – 16.74, CaO – 2.81, SiO_2 – 52.07, FeO – 0.97, Na_2O – 0.36, Al_2O_3 – 0.47.

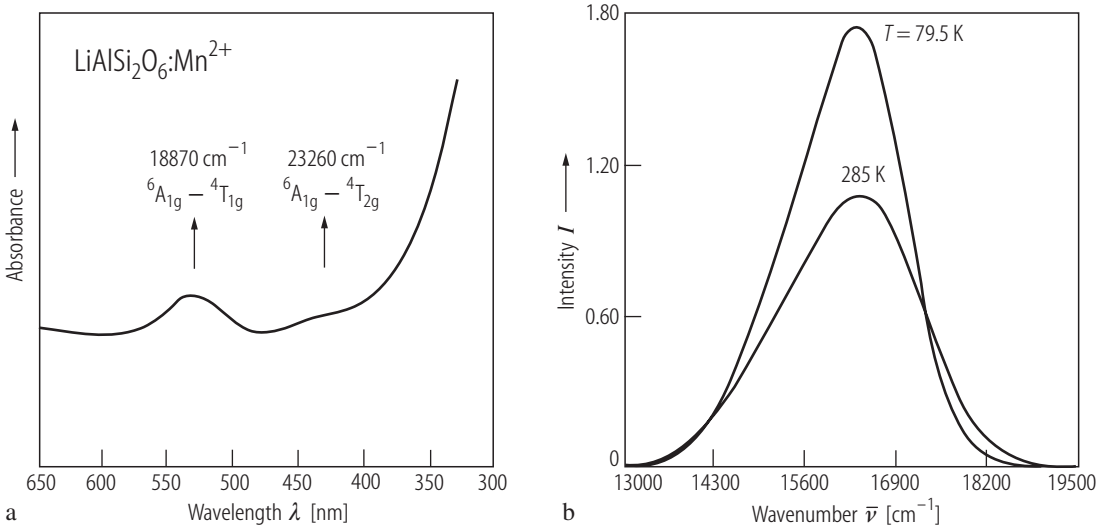

Fig. 114. Spodumene: Mn^{2+} (kunzite). (**a**) Absorption and (**b**) emission spectra at 79.5 K and 285 K [92C1].

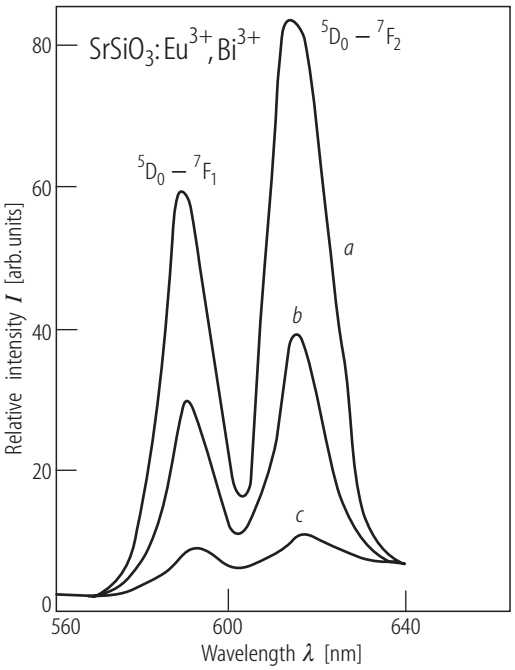

Fig. 115. $SrSiO_3$: Eu^{3+}, Bi^{3+}. Emission spectra of samples synthesized by (curve *a*) sol-gel; (*b*) at atmospheric pressure and (*c*) at high pressure [93L1].